SCIENTIFIC SUPPORT PLAN FOR A SUSTAINABLE DEVELOPMENT POLICY
(SPSD II)

Part 2:
Global change, Ecosystems and Biodiversity

FINAL REPORT

**ASSESSING THE SENSITIVITY OF THE SOUTHERN OCEAN'S
BIOLOGICAL CARBON PUMP TO CLIMATE CHANGE
(BELCANTO II)**

EV/07

*F. Dehairs[1], C. Lancelot[2], L. André[3], H. Goosse[4],
M. Frankignoulle[5]
S. Becquevort[2], A. Borges[5], D. Cardinal[3], A. de Montety[4],
B. Delille[5], M. Elskens, S. Jacquet[1], W. Lefebvre[4], B. Pasquer[2],
N. Savoye[1], V. Schoemann[2]*

*[1]. Analytical and Environmental Chemistry,
Vrije Universiteit Brussel
[2]. Ecologie des Systèmes Aquatiques,
Université Libre de Bruxelles
[3]. Lab. of Geochemistry, Dept. of Geology, Musée Royal de l'Afrique Centrale
– Koninklijk Museum voor Midden Afrika ,
[4]. Institut d'Astronomie et de Géophysique G. Lemaître, Université Catholique
de Louvain
[5]. Unité d'Océanographie Chimique, Université de Liège*

BELGIAN SCIENCE POLICY

Tabel of contents

Abstract

BELCANTO (BELgian research on Carbon uptake in the ANTarctic Ocean) is a long-term project aiming at applying and developing process-level studies, geochemical proxy tools and numerical tools for assessing and understanding the present-day functioning of the CO_2 biological pump in the iron-limited Southern Ocean (S.O.) and for predicting its evolution in response to scenarios of increasing atmospheric CO_2.

Over the last four years BELCANTO implemented and developed several multi-proxy approaches for assessing nutrient consumption and carbon fluxes, including [234]Th-deficit and natural silicon isotopic composition.

High quality results were obtained for whole water column δ^{29}Si-silicate and δ^{29}Si-opal, including first ever results for the low silicate Subantarctic region. Results show that the δ^{29}Si signature of diatoms appears to be homogeneous in the mixed layer and between diatom species. The preferential uptake of light isotope by diatoms is well reflected in the vertical distribution of silicate δ^{29}Si, as well as in the upper ocean silicate δ^{29}Si values which increase northwards in parallel with the decrease of silicate concentration. However, the relationship between δ^{29}Si and silicate concentration appears complex and depends on variations in vertical and horizontal supply of silicate.

Results based on other proxy tools (Ba_{xs} [234]Th-deficit, *f*-ratio & new production) indicate relatively high particulate carbon export and absence of strong mesopelagic mineralization in the Subantarctic Zone, but relatively low export and enhanced mesopelagic mineralization further south in the Polar Front Zone and the southern ACC. Furthermore, remineralization was clearly enhanced during summer as compared to spring. Our observations of [234]Th-based carbon export and new production along cross frontal transects also appear to challenge the widely accepted idea of enhanced primary and export production in the Subantarctic Zone and the Polar Frontal Zone, compared to more southern areas.

Laboratory-controlled experiments on two widespread phytoplankton species (diatoms-*Thalassiosira gravida* and *Phaeocystis antarctica*) showed an effect of Fe addition on the morphological form, enhancing the presence of the colonial form compared to the free-living cells for *Phaeocystis* and increasing the appearance of long chains of diatoms vs. free living cells. Under Fe enriched conditions, the

maximum photosynthesis and growth rates increased. In addition the quality of the organic matter was modified, enhancing bacterial remineralization. Consequently, Fe addition may impact on the fate of the phytoplankton in the planktonic food web and the resulting efficiency of the biological pump. Accordingly, during the EIFEX large scale iron enrichment experiment, iron addition fosters a diatom bloom which appeared to broke up rather fast and to sink rapidly accordingly to ^{234}Th measurements. This in turn triggered mesopelagic mineralization as evidenced in Ba_{xs} measurements.

N-uptake experiments with Fe-limited and Fe-replete natural algal communities indicate that the effects of ammonium and iron on *f*-ratio and new production are not simply cumulative and that the enhancement of the *f*-ratio due to Fe addition depends on the ambient ammonium concentration. However the relationship between this enhancement and ammonium concentration is at present not fully understood. Our results imply that there is no simple relationship between export production and iron availability. Ammonium appears to counter the effects of iron addition on export production, particularly for HNLC areas such as the Southern Ocean.

The meso-scale iron enrichment experiment performed during the EIFEX cruise, clearly showed that iron addition induced a diatom bloom but that the latter did not persist for long and collapsed soon after, thereby inducing a massive export of carbon as witnessed from significant deficits in ^{234}Th activity. This export in turn triggered mesopelagic organic carbon mineralization as evidenced by excess Ba_{xs} contents.

Measurements of pCO_2, scaled using remote sensing data (sea surface temperature, chlorophyll and wind stress) and related CO_2 fluxes, suggest that previous budgets of atmospheric CO_2 uptake in the S.O. may be overestimated. However, our observations indicate that sea ice cover can act as an additional CO_2 sink not taken into account in previous CO_2 budgets. This sea-ice CO_2 sink function results from physical and biogeochemical processes prevailing within the sea ice itself.

Results obtained with SWAMCO-4, an idealized 1-D model of the marine planktonic system calculating C, N, P, Si, Fe cycling within the upper ocean, the export production and air-sea CO_2 fluxes, suggest that the sink for atmospheric CO_2 will increase in response to the raising atmospheric CO_2 concentration. SWAMCO-4 simulations show that the amplitude of the predicted CO_2 sink displays large regional and inter-annual variations which are related to local hydrodynamics and the dominant

phytoplankton species. This is particularly acute in the *Phaeocystis*-dominated marginal ice zone of the Ross Sea. There the predicted annual CO_2 sink appears positively related to the length of the sea ice cover period. This results from the accumulation of iron within the ice and its sudden release in the water column at the time of ice melting, favoring algal growth.

The past and future evolution of the sea ice cover was conducted using the ORCA2-LIM and ECBILT-CLIO 3D ice-ocean models. The influence of the Southern Annular Mode on zonal integrated sea surface temperature and ice concentration seems to be small due to counteracting effects. Over the last 250 years, the annual mean ice coverage decreased in response to both natural and anthropogenic forcing, with the impact of the latter forcing clearly being enhanced over the last 150 years. Nowadays, the decrease of ice cover is more acute in the northern hemisphere as compared to the southern hemisphere, and this difference is due to thermal inertia of the S.O. However, model outputs predict a more abrupt decrease of S.O. sea ice extent in the future, resulting in similar decreases of annual mean sea ice extents in both hemispheres by the end of the century. In parallel, the seasonal amplitude of sea ice extent will increase.

Preliminary runs with the coupled ice-ocean-biogeochemical model ORCA-LIM-SWAMCO-4, predict that the efficiency of the S.O. biological pump will be very sensitive to changes in the seasonal amplitude and the mean extent of the ice cover.

Keywords: Biological Carbon Pump - CO_2 fluxes - Iron limitation - Carbon flux proxies - climate variability - Coupled ice-ocean-biogeochemical model

Introduction

The research described in the present report focused on the role of the Southern Ocean in global change. It was carried out by an interdisciplinary network of biologists, geochemists, and physical and ecological modellers (BELCANTO: BELgian research on Carbon uptake in the ANTarctic Ocean). The aim was to apply and develop geochemical proxies and numerical tools for assessing and understanding the present-day functioning of the CO_2 biological pump in the iron-limited Southern Ocean and predicting its evolution in response to scenarios of increasing atmospheric CO_2. The research methodology involved and combined existing and new field data, laboratory process-level studies and numerical work in order to improve our understanding of the mechanisms controlling the production of key bloom-forming phytoplankton groups of the Southern Ocean (diatoms and *Phaeocystis*), their sinking rate and biodegradation when exported in the mesopelagic zone (100-1000 m).

Process studies were conducted under laboratory-controlled conditions on cultures of key Antarctic phytoplankton species (*P. antarctica* and *Thalassiosira gravida* colonies and free-living cells) and bacteria using natural, sub-nanomolar-iron Southern Ocean water. Focus was on the effect of light and nutrient ($Fe/NO_3/NH_4/Si$) regulation of phytoplankton morphology, growth and sinking, as well as on iron and organic substrate control on bacterial activities and therefore on degradation of phytoplankton-derived material. Laboratory experiments were complemented with field studies focusing on combined control by varying ammonium/nitrate ratio and iron availability on *f*-ratio, including a large scale in-situ ocean fertilisation experiment (EIFEX). These studies allowed for the parameterisation of the major processes to be described by the applied biogeochemical model.

Natural Southern Ocean short-term nutrient utilisation patterns were studied via isotope dilution methods (^{15}N-nutrients), providing information on *f*-ratio and new production as a measure for 'exportable' production, for areas with varying diatom dominance. For silicate a method was implemented and optimised providing for seasonally integrated nutrient uptake, as based on the changing natural Si isotopic composition of silicate which results from fractionation during uptake by diatoms.

Based on measurements of underway partial pressure of CO_2 (pCO_2) and disequilibrium with atmospheric CO_2 pressure, we budgeted spring and summer air-sea CO_2 fluxes, using wind speed as inferred from remote sensing data and zonal pCO_2 fields as calculated from the Sea Surface Temperature (SST) and chlorophyll-a proxies. Biologically sustained carbon export fluxes from the upper mixed layer under natural (low iron) conditions were estimated via the [234]Th-deficit method. The fate of exported carbon in subsurface and intermediate waters was studied via Ba-barite accumulation in the water column, a proxy for organic carbon mineralization.

Overall we obtained information on the magnitude of the major carbon fluxes involved in the biological carbon pump: air-sea exchange; fixation; particle export; mineralization; deep ocean particle flux.

Numerical work involved the upgrading of the biogeochemical SWAMCO-4 model of the marine planktonic system calculating C, N, P, Si, Fe cycling within the upper ocean, the export production and the exchange of CO_2 between the ocean and atmosphere. The ocean response to increased atmospheric CO_2 was explored by running SWAMCO-4 over the last decade for two functionally distinct Southern Ocean environments. At all tested latitudes the prescribed increase of atmospheric CO_2 enhances the carbon uptake by the ocean, though the amplitude of the predicted atmospheric CO_2 sinks displays large regional and inter-annual variations.

As a first step towards assessing atmospheric CO_2 uptake at the whole Southern Ocean scale, the SWAMCO-4 model was coupled to the 3D ice-ocean ORCA-LIM model implemented in the domain south of latitude 30° with a grid of ~ 50km. The simulated temporal shift of algal blooms towards higher latitudes indicates that the model describes well the dual effect of light (effect of latitude and ice cover) and Fe limitation in controlling primary production.

The ORCA-LIM model was also used to analyze the influence of the Southern Annular Mode (SAM) on the ice-ocean system. We observed that surface transport anomalies associated with a positive phase of SAM are directed towards the northwest at high latitudes (south of 45°S) inducing an upwelling that features a maximum around 65°S and a downwelling at about 45°S.

Simulations performed with the ECBILT-CLIO climate model and including natural and anthropogenic forcing suggest that over the past 250 years, the annual mean ice area has decreased by about 1×10^6 m^2, with anthropogenic forcing playing a larger role than natural forcing over the last 150 years. Climate change projections over the 21st century indicate that the amplitude of the seasonal cycle of sea ice extent increases in a warming climate and the annual mean sea ice extent decreases at similar rates in both hemispheres.

I. FUNCTIONING AND BIOGEOCHEMICAL CONTROLS OF PRIMARY PRODUCTION

I.1 Effects of Iron on phytoplankton processes

The pivotal role of iron in regulating rates of primary production and the flux of carbon to the deep sea has become increasingly apparent in the last 15 years. A series of observations and experiments have been essential in establishing this base of knowledge (e.g. *Buma et al.*, 1991, *de Baar et al.*, 2005). Significant improvements in our understanding of the role of iron in regulating ecosystem processes have been made. The addition of Fe stimulates the large class of algae, in particular chain-forming diatoms (*de Baar and Boyd*, 1999). Accordingly, records in naturally iron-enriched regions of the Southern Ocean report biomass accumulation of chain-forming diatoms (*de Baar et al.*, 1995) but also, in some regions, large gelatinous colonies of the non-siliceous Haptophyceae *Phaeocystis* (*Arrigo et al.*, 2000). High iron requirement has been demonstrated for large (20-100 µm) oceanic diatom growth (*Sunda and Huntsman*, 1995) but not for *Phaeocystis* colonies. Some species of diatoms adapt their morphology in function of the available Fe in order to reduce their surface to volume ratio and avoid diffusion limitation (*Timmermans et al.*, 2001). Furthermore, it has been recognized that organisms can increase their iron uptake capacity in response to iron stress, and are capable of luxurious iron uptake. Some phytoplankton species like *Phaeocystis* can accumulate Fe in their mucus, which may constitute storage of Fe in case Fe becomes limiting (*Schoemann et al.*, 2001, 2005). Nowadays a better understanding of those processes is needed in order to evaluate their implications in determining the planktonic community composition and the associated biogeochemical cycles.

In order to determine the effect of Fe limitation on phytoplankton morphology, photosynthesis, Fe assimilation, growth, carbon uptake in the different biochemical pools (proteins, lipids, storage products) and potential sedimentation rates, process-level studies were conducted under laboratory-controlled conditions with key Antarctic algae (chain-forming *Thalassiosira gravida*, *Phaeocystis* colonies and free-living cells) cultured in low Fe (<1nM) and amended (+4nM Fe) Antarctic seawater.

Material and methods

All the experimental procedure was carried out under trace-metal clean conditions as described in *Schoemann et al.* (2001). Polycarbonate or high density polyethylene (HDPE) flasks and filtration devices were used for *Phaeocystis antarctica* and *Thalassiosira gravida* cultures, seawater samplings, and incubations. For at least 48 h, the polycarbonate labware was soaked in 1 N HCl, whereas the more resistant PE

containers were decontaminated with 6 N HCl, except for the nutrient samples, which were collected in 1 N HCl acid-cleaned PE vials ($Si(OH)_4$) and glass vials (NO_3^-, NH_4^+ and PO_4^{3-}). They were thoroughly rinsed with ultrapure water (18.2 MΩ cm^{-1}, Millipore Milli-Q Element ultrapure water system) before use. All procedures prior to the incubations were carried out in a class-100 laminar flow bench.

Chemical and biological parameters—Samples for the dissolved Fe measurement were filtered on 0.1-µm Nuclepore polycarbonate membrane filters and acidified to pH<2 with Ultrapure HNO_3 (Ultrex, JT Baker). Dissolved Fe concentrations were measured by flow injection analysis according to a chemiluminescence method adapted from *Obata et al.* (1993) (*Sarthou et al.,* 2003). The purification of the luminol solution through a column of 8-hydroxyquinoline immobilised on hydrophilic vinyl polymer (TSK-8-HQ after *Dierssen et al.,* 2001) improved both the blank and detection limit of the method. The blank is determined as the mean of five measurements of a low iron concentration sample with only 5 s of preconcentration and is equal to 0.067±0.02 nM. The detection limit is equal to 0.037±0.01 nM. The individual contributions to the total blank of hydrochloric acid, ammonia, and ammonium acetate buffer were determined by addition of increasing amounts of these reagents to the sample and were below the detection limit.

Nutrients were determined in 0.45 *µ*m membrane (Sartorius cellulose-acetate) filtered seawater according to the methods described in *Grasshoff et al.* (1983).

Chlorophyll *a* collected on 0.8µm Nuclepore membrane was measured fluorimetrically following *Yentsch and Menzel* (1963) after 90% v:v acetone extraction (12h) in the dark at 4°C.

Phytoplankton abundance was determined by inverted microscopy (Leitz Fluovert) in samples fixed with a 1% lugol-glutaraldehyde solution after a 12h sedimentation of 5–10-ml samples in Utermöhl chambers (Hasle 1978). Special attention was given to the morphological forms of the *Phaeocystis*: free-living flagellated and non motile cells, and to the shape of the colonies. The length of the *Thalassiosira* chains was also determined. The biomass of *P. Antarctica* was estimated according to *Mathot et al.* (2000). In order to evaluate diatoms biomass, biovolumes were estimated according to *Hillebrand et al.* (1999) and converted to carbon by the empirical formulae from *Menden-Deuer and Lessard* (2000).

Phytoplankton culture— *Phaeocystis antarctica*, an Haptophycean and *Thalassiosira gravida*, a relatively large diatom (average length: 33µm and 22µm, respectively) are both frequently observed in Antarctica (e.g. *Varela et al.,* 2002, *Schoemann et al.*; 2005). Pure cultures of *P. antarctica* (strain CCMP1871) and *T. gravida* (CCMP1461) originating from Antarctica and obtained from the Guillard-Provasoli Center were

performed in natural (low-iron high-macronutrient) Antarctic seawater, without the addition of any artificial chelator (e.g. ethylediaminetetraacetic acid, EDTA) in order to preserve the equilibrium and kinetics of the various natural chemical forms of Fe (*Gerringa et al.*, 2000). The seawater was filtered on 0.2 µm porosity SARTOBRAN cartdridge and sterilized by Gamma irradiation. The algae were pre-acclimated for at least 5 generations in Antarctic seawater relatively poor in Fe (<1nM) and enriched with 2 nM Fe in 30 ml polycarbonate flasks. They were grown at 2°C with a 18 : 6 dark : light (DL) cycle under light intensity of 180 µmol quanta $m^{-2} s^{-1}$, corresponding to saturating conditions in a growth cabinet (RUMED).

For the process-studies, *Phaeocystis* and *Thalassiosira* were grown in 20-liter polycarbonate carboys (Nalgene). *Phaeocystis* and *Thalassiosira* cultures were prepared with Antarctic sea water collected in the South-Western Pacific Antarctic Ocean (135°E - 150°E) during CLIVAR SR3 cruise in Nov-Dec 2001 respectively. Contrary to the seawater used in the case of *Phaeocystis* cultures, which was rich enough in macronutrient, in order to avoid growth limitation due to the macronutrients, the Antarctic seawater used for *Thalassiosira* cultures had to be enriched to reach final concentrations of 50 µM $Si(OH)_4$, 30 µM NO_3.and 2 µM PO_4.

Those macronutrients have been purified from potentially contaminating Fe on a Chelex 100 column. The *Phaeocystis* Fe-amended culture was enriched with 4 nM $FeCl_3$ 24h before the start of the culture and the *Thalassiosira gravida* with an initial addition of 2 nM $FeCl_3$ and a second addition of 2 nM during the course of the exponential growth phase. 15 ml of pre-culture in exponential growth phase was added to the 20L seawater.

Radiotracer experiments—Three kinds of incubations with radiotracers were performed in order to assess the effect of Fe on the photosynthesis, Fe uptake rates and growth. Incubations with radiotracers (^{14}C, ^{55}Fe) were performed on the cultures during the exponential growth of the algae and when biomass had reached concentration high enough to achieve good sensitivity (Chl*a* >0.05 µg l^{-1}). The cultures were maintained in the dark for at least 4 h before starting the radiotracer experiment, which allowed the cells to reach their basal metabolism.

In order to determine the photosynthetic parameters -the photosynthetic efficiency, α; the index of photoinhibition, β; the maximal specific rate of photosynthesis normalized to Chl*a*, P^B_{max}, the maximum realized photosynthesis rate, P_m, and the light adaptation parameter, E_k- P/E curves were determined from the measurement of ^{14}C-bicarbonate assimilation in a temperature controlled "photosynthetron" as described by *MacIntyre et al.* (1996). Subsamples of 5ml were spiked with 5 µCi of $H^{14}CO_3$ and incubated at different light intensities (0-600 µmol quanta $m^{-2} s^{-1}$) for 2-2.5 hours to measure the photosynthetic carbon fixation and to minimize radiocarbon losses by

respiration. After incubation, the excess inorganic ^{14}C was degassed for 24 h after addition of 6N HCl. Radioactivity was determined by liquid scintillation (scintillation cocktail Ecolume) with a Packard Tri-Carb (2100 TR) analyzer. The photosynthetic parameters were estimated from the photosynthesis-irradiance curves fitted with the nonlinear fitting method of Marquardt-Levenberg using Platt's equation *(Platt et al.,* 1982)

Parallel time-course incubations of ^{14}C and ^{55}Fe were conducted at constant saturating light intensity (180 µmol quanta m^{-2} s^{-1}). Subsamples of 300ml were spiked with 185 kBq ^{55}FeCl$_3$, corresponding to an addition of max. 2% of the dissolved concentration of Fe initially present in the sample. Parallel radiocarbon incubations of 100ml samples were conducted with a final concentration of 100 µCi l^{-1} sodium ^{14}C bicarbonate. The labeled samples were incubated in an illuminated growth cabinet at 2°C.

After incubation, the ^{14}C-labeled samples were gravity filtered in the case of *Phaeocystis*, to avoid the squeezing and disruption of the colonies and with a vacuum <2mm Hg in the case of *Thalassiosira*. Filtrations were undertaken on 25-mm Whatman GF/F filters. ^{14}C-Whatman GF/F were acidified (HCl 0.1N) to eliminate excess inorganic carbon and then stored at -18°C until analysis. The ^{14}C labeled cellular material collected on filters were sequentially solubilized as described in *Lancelot and Mathot* (1985) in order to distinguish between carbon assimilated into the storage products and proteins. The ^{14}C radioactivity was determined by liquid scintillation with a Packard Tri-Carb (2100 TR) analyzer. Counting errors were 3%.

Samples labeled with ^{55}Fe were filtered on 0.8µm Nuclepore polycarbonate membrane filters of 47mm. For the determination of the intracellular uptake of Fe, samples were filtered at vacuum pressure of 0.3 atm, because only cells had to be kept intact. These filters were further washed with the inorganic reductant Ti(III) complexed by citrate and ethylenediaminetetraacetic acid to remove extracellular Fe, according to the method of *Hudson and Morel* (1989). Filtrates and filters were kept at room temperature. ^{55}Fe samples were measured by liquid scintillation with a Packard Tri-Carb (2100 TR) analyzer. Counting errors were 3%. Counting of both filters and solutions showed that no significant amount of the radiotracers was adsorbed on the walls of the containers and the filtration device. Activities were corrected for radioactive decay and quenching. The relative uptake of the labeled trace metals used in the experiments was calculated on the basis of the activity of the particles collected on the filters divided by the total activity (filter + solution), expressed in parts per thousand (ppt). Molar uptake rates were then estimated from the initial dissolved concentrations of Fe.

Sedimentation rates- Sedimentation rates were determined with the SETCOL method as described in *Becquevort and Smith* (2001).

Results and discussion

Morphology- Phaeocystis has a complex life cycle with different morphotypes for which the cells can either be "free-living" or embedded in colonies. Cells are small (2-6 μm diameter) and colonies can reach 400 μm diameter (*Mathot et al.*, 2000). *T. gravida* can be present as single cells but is also capable of forming long chains of cells. Fe limitation affected both *P. antarctica* and *T. gravida* morphology.
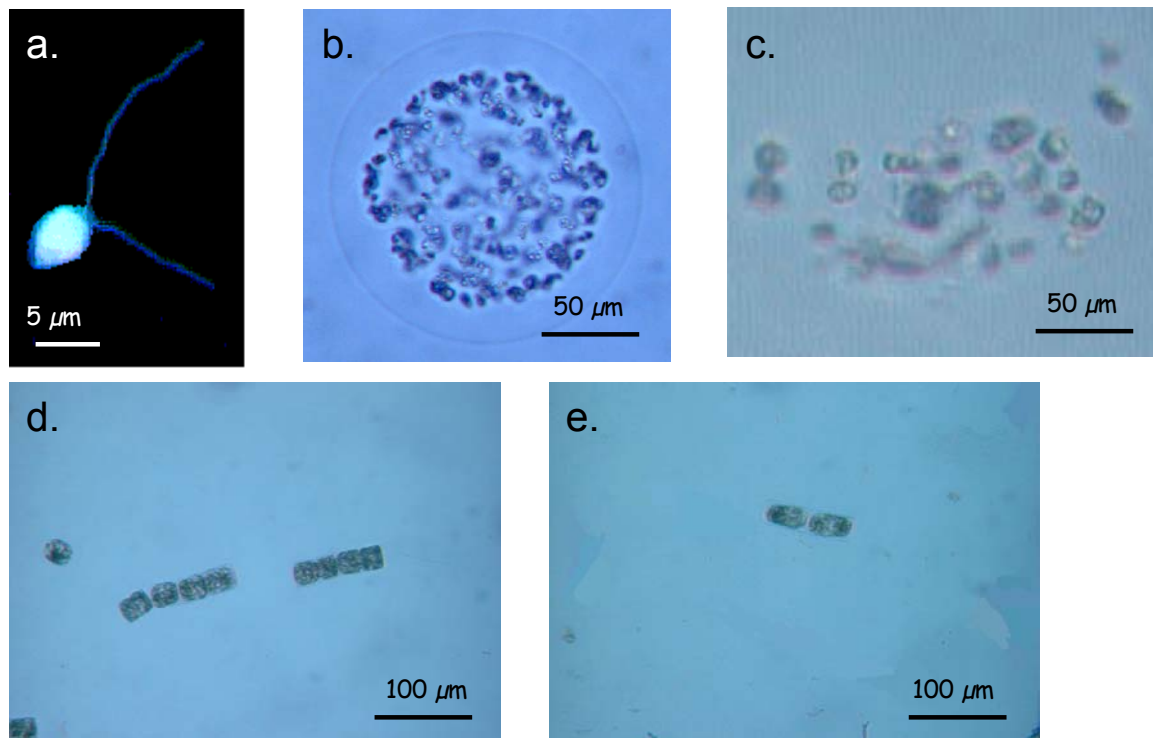
Figure I.1: Pictures of a. a flagellated cell, b. a spherical colony, c. an ellipsoid colony of *Phaeocystis antarctica*; and d. a chain of 8 cells of *Thalassiosira gravida* grown in seawater enriched in Fe (+4nM), e. a chain of 2 cells of *Thalassiosira gravida* grown in seawater non enriched in Fe (<1nM). The picture of *Phaeocystis* flagellated cell is taken under epifluorescence microscopy (1000x). The other pictures are taken under inverted microscopy (320x).

Table I.1: Dissolved Fe concentrations and algae characteristics for *Phaeocystis antarctica* and *Thalassiosira gravida* grown under Fe enriched and non-enriched conditions.

	P. antarctica		*T. gravida*	
	-Fe	+Fe	-Fe	+Fe
Dissolved Fe	0.9	2.7	0.5	3.7
chl *a* (µg l^{-1})	0.39	8.7	0.08	3.25
chl *a* / cell (pg cell^{-1})	0.05	0.24	8	20
abundance (cell l^{-1})	$7.4\ 10^6$	$3.69\ 10^7$	$9.5\ 10^3$	$1.7\ 10^5$
cell in colonies (%)	5	48	-	-
cell in chains (%)	-	-	26	59
biomass (µg C l^{-1})	32	377	4	82

Results showed an effect of Fe limitation on the formation of *Phaeocystis* colonies. At low dissolved Fe concentration (<1nM), 95% of *Phaeocystis* cells were free-living cells and only 5% were embedded into colonies (**Table I.1**). Most of those colonies had an ellipsoidal shape (**Fig. I.1.c**). In the case of the amended culture, 52% of the cells were in colonies and all colonies were spherical. According to their size (*Mathot et al;* 2000), free-living cells have surface to volume ratios (S/V) of 1.18-1.94 µm^{-1}, whereas spherical colonies of 10-400 µm of diameter have S/V of 0.60-0.02 µm^{-1}. *Ploug et al.* (1999a) demonstrated the existence of diffusion boundary layers around the colonies suggesting that colonies could be nutrient limited due to diffusion limitation. Under diffusion limitation, this concentration gradient was reflected by an apparently higher half-saturation constants for macro-nutrients uptake (N, P), K$_M$, for colonial cells compared to single cells (*Ploug et al.*, 1999b). To avoid diffusion limitation under low Fe conditions, *Phaeocystis* could adapt its morphology, keeping a small volume/surface ratio to avoid diffusion limitation. Moreover, *Phaeocystis* colony shape has also an impact on diffusive transport: the S/V ratio is greater for an elongated than for a spherical colony (**Fig. I.2**). Under nutrient limiting conditions, an elongated colony allows for a higher supply of nutrients to the cells than a spherical one.

In the Fe-amended culture of *T. gravida*, 59% of the cells were in chains and we observed chains of up to 11 cells; whereas in the non-amended culture, only 26% of the cells were in chains of max. 3 cells. However, no difference in cell biovolume was evidenced (**Table I.1**). Our results confirm previous findings on other diatoms Antarctic species showing increase in chain length after Fe addition under laboratory controlled conditions (*Chaetoceros dichaeta* et *Fragilariopsis kerguelensis,*

Timmermans et al., 2001) and during the in situ fertilizing experiment SOIREE (Southern Ocean Iron RElease Experiment, *Gall et al.*, 2001a).
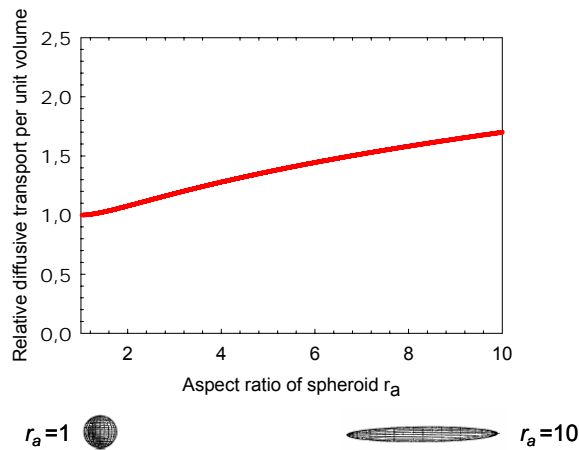
Figure I. 2: Potential diffusive transport per unit volume in function of the aspect ratio.

Chla and photosynthesis- Both for *P. antarctica* and *T. gravida*, the chlorophyll a content per cell increased significantly with Fe addition (**Table I.1**). Since Fe is needed in chlorophyll *a* synthesis, Fe limitation induces lower chlorophyll *a* concentrations per cell as shown in other previous studies (*Glover*, 1977, *van Leeuwe and Stefels*, 1998, *Kudo et al.*, 2000).

The maximum realized photosynthesis rate (P^B_{max}) of *P. antarctica* increased from 2.0 to 4.5 mgC (mg Chl*a*)$^{-1}$ h^{-1} with Fe addition (**Fig. I.3**). In contrast there was no significant change in the light adaptation parameter, E_k (36 and 31 µmol quanta m^{-2} s^{-1}, in the low Fe and amended cultures, respectively). Due to an experimental problem, those parameters could not be determined for *T. gravida*.
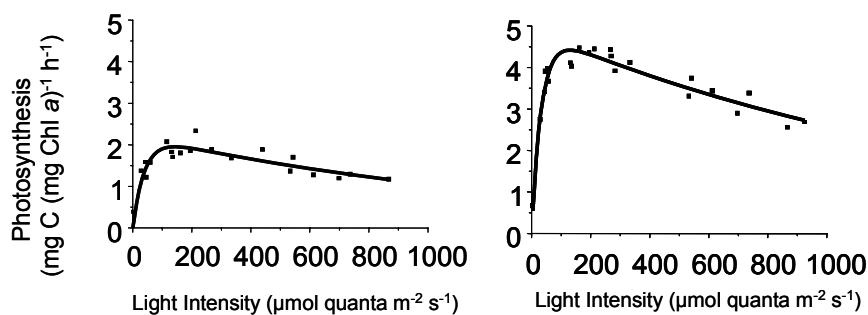
Figure I.3: Photosynthesis-irradiance curves for *Phaeocystis antarctica* grown in non enriched (left) and enriched seawater (right).

Fe uptake and carbon assimilation-

In the case of the experiment conducted on *Phaeocystis Antarctica* (**Fig. I.4**) we observe an increase in the specific assimilation of Fe (per cell) whereas the assimilation of Fe (per cell) of *Thalassiosira gravida* was similar in both enriched and non-enriched cultures. It is important to note, as discussed above, that the dominating morphological forms were different for the 2 treatments: 92% of the cells were small flagellated free-living cells in non enriched seawater whereas only 35% were small flagellated free-living cells in the case of the amended culture. *Mathot et al.* (2000) estimated the biomass of the colonial cells to be approximately 4 times higher (13.6 pg/cell) than the flagellated cells (3.3 pg/cell). This could explain the higher Fe requirement/cell of the *Phaeocystis antarctica* Fe amended culture. Similarly, the production rate of proteins/cell was 4 times higher in the enriched culture (**Fig. I.4.d**). The intracellular Fe to total carbon ratios (Fe:C_{tot}) obtained for the diatoms cultures were similar for both Fe conditions and were in the range of value usually observed for phytoplankton >10µm (**Table I.3**). On the contrary, higher Fe:C_{tot} ratio was estimated for *Phaeocystis* grown in the non amended Antarctic seawater.
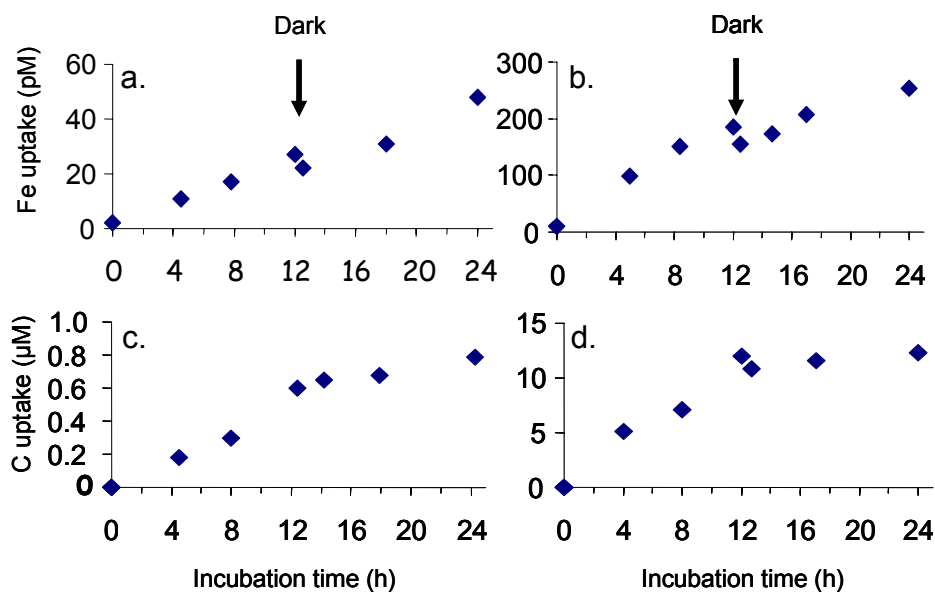
Figure I.4: Light-Dark kinetics of Fe uptake (a,b) and C assimilation in proteins (c,d) for *Phaeocystis antarctica* grown grown in: a,c. non enriched and b,d. enriched seawater.

This could also be explained by the difference in the dominance of the morphotype. Proportionally to the intracellular Fe uptake, the carbon uptake would be higher for *Phaeocystis* colonies than for free-living cells due to the carbon assimilated for the production of mucus. If we only take into account the carbon assimilated in proteins, this difference in ratio (Fe:C_{prot}, **Table I.2**) is reduced, but still remains twofold higher.

This is not due to a decrease in Fe intracellular uptake, which was as expected higher in the case of the Fe enriched culture, but was partly due to changes in the production of proteins.

The Fe:C_{tot} ratio estimated for *Phaeocystis* grown in the non-amended seawater was similar to those observed for small sized (<5µm) phytoplankton (**Table I.3**).

Table I.2: Fe uptake and growth parameters for *Phaeocystis antarctica* and *Thalassiosira gravida* grown in non enriched and enriched seawater.

	Phaeocystis antarctica		*Thalassiosira gravida*	
	-Fe	+Fe	-Fe	+Fe
Fe light uptake (pmol l^{-1} h^{-1})	2.1	20.6	0.21	3.0
Fe dark uptake (pM h^{-1})	2.3	11.8		
Fe light uptake (mol h^{-1} $cell^{-1}$)	2.8 10^{-19}	5.6 10^{-19}	2.2 10^{-17}	1.8 10^{-17}
Light production of proteins (mol h^{-1} $cell^{-1}$)	6.4 10^{-15}	25.7 10^{-15}	1.6 10^{-13}	5.7 10^{-13}
Fe:Ctot	28	10	9	6
Fe:Cproteins	44	22	133	31

Table I.3: Reported values of Fe:C cell uptake ratios for HNLC areas.

	Fe:C	References
North East Pacific		
Picoplankton	26-58	*Schmidt and Hutchins*, 1999
Phytoplankton >5µm	7-10	*Schmidt and Hutchins*, 1999
Southern Ocean		
Pico/nano- dominance	52-78	*Boyd et al.*, 2001
<10µm cell dominance	16-54	Schoemann, unpubl. data
>10µm cell dominance	6-19	Schoemann, unpubl. data
Phaeocystis antarctica	28	This study –low Fe
Phaeocystis antarctica	10	This study –high Fe
Thalassiosira gravida	6-9	This study

Sinking rates-

No sedimentation was observed for *Thalassiosira gravida* in both Fe amended and non amended cultures and for *Phaeocystis antarctica* at low Fe, whereas a relatively low potential sinking rate (0.13 d^{-1}) was measured at higher Fe concentrations cultures of *Phaeocystis*. There was no free-living cell sedimentation and colony sedimentation mainly occurred as aggregates. These sinking rates were comparable to those estimated for *P. antarctica* in the Ross Sea in Spring (0-0.19 m d^{-1}; *Becquevort and Smith*, 2001).

Conclusions

Diatoms and the non-siliceous Haptophyceae *Phaeocystis* adapt their morphology in function of the available Fe in order to reduce their surface to volume ratio and avoid diffusion limitation. Changes in the morphological forms constrained by the Fe conditions are shown to result in different physiological responses with different biogeochemical implications. The morphological form of *Phaeocystis* is important in determining its fate in the planktonic food web and the resulting efficiency of the biological pump. Free-living cells can lead to a carbon retention microbial food-web; whereas the fates of the colonies can either participate to the microbial food web by liberating single cells or lead to C export by producing aggregates.

I.2. Effect of Iron on new production

The ability to model new production is important for prognostic studies of the global carbon cycle, as new production represents the "exportable" fraction of carbon from the photic zone (*Eppley and Peterson*, 1979). Thus, the study of N-uptake, and especially the variation of the *f*-ratio (the relative fraction of new vs. total production) in response to environmental variations, is of great importance in the scope of export production studies. Three environmental parameters that strongly affect the *f*-ratio are: (1) ammonium concentration, (2) light and (3) iron availability. As ammonium is preferentially used by phytoplankton and can inhibit nitrate uptake (*Dortch*, 1990), an increase in ammonium concentration leads to a decrease of *f*-ratio (*Elskens et al.*, 2002). In addition, nitrate reductase — the enzyme involved in the reduction of nitrate to ammonium within the cell — is light- and iron-dependent, whereas ammonium uptake does not require light or iron. Thus, when light is limiting, nitrate utilization is reduced (*Armstrong,* 1999) and consequently *f*-ratio decreases. Similarly, low iron concentration (as in HNLC areas) decreases the *f*-ratio (*Cochlan et al.*, 2002).

With natural phytoplankton assemblage, the *f*-ratio response to ammonium or iron addition is shown schematically in **Figure I.5**. This response is strongly dependent on initial conditions (ammonium, nitrate and/or iron availability), and the combined effects of additions of iron and ammonium are not well known. Based on the results of an optimization model of iron-light-ammonium co-limitation on nitrate uptake, *Armstrong* (1999) argued that the variation of *f*-ratio with ammonium concentration evolves from a hyperbolic-type relationship (asymptotic decrease of *f*-ratio with increasing ammonium concentration) when phytoplankton are iron-replete, to a linear-type relationship (*f*-ratio reaches zero at a given ammonium concentration) when phytoplankton are iron-limited.
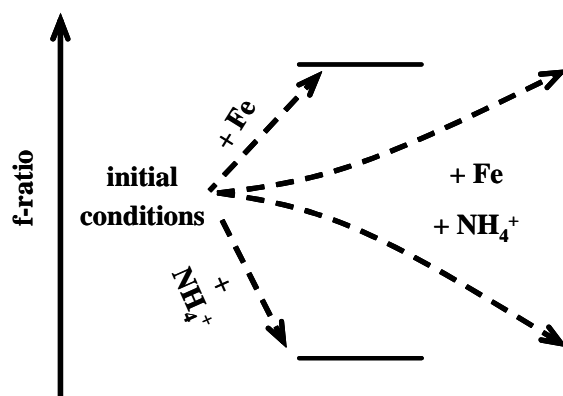
Figure I.5: Possible effects of ammonium and iron additions on *f*-ratio.

In the present study, we discuss results of shipboard experiments which examine effects of both ammonium and iron concentration on N-uptake and *f*-ratio in natural plankton assemblages in the Southern Ocean south of Australia.

Sampling

Experiments were conducted during the CLIVAR SR3 cruise (Oct. 30 – Dec. 14, 2001) in the SubAntarctic Zone (SAZ), Polar Front Zone (PFZ) and Antarctic Zone – South (AZ-S) between Australia and Antarctica. Seawater was sampled using a trace-metal clean pumping system and collected into pre-cleaned carboys for two incubation treatments: one with added iron (+1.8 nM) and one without (control). Ambient surface-water dissolved iron levels were 0.26, 0.14 and 0.11 nM at the SAZ, PFZ and AZ-S sites, respectively (see below, **Figure I.6**). After incubation of the samples at simulated in-situ conditions for ca. one week (time for significant phytoplankton biomass accumulation after Fe addition) we measured the uptake of nitrate, ammonium and urea, in the control and iron-enriched treatments, both with and without added ammonium (0.2, 0.4 and 0.9 µM). Uptake rates were determined from ^{15}N tracer experiments and inverse modeling (*Elskens et al.*, 2002). To avoid

any light effect on N-uptake, incubations were carried out at constant saturated irradiance within a thermostated cabinet. Analyses were performed via Elemental Analyzer – Isotope Ratio Mass Spectrometer.

Effects of Ammonium and Fe contents on N-uptake and f-ratio

The initial ammonium NH_4^+ concentrations in the SAZ, PFZ and AZ-S samples were 0.25, 0.23 and 0.05 µM, respectively. Addition of 1 µM of ammonium to these samples respectively (**Figure I.7**). While it is clear that ammonium addition enhances ammonium uptake it lowers nitrate and urea uptake (not shown).

0: no NH_4^+ addition
1: + 0.21 µM NH_4^+
2: + 0.43 µM NH_4^+
1: + 0.91 µM NH_4^+
+Fe: + 1.8 nM Fe
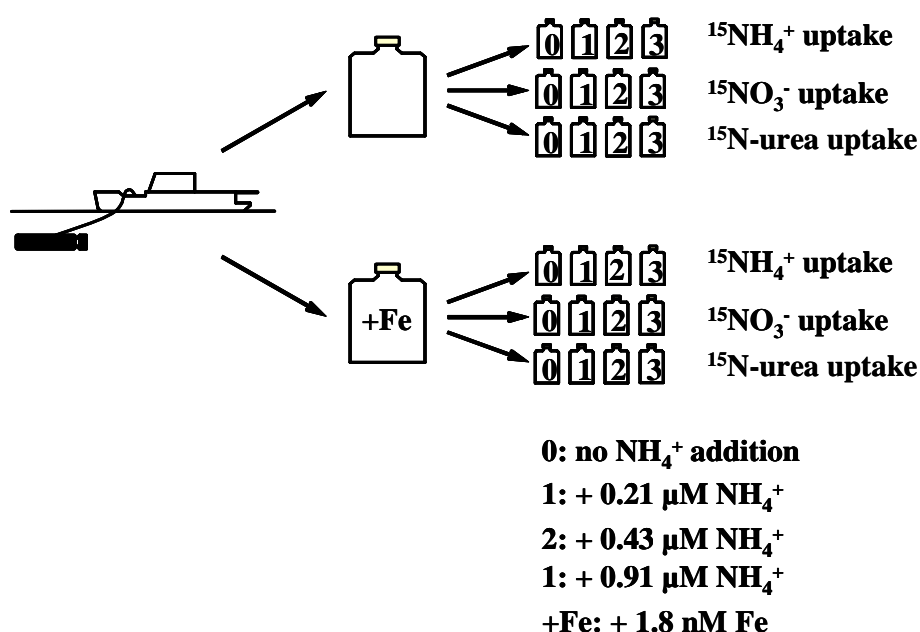
Figure I.6: Sampling strategy and additions of ammonium and Fe.
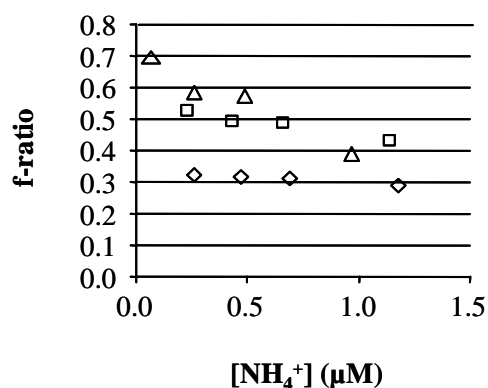
Figure I.7: f-ratio for vs. $[NH_4^+]$ conc. Fe added.
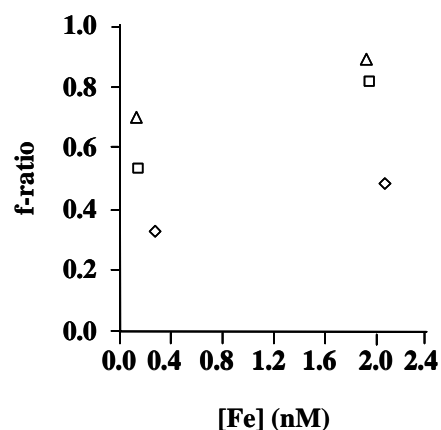
Figure I.8: f-ratio vs. Fe content no no NH_4^+ added.

Iron enrichment (addition of 1.8 nM Fe) enhanced nitrate (3-7x), ammonium (2x) and urea (1.2-2x) uptake rates (not shown) and *f*-ratio values increased by 0.15 (46%), 0.29 (55%) and 0.19 (27%), for SAZ, PFZ and AZ-S samples, respectively (**Figure I.8**).

Combined effect of ammonium and iron addition on f-ratio

The combined effects of ammonium + iron addition are not simply aditive. Indeed, adding ammonium to an Fe-enriched sample does not lower the *f*-ratio in the same way as for an Fe-depleted sample (**Figure I.9**).
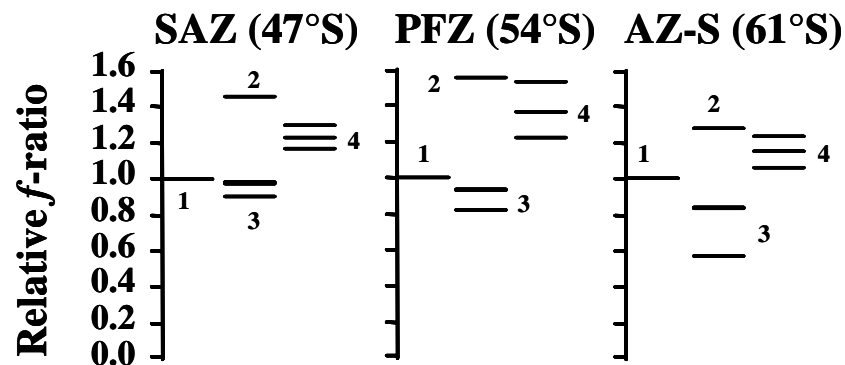
Figure I.9: Relative change of *f*-ratio due to single and combined effects of ammonium and Fe addition (relative *f*-ratio = 1); 1= no NH_4^+, no Fe; 2= +Fe (1.8 nM); 3= $+NH_4^+$ 0.2, 0.4, 0.9 µM; 4= $+NH_4^+$, + Fe.

Figure I.10 reports the slopes of the *f*-ratio regressions vs. $[NH_4^+]$. At the SAZ and PFZ sites (original $[NH_4^+]$ = 0.25 and 0.23 µM, respectively) *f*-ratio decrease is more pronounced as a result of NH_4^+ addition (slope more negative) for the Fe-amended samples, while at the AZ-S site (original $[NH_4^+]$ = 0.05 µM) *f*-ratio decrease is less pronounced for the Fe-amended sample.

Figure I.11 illustrates that Fe addition does not increase the *f*-ratio in a unique manner but that this depends on ambient ammonium concentration. However, whereas the difference of *f*-ratio between Fe-deficient and Fe-replete seawater decreases with increasing ammonium concentration at the SAZ and PFZ sites, this difference increases with increasing ammonium concentration at the AZ-S site. The reasons for the different behavior at the AZ-S site are not known: Is it due to different initial NH_4^+ conditions, different plankton assemblages or some other factor?
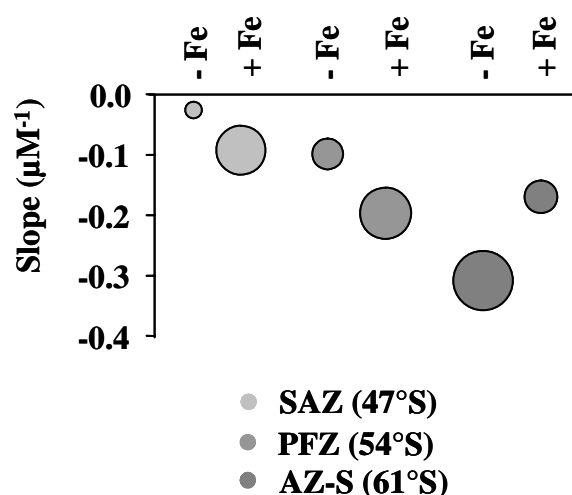
Figure I.10: Slope of *f*-ratio vs. [NH$_4^+$] regressions at the three study sites with (+Fe) and without (-Fe) iron addition. The size of the bubbles corresponds to the uncertainty of the slope.
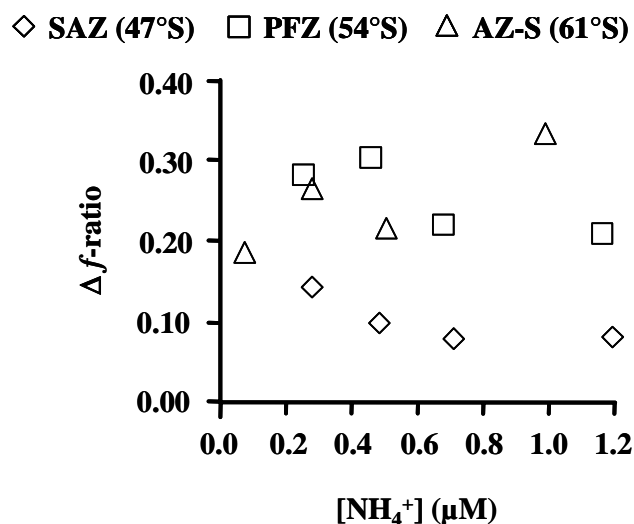
Figure I.11: *f*-ratio difference (Δ*f*-ratio) between Fe-replete and Fe-depleted experiments *vs.* ammonium concentration.

The experiments we conducted in the SAZ, PFZ and AZ-S of the Southern Ocean confirmed that the *f*-ratio is lowered by ammonium addition and enhanced by iron addition in HNLC areas. The originality of this study is that the combined effects of ammonium and iron on *f*-ratio were investigated in addition to their individual effects. The results indicate that this combined effect does not result from the simple addition of individual effects and that the enhancement of the *f*-ratio due to Fe addition depends on the ambient ammonium concentration. However the relationship

between this enhancement and ammonium concentration is at present not fully understood.

Our results imply that there is no simple relationship between export production and iron availability. Ammonium appears to counter the effects of iron addition on export production, particularly for HNLC areas such as the Southern Ocean.

I.3. Assessment of Si-nutrient source and utilisation via a new proxy: Si isotopic composition.

Silicon isotope variations are important to estimate Si nutrient utilisation since they offer a means to track sources and magnitude of silicon transport and transformation within the ocean (*De La Rocha et al.*, 1997; *De La Rocha et al.*, 1998; *Brzezinski et al.*, 2002; *Varela et al.*, 2004; *Cardinal et al.*, 2005-GBC). Till recently such studies were scarce because of analytical difficulties. These have been partly overcome since the development of Multi-Cup ICP-MS techniques (*De La Rocha*, 2002; *Cardinal et al.*, 2003).

I.3.1 Methodology

During BELCANTO II we developed a method for precise analysis of Si isotopic composition, using a Nu Instruments Plasma multicollector inductively coupled plasma mass spectrometer (MC-ICP-MS) in dry plasma mode and a Cetac Aridus desolvating nebulization system (*Cardinal et al.*, 2003). We measure Mg isotopes in dynamic mode for adequate correction of instrumental mass bias, applying the exponential fractionation law and external normalisation. The repeatability and the internal precision of the $\delta^{29}Si$ measurements on a 1ppm Si solution in dilute HF/HCl is better than $\pm$ 0.1 ‰ ($\pm$ 2σ). The accuracy has been assessed by cross analysis of an in-house standard with the laser fluorination - isotope ratio mass spectrometry (IRMS) and different MC-ICP-MS systems (see *Carignan et al.*, 2004). This new dry plasma methodology has improved sensitivity 100 times as compared to former wet plasma MC-ICP-MS (De La Rocha, 2002).

Analysis of Si isotopic composition of silicate in seawater requires a purification step by co-precipitation of Si with a triethylamine molybdate, TEA-Moly (*De La Rocha et al.*, 1996, adapted from *De Freitas et al.*, 1991). However, this purification step is inefficient when $Si(OH)_4$ concentrations drop below 10 µmol l^{-1}. In, We have applied and tested (*Cardinal et al.*, 2005) an additional pre-concentration step adapted by *Brzezinski et al.* (2003a) from the MAGIC method (*Karl and Tien*,

1992). It consists in precipitating Si(OH)$_4$ along with brucite (Mg(OH)$_2$) by increasing the pH with ammonium hydroxide, centrifugation and redissolution in HCl. For silicate replete samples we observed no systematic difference in isotopic composition between treatments with and without this extra pre-concentration step (*Cardinal et al.*, 2005-GBC). With a Si recovery > 95 % we validated for the first time the use of this approach for the determining the Si isotopic composition of silicate in in Si-depleted seawater.

I.3.2 The CLIVAR-SR3 expedition
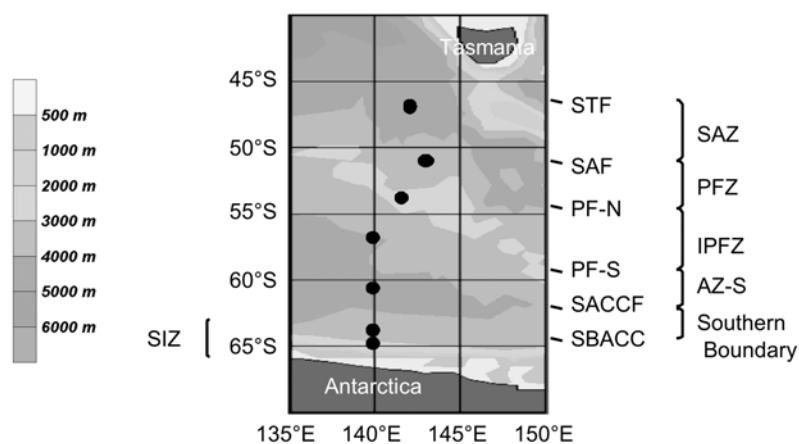
Figure I.12: CLIVAR-SR3: station location. STF: Sub-Topical Front; SAF: Sub-Antarctic Front; PF-N and PF-S: northern and southern branches of the Polar Front, respectively; SACCF: Southern Antarctic Circumpolar Current Front; SBACC; Southern Boundary of the Antarctic Circumpolar Current; SAZ: Sub-Antarctic Zone; PFZ: Polar Front Zone; IPFZ: Inter-Polar Front Zone; AZ-S: southern Antarctic Zone; SIZ: seasonal Ice Zone. See *Trull et al.* (2001a) and references therein for definition of fronts and zones.

Seawater and suspended matter were sampled during spring 2001 along a north - south transect at 140°-144°E (CLIVAR SR3, cruise #AU0103, Oct. 29 - Dec. 11 2001, R/V *Aurora Australis*), in the Australian sector (**Figure I.12**). The stations sampled were located in the following Antarctic zones (defined and described in Trull et al., 2001a and Orsi et al., 1995): the Subantarctic Zone (SAZ, stations at 46.7° and 48.8°S); the Subantarctic Front (SAF, station at 51.0°S); the Polar Front Zone (PFZ, station at 53.7°S); the Interpolar Front Zone (IPFZ, station at 56.9°S); the southern Antarctic Zone (AZ-S, station at 60.9°S) and two stations under sea ice influence. The latter are located between the Southern Antarctic Circumpolar Front (SACCF)

and the Southern Boundary (station at 63.9°S) and between the SB and the Antarctic Slope Front (station at 64.9°S). The stations at 63.9°, 60.9° and 51.0°S were visited again on the way back north, after 11, 17 and 31 days, respectively. The two southernmost stations are reported further as located in the Seasonal Ice Zone (SIZ). Only the site at 63.9°S was actually covered by sea ice at the time of sampling, while at 64.9°S, a site visited 10 days later, melting had taken place and sampling occurred in partially ice-free conditions. A summary of samples and proxies acquired from this cruise is given in **Table I.4.**

I.3.3 Results and discussion
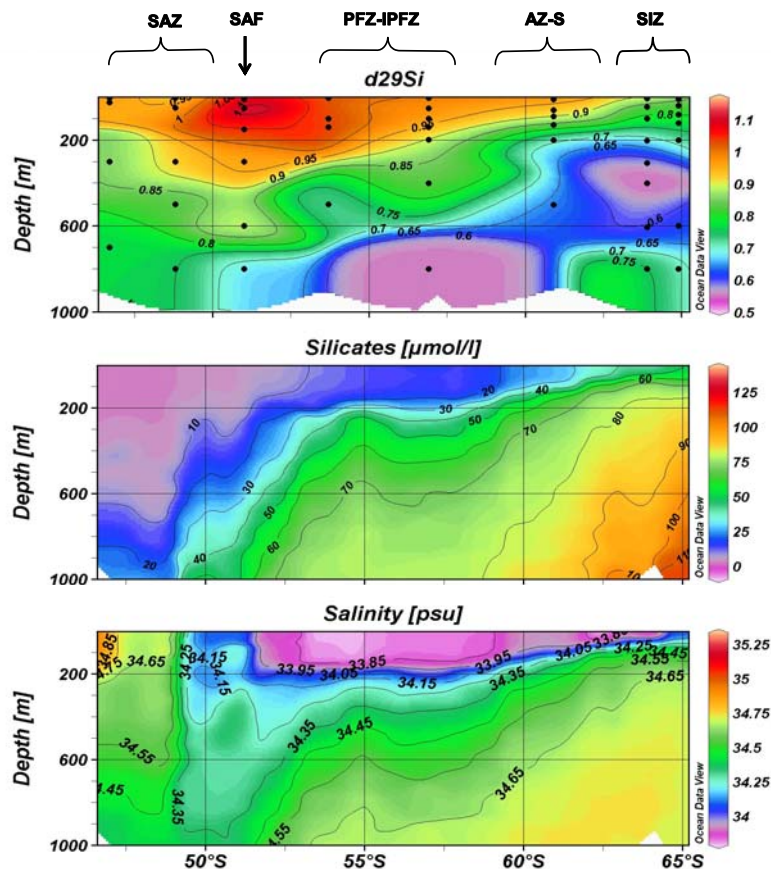
Figure I.13: CLIVAR-SR3 section at 140°E (spring 2001). Si isotopic composition of silicicacid (top); silicic acid concentration (middle); salinity (bottom) in the upper 1000m.

Complete water column profiles of δ^{29}Si-silicic acid are given in *Cardinal et al.* (2005-GBC). **Figure I.13** shows the latitudinal distribution in the upper 1000m for δ^{29}Si-silicate, silicic acid concentration and salinity. At all locations Si isotopic composition is heavier in surface waters, similar to what is reported for $\delta^{15}NO_3^-$

(*Sigman et al.,* 1999; *Altabet and François*, 2001; *Karsh et al.*, 2003). Average δ^{29}Si signatures for different depth ranges were as follows.

Table I.4: Summary of proxies analysed by MRAC-VUB during CLIVAR-SR3

Zone	Latitude	depth layer	Ba_d[1]	Ba_{xs}[2]	^{15}N-uptake[3]	[234]Th[4]	$\delta^{29}Si_{DSi}$[5]	$\delta^{29}Si_{BSi}$[6]
SAZ	47	upper layer	x	x		x	x	
		mesopelagic	x	x		x	x	
		deep	x				x	
SAZ	49	upper layer	x	x	x		x	
		mesopelagic	x	x			x	
		deep	x				x	
SAF	51	upper layer	x	x	x	x	x	
		mesopelagic	x	x		x	x	
		deep	x				x	
SAF-Repeat	51	upper layer		x	x			
		mesopelagic		x				
		deep						
PFZ	54	upper layer	x	x	x	x	x	x
		mesopelagic	x	x		x	x	
		deep	x				x	
IPFZ	57	upper layer	x	x	x	x	x	x
		mesopelagic	x	x		x	x	
		deep	x				x	
AZ-S	61	upper layer	x	x	x	x	x	x
		mesopelagic	x	x		x	x	
		deep	x				x	
AZ-S Repeat	61	upper layer		x	x	x	x	x
		mesopelagic		x				
		deep						
SIZ	64	upper layer	x	x	x	x	x	x
		mesopelagic	x	x		x	x	
		deep	x				x	
SIZ Repeat	64	upper layer		x	x	x	x	x
		mesopelagic		x				
		deep						
SIZ	65	upper layer	x	x	x	x	x	x
		mesopelagic	x	x		x	x	
		deep	x				x	

[1] Dissolved Ba as a water mass tracer - Data from Jacquet et al. (2004) - Note that this is a high resolution transect, i.e. 53 stations have been analysed and not only 8 as listed in this table

[2] Excess Ba as proxy of mesopelagic remineralisation - Data from Cardinal et al. (2005b)

[3] N-uptake as a proxy of New Production - Data from Savoye et al. (2004a)

[4] [234]Th as a proxy of particle export from surface and particle remineralisation in the mesopelagic zone - Data from Savoye et al. (2004b)

[5] Si isotopic composition of seawater as a proxy of Si utilisation and water masses - Data from Cardinal et al. (2005a)

[6] Si isotopic composition of biogenic silica as a proxy calibration (nutrient utilisation) - Data from Cardinal et al. (submitted)

upper layer: mixed layer or upper 200m
mesopelagic: 200-500 or 200-1000m
deep: 1000-bottom

Within the mixed layer: 0.97 ± 0.09‰ (n = 14); in mesopelagic waters (200-1000 m): 0.70 ± 0.11‰ (n = 28); in deep waters (>1800 m): 0.62 ± 0.06‰ (n = 30). Such values are in good agreement with the few existing data for the Southern Ocean: 1.19 ± 0.25‰ (n=8), surface waters

during spring (*Varela et al.*, 2004); 0.67 ± 0.05‰ (n=5), 0.57 ± 0.04‰ (n=9), intermediate and deep waters, respectively (*De La Rocha et al.*, 2000).

Our averaged deep-water signature is also close to the estimate of the oceanic steady state signature (0.70‰) obtained from a model simulation (*Wischmeyer et al.*, 2003).

Deep water signatures

In general, deep waters are isotopically homogeneous and do not show large changes of $\delta^{29}Si$ with latitude and depth; for all deep (>1800m) samples combined, the standard deviation (σ) is 0.06‰, what is only slightly larger than the value for reproducibility. This contrasts with the situation for silicic acid, showing concentrations to increase with depth. The absence of a systematic decrease of $\delta^{29}Si$ below 1800m suggests that progressive opal dissolution at depth is not large enough to significantly impact the isotopic composition of silicic acid there.

The $\delta^{29}Si$ signature of bottom water (2550 m) at 64.9°S is heavier by 0.14‰ compared to the value at 1900m. This trend is mirrored by the $Si(OH)_4$ concentration which decreases when approaching the seafloor and likely reflects the imprint of surface water sinking along the Antarctic slope in the process of Antarctic Bottom Water (AABW) formation. Bottom water formation has been reported, among other places, off Adelie Land, close to the 64.9°S site sampled here (*Rintoul*, 1998; *Orsi et al.*, 1999; *Trull et al.*, 2001a). The formation of AABW, clearly seen also from the CLIVAR-SR3 dissolved Ba data (see section II.4.1 and *Jacquet et al.*, 2004), supplies isotopically heavy waters low in $Si(OH)_4$ to the ocean abyss.

Processes in surface and mesopelagic waters

Most of the variation of Si isotopic composition occurs in the upper 1000 m layer as seen from **Figure I.13**. In the upper 600 m layer there is a clear trend of icreasing $\delta^{29}Si$ values from South to North (SIZ to SAF). The mixed layer isotopic signatures of the SAF are the heaviest observed during CLIVAR-SR-3. North of the SAF, in the SAZ, the trend reverses and surface water there are again isotopically lighter, with $\delta^{29}Si$ values similar to those for the PFZ and IPFZ. This condition is a priori unexpected since SAZ waters are Si-depleted ([$Si(OH)_4$] <5 µmol l^{-1}) compared to PFZ and IPFZ where silicic acid concentrations are 10 and 15 µmol l^{-1}, respectively. In the following section we investigate possible origins for these isotopic variations during spring in the Southern Ocean.

I.3.4. Open vs. closed models

The biologically driven Si isotopic fractionation in the mixed layer can be described, in first approximation, by two simple models:

(i) the Rayleigh type distillation model (*Mariotti et al.*, 1981; *De La Rocha et al.*, 1997) assumes a closed system (i.e. nutrient consumption is not replenished by external sources) and writes the evolution of the isotopic signal as (Eq. 1):

$$\delta^{29}Si_{Si(OH)4} = \delta^{29}Si_{initial} + {}^{29}\varepsilon \times \ln f \qquad (1)$$

(ii) the open steady-state model (e.g., *Sigman et al* 1999; *Varela et al.*, 2004) assumes a continuous supply of nutrients from the same external source (Eq. 2):

$$\delta^{29}Si_{Si(OH)4} = \delta^{29}Si_{initial} - {}^{29}\varepsilon \times (1-f) \qquad (2)$$

In equations (1) and (2), *f* is defined as:

$$f = \frac{\left[Si(OH)_4\right]_{observed}}{\left[Si(OH)_4\right]_{initial}} \qquad (3)$$

$^{29}\varepsilon$ is the fractionation factor between opal and silicic acid (note that $^{29}\varepsilon$ is negative) and can be approximated as the difference between the $\delta^{29}Si$ signature of the opal and the one of the water from where it was precipitated. $\delta^{29}Si_{initial}$ and $[Si(OH)_4]_{initial}$ are the initial Si isotopic composition and concentration of the silicic acid source i.e., the seawater properties before any Si consumption took place.

Both models assume steady-state conditions and constancy of the fractionation factor. The latter is supported by experimental work of *De La Rocha et al.* (1997). However, considering the relatively large uncertainty of ε deduced from experimental work, new estimates are needed, especially for the low temperature range of the Southern Ocean. Based on the rationale applied for $\delta^{15}N$ (e.g., *Sigman et al.*, 1999; *Altabet and François*, 2001; *Karsh et al.*, 2003), equations (1) or (2) can be used to calculate apparent ε values. Doing so and assuming constant initial conditions, *Varela et al.* (2004) obtained larger absolute ε values (-0.88‰ < $^{29}\varepsilon$ < -0.52‰) compared to the value of -0.57 ± 0.20 ‰, reported by *De La Rocha et al.* (1997). In contrast to fully controlled *in-vitro* incubations, the *in-situ* approach is delicate because equations (1) or (2) are unlikely to describe the system correctly.

Moreover, *Wischmeyer et al.* (2003) warn against potential bias of the Si isotopic signature, in cases where the initial conditions of equations (1) and (2) (concentrations and isotopic signature of the source) are not well constrained.

ε estimates: a multi-box approach

In the Southern Ocean characterized by a strong seasonality of phytoplankton growth, nutrients are supplied by vertical mixing which is particularly intense during winter and early spring, and by surface water advection from the south via Ekman drift (e.g., *Pollard et al.*, 2002; *Sarmiento et al.*, 2004). The silicate pump *Dugdale et al.* (1995) explains why Antarctic waters become relatively more Si-depleted from south to north, compared to nitrate (*Trull et al.*, 2001a; *Nelson et al.*, 2001; *Matsumoto et al.*, 2002; *Anderson et al.*, 2002; *Sarmiento et al.*, 2004). It is unlikely that the Southern Ocean operates as a single closed system for silicon isotopes at seasonal or annual time scale, especially in spring when vertical mixing can be still strong. Therefore, we applied the open system fractionation model (Eq. 2) at every station ("multiple box approach") selecting initial conditions for silicate content and isotopic composition in order to calculate the fractionation factor, $^{29}\varepsilon$. For each station, we have determined these initial conditions from the CLIVAR-SR3 profile at the estimated winter Mixed Layer Depth (MLD). In order to quantify the uncertainty inherent to this approach (e.g., inter-annual variability) we considered for each site a range of winter MLD values by calculating $^{29}\varepsilon$ values for a shallow and a deep estimate of MLD (**Table I.5**). In case no $\delta^{29}Si_{initial}$ value was available for an identified winter MLD, we selected the next closest deeper value.

The average calculated $^{29}\varepsilon$ from CLIVAR-SR3 is -0.45 ± 0.17‰ (n=13), which is not significantly different from the *De La Rocha et al.*, (1997).experimentally obtained value (-0.56 ± 0.21‰, n=13). It is likely that in our case most of the variability is due to uncertainties linked to equation (2) and the choice of the initial conditions. Although our approach is better constrained than the one based on winter nutrient data, some bias could still exist, because the sampling resolution applied here for intermediate waters, while high relative to previous studies, is still relatively coarse. Nevertheless, the reasonable standard deviation on ε estimated with the open system model, gives confidence that the assumptions we formulated regarding spring and winter Southern Ocean characteristics are sound.

The standard deviation on all estimates (**Table I.5**) is not larger than the ones from previous studies (*De La Rocha et al.*, 1997 and *Varela et al.*, 2004), despite very different phytoplankton compositions and biomasses along SR-3 transect (*Savoye et al., 2004a*; *Cardinal et al.*, 2005-GBC; *Kopczynska et al.*, submitted). This indicates that the $\delta^{29}Si$ proxy is independent of ecosystem type, validating the tool for a wide range of biogeochemical conditions.

Table I.5: Estimates of fraction factor $^{29}\varepsilon$ (open system), for winter and spring mixed layer properties.

Table 5. Fractionation factor estimates (open system), $^{29}\varepsilon$, as a function of spring and winter mixed layer properties

| Zones | Lat., | Spring surface CLIVAR-SR3 conditions | | | | Winter conditions[c] | | |
| | | Spring SR 3 MLD[a], | [Si(OH)$_4$]$_{ML}$ average, | δ^{29}Si$_{ML}$ average, | st. dev.[b], | Winter MLD, | $^{29}\varepsilon$ shallow winter MLD[d], | $^{29}\varepsilon$ deep winter MLD[d], |
	°S	m	µmol l^{-1}	‰ vs NBS28	‰	m	‰	‰
SAZ	46.9	100	2.0	0.97	0.03	400-600	-0.373	-0.258
SAZ	48.8	580	3.0	0.93	0.03	500-700	-0.392	-0.247
SAF	51.0	99	5.0	1.12	0.03	170-300	n.a.	-0.302
PFZ	53.7	76	11.0	1.02	n.a.	140-170	n.a.	-0.698
IPFZ	56.9	92	15.8	0.99	0.01	140-200	-0.443	-0.217
AZ-S	60.8	97	28.1	0.97	0.04	110-130	-0.559	-0.442
SIZ	63.9	41	40.8	0.97	n.a.	75-125	-0.624	-0.644
SIZ	64.9	104	60.7	0.84	0.03	100-200	n.a.	-0.632
						average stations southern than PFZ	-0.54 ± 0.09	-0.53 ±0.20
						average all stations	-0.48 ± 0.11	-0.43± 0.20
						All $^{29}\varepsilon$ estimates		**-0.45 ± 0.17**

[a] Mixed layer depth (MLD) during CLIVAR SR3 cruise (for the SAZ - PFZ: depth at which the density is 0.05kg.m^{-3} heavier than the surface density in accordance with *Rintoul and Trull* [2001]) and for the IPFZ - SIZ depth at which the surface density is 0.02 kg.m^{-3} heavier than the surface density in accordance with *Chaigneau et al.* [2004] Note that the MLD at 48.8°S was exceptionnally deep due to a storm before sampling and not reflected in nutricline, so we have taken 100m for this station

[b] standard deviation obtained on each station average δ^{29}Si calculated from the 1-4 samples analysed in the mixed layer (ML) for each station (cf. Table 3). n.a. when only one depth analysed in the ML for silicon isotopes

[c] Range of winter ML conditions along SR-3 transect as measured by *Rintoul and Bullister* [1999] in Sept - Oct. 1991, *Trull et al.* [2001a] and *Rintoul and Trull* [2001] in July-August 1995 and Sept. 1996

[d] ε calculated using Eqs. 2 and 3 (open system). Initial conditions were read on the spring CLIVAR-SR3 profiles (Table 3) at shallowest and deepest estimated winter MLD respectively When no isotopic data were available from such depth, the closest deeper one has been used. n.a. when the shallow winter MLD is not applicable to the CLIVAR -SR3 situation See legend caption of Fig.1 and text for definition of acronyms

A recent study on Si isotopic signatures in Lake Tanganyika further widens this conclusion to freshwater environments (*Alleman et al.*, 2005). We recognize that our average $^{29}\varepsilon$ (-0.45‰) is smaller compared to the Southern Ocean estimates reported by *Varela et al.* (2004) ranging between -0.55 and -0.98‰. However, in their study, spring and late summer values were not taken into account and they considered one single $Si(OH)_{4initial}$ source (65 µmol l^{-1}) in the calculation of *f* (equation (3)) for all stations south of the PFZ. The fractionation factor seems to be larger south of the PFZ (**Table I.5**), a feature that is discussed in the next section along with diatom Si isotopic signature and closer comparison with *Varela et al.* (2004).

<u>ε estimated from the comparison of diatoms and seawater isotopic compositions</u>
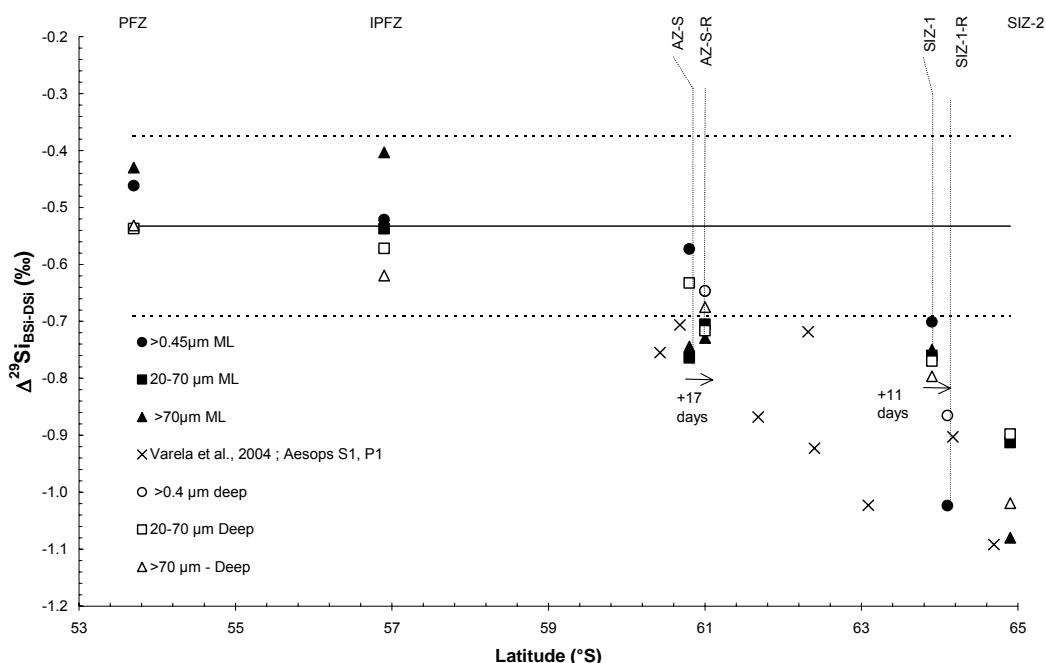
Figure I.14: CLIVAR-SR3. Latitudinal trend of $\Delta^{29}Si$, i.e. the difference between $\delta^{29}Si_{BSi}$ and $\delta^{29}Si_{DSi.}$

Within a steady-state open (Eq. 1) or closed (Eq. 2) system the difference between the isotopic composition of the instantaneous diatom product ($\delta^{29}Si_{BSi}$) and surrounding waters ($\delta^{29}Si_{DSi}$), $\Delta^{29}Si$, should be an estimate of the fractionation factor, $^{29}\varepsilon$. This assumption only holds if the isotopic compositions of both phases represent instant equilibrium conditions (i.e. same f, Eq. 3). Moreover, in case a closed system applies, $\Delta^{29}Si$ should increase along with silicic acid (DSi) consumption. *Varela et al.* (2004) obtained an average $\Delta^{29}Si$ of -0.83 ‰, giving additional support for a significantly larger ε value than the one deduced from laboratory experiments (*De La Rocha et al.*, 1997), whereas recent $\Delta^{29}Si$ values reported by *Alleman et al.* (2005)

for tropical lake diatoms are in the range of *De La Rocha et al.* (1997). In the present study, the latitudinal trend for $\delta^{29}Si_{BSi}$ is much steeper than for $\delta^{29}Si_{DSi}$ inducing latitudinally varying $\Delta^{29}Si$ values (**Figure I.14**).
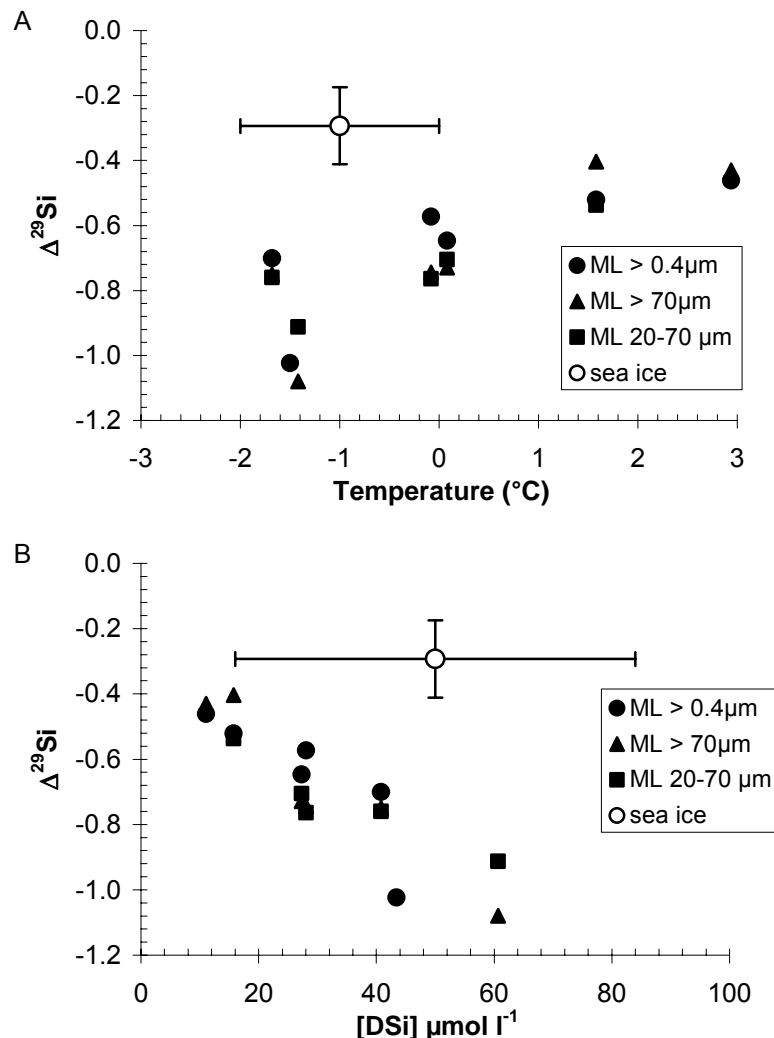
Figure I.15a,b: Mixed layer $\Delta^{29}Si$ vs. temperature (a) and [DSi] (b). Filled circles: >0.4 µm; filled squares: 20-70µm; filled squares: > 70µm; empty circles: sea ice diatoms. Temperatures and isotopic composition of sea ice diatoms (n=10) are from *Fripiat* (2005) and *Fripiat et al.* (in prep.) in cores sampled during the ARISE 2003 cruise (AU0301). Only data for temperatures > -5°C are shown because above this temperature the brine channels are open (*Golden*, 2001) and therefore $\delta^{29}Si_{BSi}$ is not likely to be biased by $\delta^{29}Si_{BSiacc}$ (*Varela et al.*, 2004). As no [DSi] contents were measured directly in the brine pockets during this cruise we have taken the range obtained by *Gleitz et al.* (1995).

A similar latitudinal trend is actually also seen on data reported by *Varela et al.* (2004). This suggests a possible change in the water-diatom silicon fractionation factor. For the PFZ-IPFZ zone $\Delta^{29}Si$ falls well in the range of our previous $^{29}\varepsilon$

estimates (**Table I.5**) and see *Cardinal et al.,* 2005) but becomes progressively more negative southward (i.e. larger isotopic difference between BSi and DSi phases). SIZ-2 and SIZ-1-R are particularly off the expected range.

Revisiting previous published data (*Brzezinski et al.*, 2001; *Varela et al.*, 2004; Cardinal et al., 2005-GBC), and taking into account the large amount of information available from the CLIVAR-SR3 cruise, we found that the parameters most likely to produce such change are temperature, DSi content and specific Si uptake and dissolution rates (*Cardinal et al.*, subm.). For instance, plotting Δ^{29}Si vs. mixed layer temperature (**Figure I.15a**) reveals a significant anti-correlation for CLIVAR-SR3 data but sea ice Δ^{29}Si data from *Fripiat et al.* (in prep.) fall completely off this trend. Although temperature is a plausible cause which cannot be ruled out yet, we believe it is unlikely to explain the observed variations. Nevertheless, the temperature effect remains to be addressed carefully by experimental growth experiments to verify if non-dependency of ε on temperature (*De La Rocha et al.,* 1997) can be extended to very low temperatures (<-1.0°C) in the SIZ. A strong correlation between DSi contents and Δ^{29}Si is also observed (**Figure I.15b**).

In this regard, hydroponic experiments on upper plants support also a larger Δ^{29}Si when DSi content of the continuous nutrient supply is higher (*Opfergelt et al.*, to be submitted) although we do not have yet satisfactory explanation to understand how these parameters could be positively correlated. These parameters are different from the ones controlling N isotopic fractionation which strengthens the picture of a decoupling between the Si and N cycles in diatoms as underlined by recent studies (*Martin-Jézéquel et al.*, 2000; *Claquin et al.*, 2002).

Yet, these results are far from being definitive proof that Si fractionation by diatoms is not constant. Many parameters vary with latitude in the Southern Ocean and finding a significant relationship amongst two, as in **Figure I.15** does not necessarily mean that one leads the other. Moreover a decoupling between δ^{29}Si$_{BSi}$ and δ^{29}Si$_{DSi}$ resulting from different and/or too small time window is also possible which should results in the undermining of the assumption Δ^{29}Si ~ $^{29}\varepsilon$ drawn based on the simple models currently available. Such biases from model rationales recorded by snapshot sampling could be dampened at the annual or multi-annual time scales and hence do not invalidate the potentials of Si isotopes as (paleo)proxy yet.

Overall even if these results highlight important gaps in the understanding of the oceanic Si isotope system, given the standard deviations of the fractionation factor estimates and the assumptions linked to the choice of the model, the differences with previous estimates are significant only in the seasonal ice zone.

II. ASSESSMENT OF CARBON FLUXES

II.1 Air-Sea exchange of CO_2

II.1.1 Air-CO_2 fluxes south of Tasmania and New Zealand.

We aimed to budget CO_2 fluxes from in situ surface partial pressure of CO_2 (pCO_2) measurements combined with Sea Surface Temperature (SST), Chlorophyll a and wind speed inferred from satellite observations. We collaborated with the Laboratoire D'Océanographie Dynamique et de Climatologie/Institute Pierre Simon Laplace (LOCEAN), the Lamont-Doherty Earth Observatory of Columbia University and the School of Environmental Sciences of the University of East Anglias to budget CO_2 fluxes in the area south of Tasmania and New Zealand (125°E-205°E; 45°S-60°S; **Figure II.1**). In situ pCO_2 measurements were carried out from December 1997 to December 1998 during several cruises: AESOPS; Astrolabe and SOIREE transects (see *Rangama et al.,* (2004) for details). SST was derived by the National Meteorological Centre from in situ and Advanced Very High Resolution Radiometer (AVHRR) data while Level 3 Sea-viewing Wild-Field-of view Sensor (SeaWIFS) chlorophyll (Chl) was obtained from the Physical Oceanography Distributed Active Archive Center (PODAAC).

Correlation of oceanic pCO_2 with chlorophyll and SST

We established biogeochemical provinces inside which in situ pCO_2 measurements appear to have a similar behaviour with respect to SST and chlorophyll. Then, inside each zone, correlations between pCO_2 and SST or chlorophyll were examined. The pCO_2-SST relationships take into account pCO_2 variability induced by mixing and thermodynamical effects. Comnininh this with chlorophyll data allows to take into account the biological effect. Three different zones were identified. The best pCO_2-chlorophyll fit (**Figure II.2**) was obtained for Chl values exceeding a 37 mg m^{-3} and corresponds to Zone "A" (**Figure II.1**).
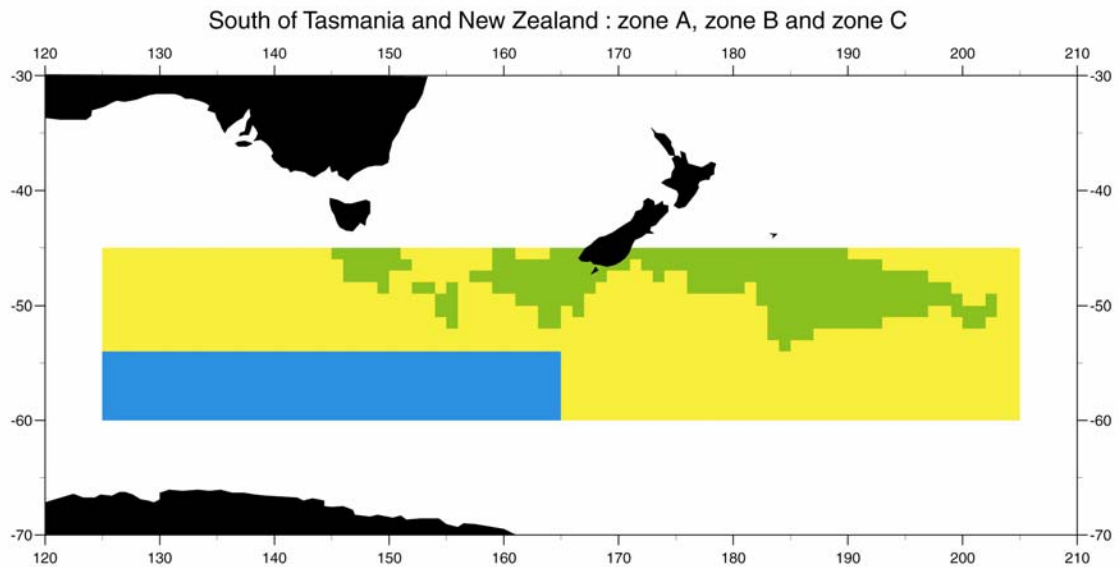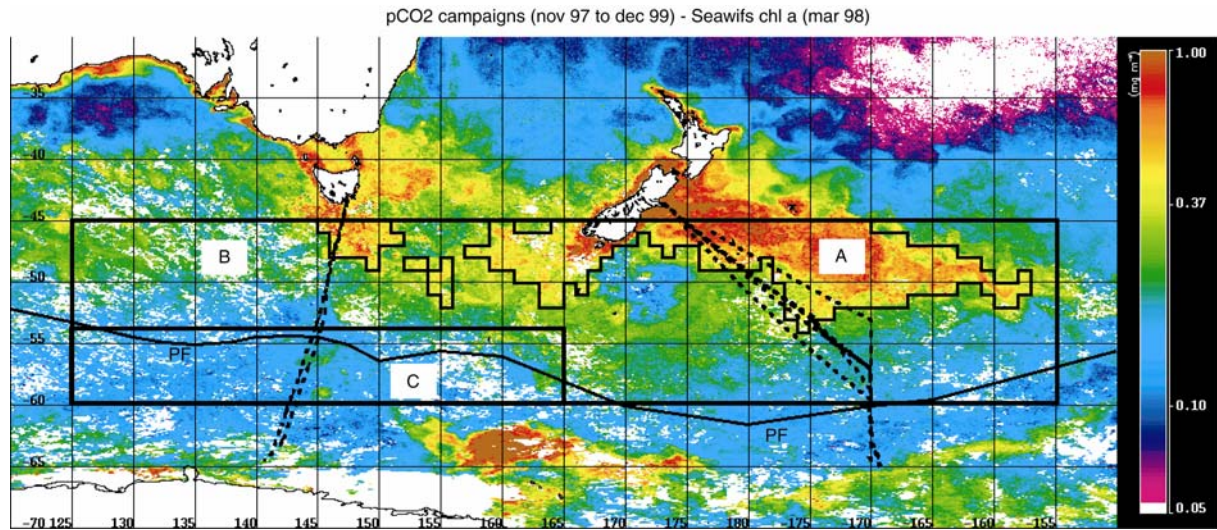
Figure II.1 : Top: cruise tracks (dashed lines; AESOPS cruises in the eastern part, Astrolabe cruises in the western part) superimposed on a SeaWiFS chlorophyll map (March 1998). The climatological Polar Front (PF) from Belkin and Gordon (1996); solid lines indicate boundaries between zones A, B, and C. Bottom: Zone A (chlorophyll-rich region; green), B (yellow), and C (blue).
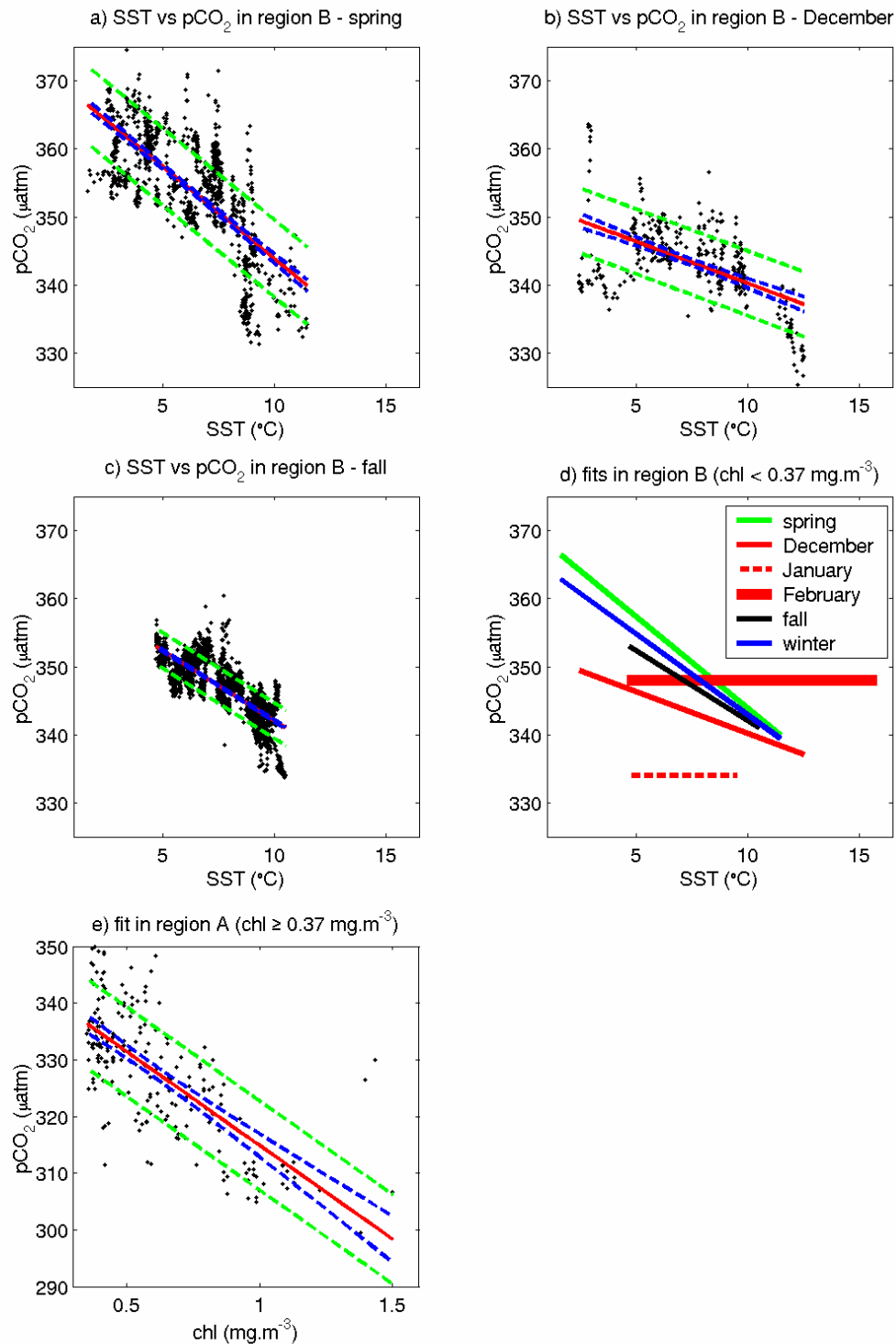
Figure II.2: Linear fit (red), its 95% confidence interval (blue dashed line), and the pCO_2 residuals with respect to the fits (±stdfit) (green dashed line) superimposed on the pCO_2–SST scatterplot for zone B in (a) spring, (b) December and (c) fall; (d) Summary of pCO_2–SST relationships (including mean values) plotted over the SST ranges covered by the measurements. (e) Same as (a) for a yearly pCO_2 chlorophyll fit in zone A (for chl > 0.37 mg m^{-3}).

High chlorophyll coincides with high SST conditions such that chlorophyll and SST appear correlated; low pCO_2 values occur at high SST, but the corresponding pCO_2-SST fit is poor and was not used in the following. In the rest of the studied area, a sharp latitudinal SST and pCO_2 gradient is observed at about 54°S on the Astrolabe measurements corresponding to the position of the Polar Front (PF) (**Figure II.1**). The remaining area was divided in two zones; zone B north of the Polar Front and zone C south of the Polar Front.

In Zone B negative correlations between pCO_2 and SST were observed for spring and fall. For January and February the pCO_2-SST correlation is poor (r<0.5), so an average pCO_2 value was used instead. Since no measurements are available for winter a pCO_2-SST relationship for winter was derived by averaging the coefficients of the pCO_2-SST fit observed for spring and fall.

In zone C no correlation between pCO_2 and SST was found, consequently a seasonal pCO_2 average derived from the Astrolabe measurements in spring and summer was used. Since no data were available in zone C during fall, averages of the AESOPS pCO_2 data, obtained for the same latitudinal range, were used. In winter, pCO_2 is assumed to be equal to the average of spring and fall values.

Reconstruction of pCO_2 fields.

The pCO_2 fields were constructed on the basis of fits between pCO_2 and SST during three periods in zone B and a yearly fit between pCO_2 and chlorophyll in zone A. **Figure II.2d** summarizes the pCO_2-SST relationships (including pCO_2 constant values). Alternative extrapolation methods were conducted to determine "methodological error" (see report to *Rangama et al., 2004*), and the method providing the best results was selected. Reconstruction of the pCO_2 fields over the studied area was performed for a full year (December 1997 to December 1998). Using the pCO_2-SST and pCO_2-Chl regressions and low resolution SST and Chlorophyll data (monthly data for 1°×1° grids) we reconstructed monthly pCO_2 fields of 1°×1° spatial resolution. A chlorophyll-rich zone (zone A) was observed from December 1997 to April 1998 and from October 1998 to December 1998, so that from May 1998 to September 1998, the study area is consists only of zones B and C without zone A. in December 1997 and January1998, chlorophyll-rich areas are also found in parts of the southwestern region (Zone C). In this case, it has been assumed that the pCO_2-Chla relationship from zone A applies.
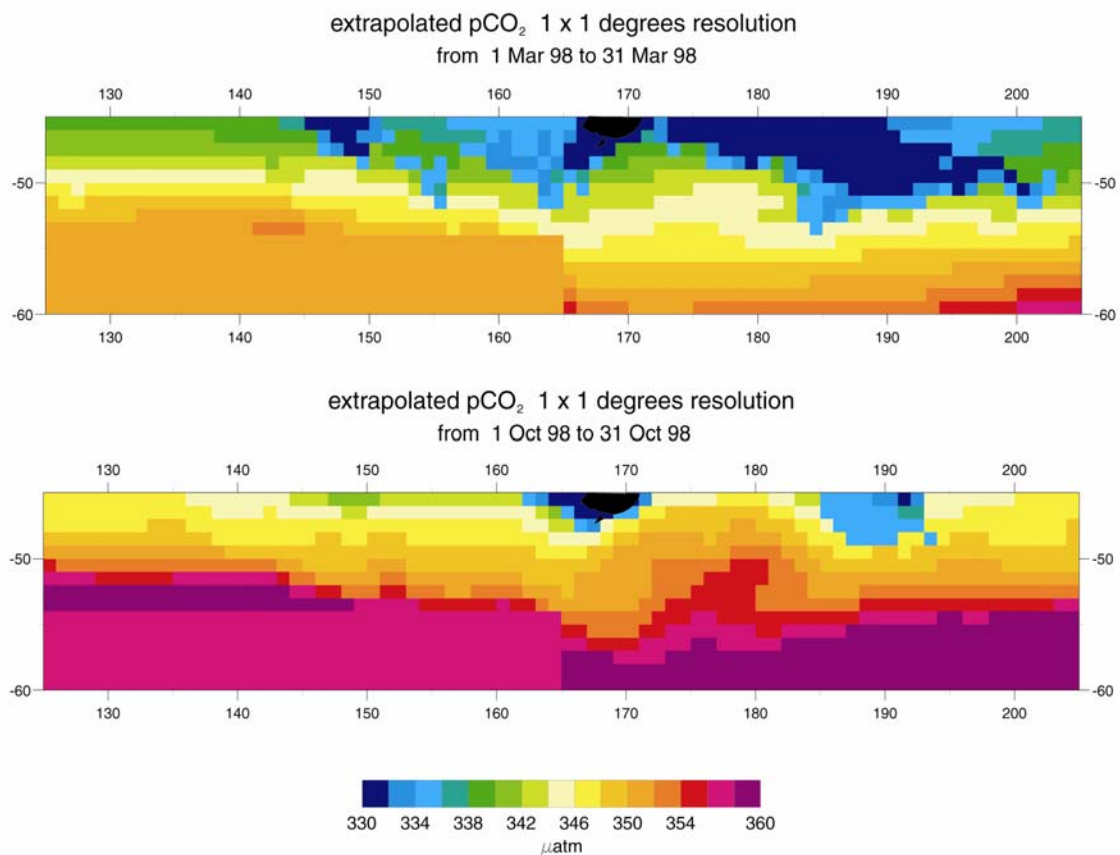
Figure II.3: Extrapolated pCO$_2$ maps (top) in March 1998 and (bottom) in October 1998

In March 1998, low pCO$_2$ regions (less than 330 µatm) occur south of Tasmania, south and east of New Zealand (**Figure II.3**). These areas are associated with chlorophyll-rich region. In the whole study area, we find a north-south pCO$_2$ gradient due to the inverse relationship between SST and pCO$_2$: in the northern part, pCO$_2$ is about 330 µatm (northeast) to 340 µatm (northwest), while in the southern part, pCO$_2$ is about 350 µatm (southwest) to 355 µatm (extreme southeast). Thus spatial pCO$_2$ variation is about 10-25 µatm from north to south and less than 10µatm from east to west. In October 1998, pCO$_2$ values are higher than in March due to lower biological activity and to higher SST. Again, low pCO$_2$ regions occur south and east of New Zealand, but the low pCO$_2$ region south of Tasmania is not apparent. Zone A is smaller than in March, because of lower biological activity. In the northern part, pCO$_2$ is relatively homogeneous (about 345 µatm) except in the chlorophyll-rich zone south and east of New-Zealand. The pCO$_2$ values increase from north to south and is more or less homogeneous in the southern part.

Budget of air-sea CO₂ fluxes

Monthly 1°×1° maps of atmospheric pCO_2 (pCO_2a) were constructed from atmospheric concentration of CO_2 in dry air (atmospheric xCO_2) provided by Globalview –CO₂ (http://www.cmdl.noaa.gov/ccgg/globalview/co2/index.html) at Cape Grim station in Tasmania, taking into account ECMWF atmospheric pressure and saturated water pressure. ΔpCO_2 fields were computed as the difference between pCO_2a and pCO_2 maps. Monthly 1°×1° net air-sea CO_2 flux maps result from the product of monthly exchange coefficients (K) and monthly ΔpCO_2 grids at 1°×1° resolution. K was derived from SST, ERS-2 wind products delivered by the Centre ERS d'archivage et de Traitement (CERSAT) of the Institut Français de Recherche pour l'Exploitation de la Mer (IFREMER), and the gas transfer velocity parameterization given by *Wanninkhof* (1992).
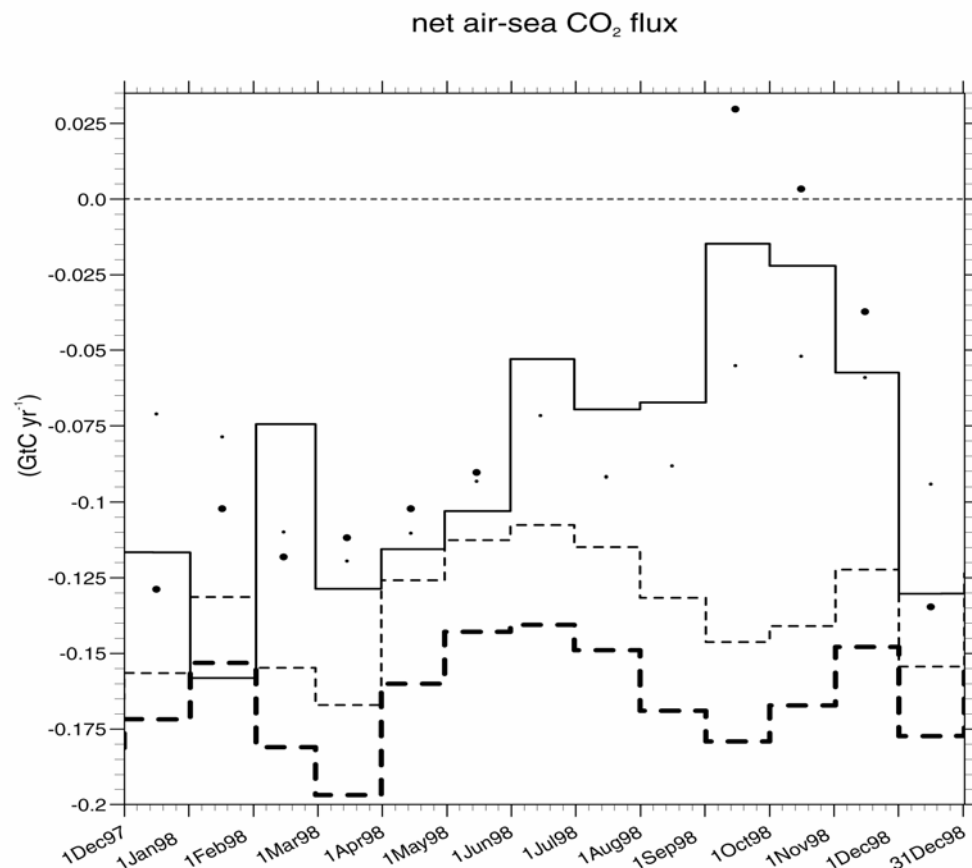
Figure II.4: Extrapolated net air-sea CO_2 flux deduced from the exchange coefficient computed from ERS-2 wind fields and the gas transfer velocity parameterization of *Wanninkhof* (1992) and reconstructed pCO_2 fields, and *Takahashi et al.* (2002) climatological mean ΔpCO_2 fields with correction for the atmospheric trend between 1995 and 1998 (dashed line).

Integrating CO_2 fluxes over the year shows that the studied area acts as a sink for atmospheric CO_2 amounting to 0.08 PgC yr^{-1} (**Figure II.4**). This value represents only half of the integrated fluxes derived by *Takahashi et al.* (2002). When comparing our calculated seasonal CO_2 fluxes with the *Takahashi et al.* (2002) climatology, we note that in summer and fall, fluxes obtained with both approaches are close. For spring and winter the difference is more substantial, but which of the two approaches provides a poor result can not be verified at present since few, if any, in situ measurements are available for these seasons. These differences depend on the extrapolation methods used to reconstruct pCO_2 fields. This emphasises the need for in situ measurements during these poorly covered seasons.

II.1.2. Spring and summer air-CO$_2$ fluxes in the Indian sector of the Southern Ocean

Based on underway pCO_2 measurements in the Indian sector of the Southern Ocean, carried out in the framework of BELCANTO (Figure II.5 and Table II.1), we budgeted spring and summer air-sea CO_2 fluxes using SST, SeaWIFS chlorophyll-a concentrations (Chl) and wind speed inferred from satellite measurements. We focused on the Indian sector (20°E-150°E; 30°S-60°S) from October 1997 to December 1999. Zonal variability of CO_2 flux was investigated by partitioning the data according to the main oceanographic provinces of the Southern Ocean, namely the subtropical zone (STZ), both north and south subantarctic zone (denoted as NSAZ and SSAZ respectively), polar frontal zone (PFZ) and polar open ocean zone (POOZ), using the positions of fronts inferred from a previous study conducted in the framework of BELCANTO and also based on satellite data (*Kostianoy et al., 2003, Kostianoy et al., 2004).*

Table II.1: Cruises for pCO_2 measurements carried out in the Indian Sector of the Southern Ocean in the framework of BELCANTO projects.

ship	area	period
R.S.V. Aurora Australis	South of Tasmania - SR3 transect	28-02 to 31-03-1998
R.S.V. Marion Dufresne	Crozet Basin	12-11 to 19-11-1998
R.V. La curieuse	Kerguelen Plateau	02-12 to 5-12-1998
R.S.V. Marion Dufresne	Crozet Basin	21-12 to 29-12-1999
R.S.V. Marion Dufresne	Crozet Basin	06-01 to 20-02-1999
S.V. Astrolabe	South of Tasmania - Adélie Land	22-10 to 28-10-1999
S.V. Astrolabe	South of Tasmania - Adélie Land	21-12 to 27-12-1999
R.S.V. Aurora Australis	South of Tasmania - Eastern Antarctica	31-10 to 12-12-2003
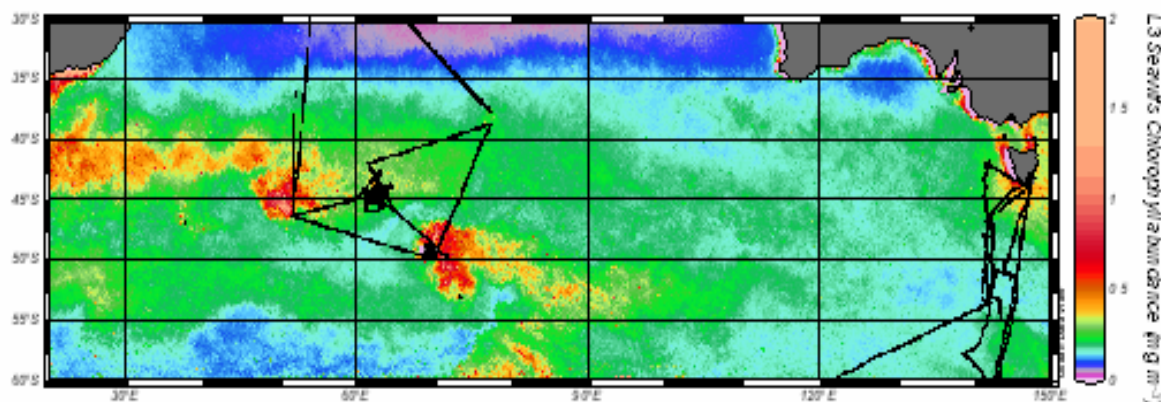
Figure II.5: Underway pCO_2 data for the Indian sector of the Southern Ocean (carried out in the framework of BELCANTO) superimposed on SeaWIFS chlorophyll concentrations (average maps used for the pCO_2 reconstruction, e.g. spring and summer seasons from October 1997 to December 1999).

Correlation of oceanic pCO_2 with chlorophyll and SST

A complete description of the experimental set-up of underway pCO_2 measurements was given by *Frankignoulle et al.* (2001). Surface pCO_2 measurements were corrected to a single reference year (arbitrary chosen as 1999) using atmospheric CO_2 concentration measured at Cape Grim station (provided by Globalview –CO_2 http://www.cmdl.noaa.gov/ccgg/globalview/co2/index.html). We collocated corrected pCO_2 measurements with weekly standard maps (resolution of 9×9 km) of Level 3 SeaWIFS Chl (obtained from the National Atmosphere and Space Agency http://oceancolor.gsfc.nasa.gov/). SST was derived from Advanced Very High Resolution Radiometer (AVHRR) data (obtained from the Physical Oceanography Distributed Active Archive Center). Covariation of corrected pCO_2 for spring and summer season with Chl and in situ SST was investigated using Surfer® package ("kriging" method - type "block") (**Figure II.6**). Wind speed was derived form ERS-2 wind products delivered by the Centre ERS d'archivage et de Traitement (CERSAT) of the Institut Français de Recherche pour l'Exploitation de la Mer (IFREMER).

Reconstruction of CO$_2$ flux fields

The pCO$_2$ fields were reconstructed using the same rationale as or the study conducted south of Tasmania and New Zealand (see section II.1).
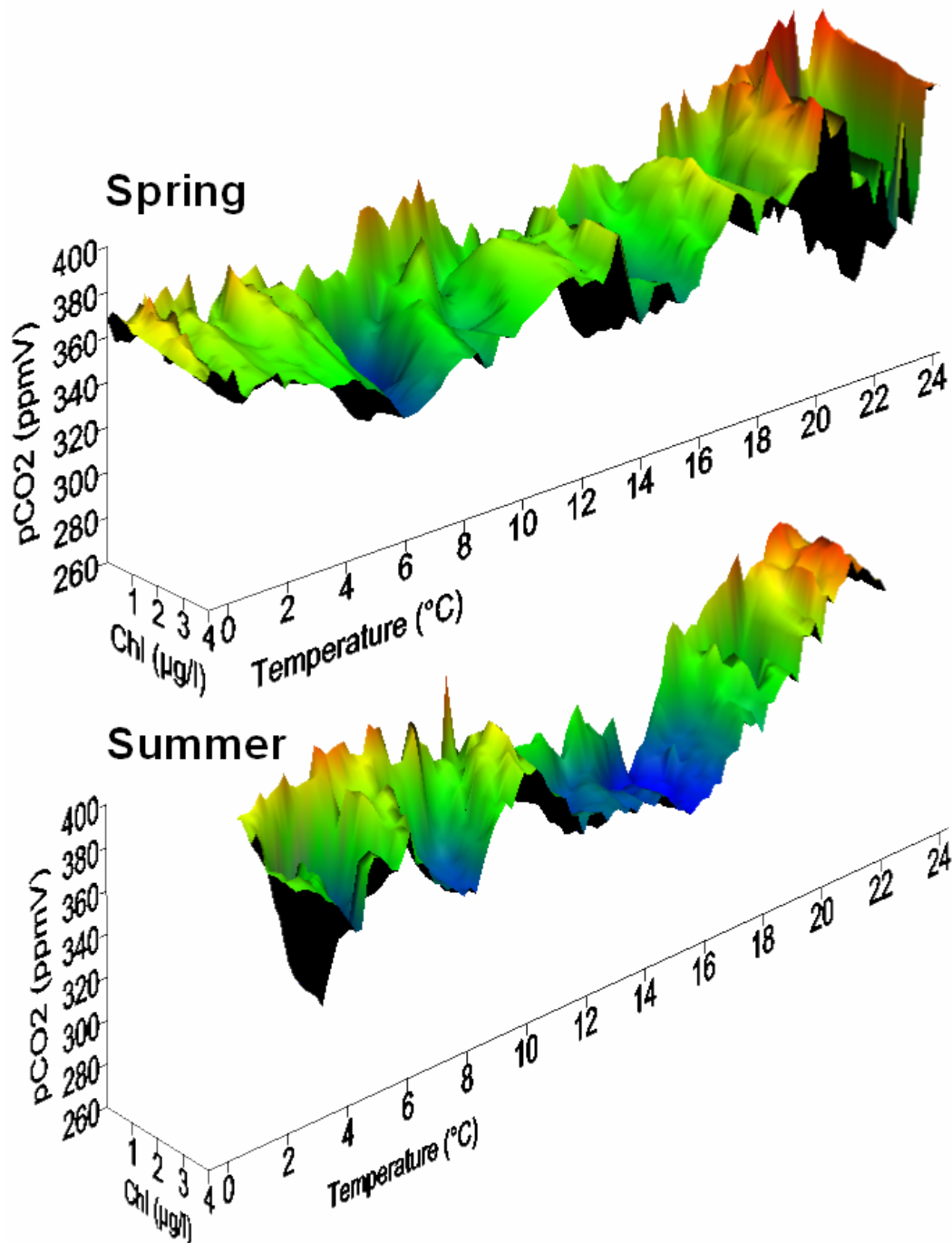
Figure II.6: Cross correlations between pCO$_2$, SST and Level3 SeaWIFS chlorophyll-a concentration (Chl) in spring (top) and summer (bottom) in the Indian sector of the Southern ocean used for the reconstruction of pCO$_2$ fields.

We used fits between pCO_2, SST and SeaWIFS Chlorophyll shown in **Figure II.6** to reconstruct pCO_2 fields over the Indian sector for the period between October 1997 to December 1999. This time period is covered by SeaWIFS data, our analysis of the positions of fronts and most of the in situ pCO_2 measurements. We reconstructed monthly pCO_2 fields with a resolution of 0.2°×0.2° using monthly SeaWIFS and SST maps. SST maps were derived from AVHRR data obtained from the PODAAC. We subsequently computed CO_2 fluxes based on the gas transfer velocity parameterization of *Liss and Merlivat* (1986), *Wanninkhof* (1992) and *Wanninkhof and McGillis* (1999) using wind speed derived form ERS-2 wind products delivered by the CERSAT.

In spring a strong sink for atmospheric CO_2 is centred on the Crozet Basin (Figure II.7). This is likely due to the intense frontal dynamics specific to this region which promotes large decreases of pCO_2 (*Fiala et al., 2003*). In summer, the sink of atmospheric CO_2 spreads over the entire SSAZ and PFZ. The frontal signature appears well marked on the distribution of CO_2 fluxes in SSTF, SAF and PF. On the whole, the most intense sink of atmospheric CO_2 occurs in the SSAZ.

Budget of air-sea CO_2 fluxes

While budgeting CO_2 fluxes from reconstructed CO_2 fluxes fields, attention was paid to discriminate the different oceanographic provinces of the Southern Ocean delimited by the fronts. Analysis of the positions of these fronts was carried out mainly using SST gradients derived from remote sensing AVHRR data in conjunction with previous work based on XBT and CTD vertical profiles (*Kostianoy et al., 2003*). Monthly maps of the main frontal structures were established over the whole Indian sector of the Southern Ocean from 1997 to 1999. These maps allowed to budget the CO_2 flux per province using different parameterizations of the gas transfer velocity (**Table II.2**).

The overall sink of atmospheric CO_2 for the 35°S-50°S band of the Indian sector of the Southern Ocean ranges between -0.039 and -0.110 PgC in spring and between -0.032 and -0.093 PgC in summer (**Table II.2**). As expected, large changes in the magnitude of the sink appear depending on the choice of the gas transfer velocity parameterization. *Metzl et al.* (1995) report summer CO_2 fluxes (January 1991 to March 1993) ranging between -2.5 and -5.5 mmol m^{-2} d^{-1}, with an average value around -3.5 mmol m^{-2} d^{-1} for the area corresponding with the one studied here. In a subsequent paper, *Metzl et al.* (1999) report average fluxes for the same area of about -5.1 mmol m^{-2} d^{-1} in spring and -11.3 mmol m^{-2} d^{-1} in summer, between 1992 to 1995. Such fluxes, computed with the gas transfer velocity parameterization of *Liss and Merlivat* (1986), are higher that our present estimations. Our computed flux

values for the Indian and the western Pacific sectors of the Southern Ocean are lower than previous ΔpCO_2-based estimates *(Metzl et al. 1995, Metzl et al. 1999, Takahashi et al. 2002)*. This might support the conclusions of inverse models suggesting that previous ΔpCO_2 based studies overestimate CO_2 fluxes in the Southern Ocean (*Gloor et al., 2003, Gurney et al., 2004, Jacobson et al., 2005*). However, the estimates of *Metzl et al.* (1995,1999) and *Takahashi et al.* (2002) were mostly based on older data than used in the present caluclations. Hence, these differences might also be ascribed to a large inter-annual variability of the magnitude of the fluxes of CO_2 in the Southern Ocean as also recently observed for the period between 1998 to 2002 (*Nicolas Metzl*, personal communication).
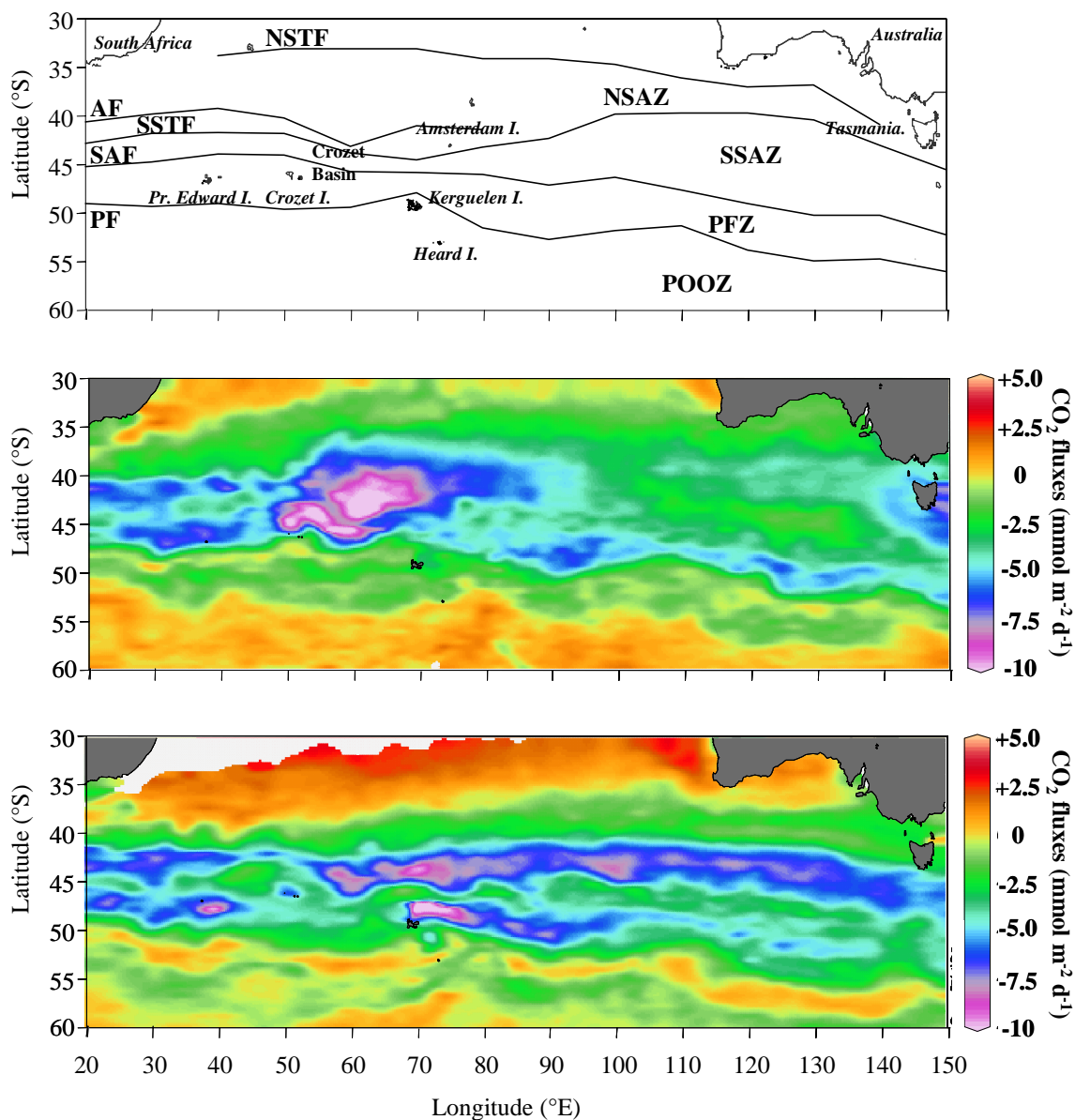
Figure II.7: Mean positions of the fronts inferred from SST gradients (top) and reconstructed air-sea CO_2 fluxes in spring (middle) and summer (bottom) based on the *Wanninkhof* (1992) gas transfer velocity parameterization.

Table II.2: Averaged and integrated air-sea CO_2 fluxes over the different provinces of the Indian sector of the Southern Ocean. Fluxes were computed using the gas transfer velocity parameterizations of *Liss and Merlivat* (1986), *Wanninkhof* (1992) and *Wanninkhof and McGillis* (1999). Integrated fluxes represent a 3 months period.

Average flux (mmol m^{-2} d^{-1})	Liss et Merlivat (1986) Spring	Summer	Wanninkhof (1992) Spring	Summer	Wanninkhof and McGillis (1999) Spring	Summer	Nightingale et al. (2000) Spring	Summer
STZ	-0.72	0.48	-1.37	0.94	-1.43	0.84	-0.94	0.67
NSAZ	-2.02	-0.73	-4.01	-1.43	-5.11	-1.77	-2.69	-0.96
SSAZ	-1.96	-2.52	-4.04	-5.15	-5.85	-7.35	-2.67	-3.40
PFZ	-1.52	-2.01	-3.29	-4.36	-5.42	-7.24	-2.13	-2.83
POOZ	-0.10	-0.39	-0.22	-0.82	-0.43	-1.32	-0.14	-0.54
35°~50°S	-1.97	-1.66	-4.00	-3.39	-5.59	-4.87	-2.66	-2.24
Integrated flux (PgC)								
NSAZ	-0.018	-0.006	-0.036	-0.012	-0.046	-0.015	-0.024	-0.008
SSAZ	-0.012	-0.016	-0.025	-0.032	-0.036	-0.045	-0.016	-0.021
PFZ	-0.008	-0.011	-0.017	-0.023	-0.029	-0.038	-0.011	-0.015
35°~50°S	-0.039	-0.032	-0.080	-0.065	-0.110	-0.093	-0.053	-0.043

II.1.3. Contribution of CO_2 fluxes over sea ice

At maximum extent seasonal sea ice represents about 7% of the Earth surface, representing one of the largest biomes on Earth (*Lizotte*, 2001). For decades, sea ice was seen as an impermeable and inert barrier for air-sea exchanges of CO_2, and as a result global climate models do not include CO_2 exchanges over this compartment (*Tison et al. 2002*). This is because budgets of CO_2 and oxygen of Weddell Sea waters do not reveal evidence of air-sea exchange of CO_2 for Winter Surface Water at the time it subducts and mixes with other water masses to form Weddell Sea Bottom Water (*Weiss et al.* 1979, *Poisson and Chen* 1987), a major contributor to Antarctic Bottom Water formation. However, *Gosink et al.* (1976) studying permeation constants of SF_6 and CO_2 within sea ice, stressed that sea ice is a highly permeable medium for gases. They also suggested that gas migration through sea ice could be an important factor in winter ocean-atmosphere exchange when the sea ice surface temperature is >10°C. More recently, *Semiletov et al.* (2004) found evidence for CO_2 uptake over sea ice edge in the Arctic. In order to reconcile these contradictory conclusions, one must bear in mind that there is no evidence of CO_2 exchange during winter between surface water beneath sea ice and the atmosphere. In autumn and winter, when this water sinks sea ice is growing and

due to its low temperatures, it is likely impermeable to gas exchange. However, it is reasonable to think that when sea ice is warming up, melting and becoming permeable, air-ice gas exchanges are possible.

Such spring and summer gas exchanges are unlikely to affect the chemical signatures of deep-water, since deep-water formation is weak at this time of the year and their signature in well stratified spring surface waters will be altered by summer processes prior to winter surface and deep water formation.
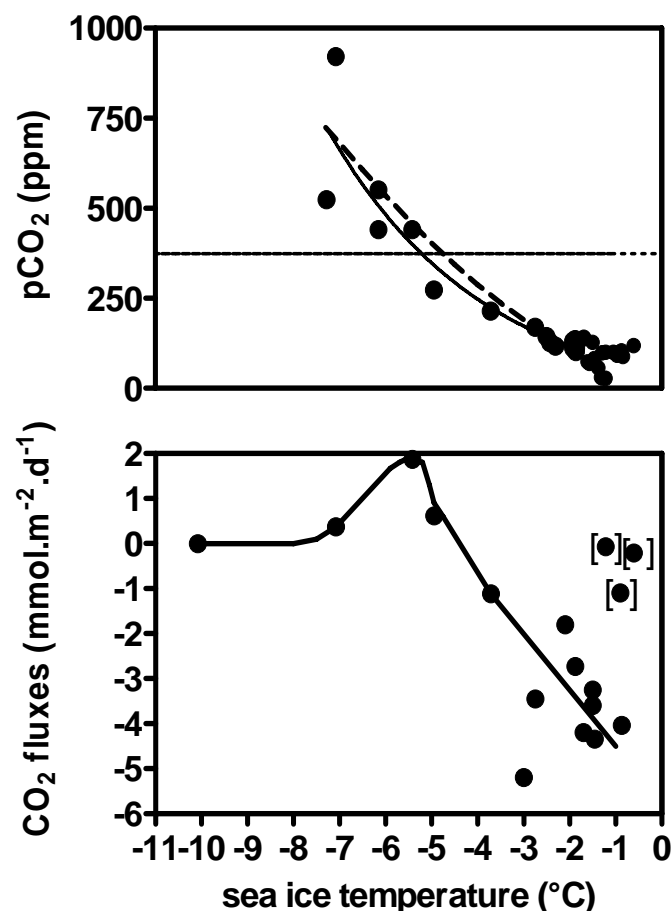
Figure II.8: pCO_2 within brines and related air-sea ice CO_2 fluxes versus sea ice temperature integrated over the depth of sackholes. Data within brackets were obtained during superimposed ice events. Solid and horizontal dotted lines denote, respectively, the mean trend and the atmospheric $pCO_{2(air)}$. Dashed line corresponds to the theoretical variations of pCO_2 $_{(water)}$ due to the increase of temperature the decrease of salinity. Salinity decrease (dilution by meltwater) was estimated from temperature using a relationship taken from *Cox and Weeks* (1985) while the thermodynamical effect of salinity and temperature changes on pCO_2 were estimated using the CO_2 dissociation constants of *Mehrbach et al.* (1973) refitted by *Dickson and Millero* (1987).

Dissolved inorganic carbon dynamics within sea ice and associated air-sea ice fluxes were studied during the 2003/V1 cruise of the R.V. Aurora Australis in first year Antarctic pack ice in the Indian sector of the Southern Ocean and during the "ISPOL" drifting station experiment aboard R.V. Polarstern in first year and multiyear pack ice in the Weddell Sea. The backbone of our study was the direct measurement of pCO_2 in brines using conventional pCO_2 equilibration techniques. This portable device also allowed to measure air-ice CO_2 fluxes using the chamber method.

In spring, as sea ice is warming up, pCO_2 of brines decreases dramatically from a large over- saturation (ΔpCO_2 = $pCO_{2(water)}$ – $pCO_{2(air)}$ = 525ppm) to an extreme under-saturation (ΔpCO_2 = -335 ppm). A large part of this decrease is driven by the dilution of brines with melted ice crystals counteracting the thermodynamic effect of temperature increase **(Figure II.8).** Other processes appear to enhance this CO_2 uptake, namely primary production and dissolution of calcium carbonate ($CaCO_3$). Antarctic pack ice hosts algal communities whose biomass and photosynthesis rate can exceed 50 mg m^{-3} and 8 mg C mg^{-1}Chl-a h^{-1}, respectively (see *Arrigo* 2003). Primary production peaks in January and is likely to decrease pCO_2 significantly in late spring and summer. Precipitation of $CaCO_3$ in sea ice as a result of drastic increase of salinity in brines is subject to a long-lived debate. Numerous laboratory experiments show that precipitation of $CaCO_3$ occurs during sea ice formation (*Jones et al.* 1983, *Tison et al.* 2002, *Papadimitriou et al.* 2004) but to date this has not been verified in the field (*Anderson and Jones.E.P.* 1985, *Gleitz et al.* 1995). However, low values of normalized DIC and TA (DIC_{35} and TA_{35}, respectively) in brines collected in early spring in cold sea ice (**Figure II.9**) are a conspicuous indication that $CaCO_3$ precipitation had taken place within sea ice brines in the period preceding sampling. The impact of this precipitation is very marked, leading to a removal of 60% of DIC_{35} from brines. Precipitation of $CaCO_3$, when brine salinity increases dramatically due to sea ice growth, produces CO_2. In contrast, as sea ice is melting in spring, subsequent dissolution of $CaCO_3$ likely matches and enhances the decrease of pCO_2 due to the dilution with meltwater.

Fluxes of CO_2 at the air-ice interface were measured with the chamber method and ranged from +1.9 to –5.2 mmol m^{-2} d^{-1} (**Figure II.8**). Such values are lower than measured by eddy correlation over slush – a mixture of melting snow, ice and seawater covering sea ice - in the Antarctic pack ice (*Zemmelink et al.*, 2005) and sea ice melt ponds in fast ice of the North American-Siberian Arctic Ocean shelf zone (*Semiletov et al.*, 2004), for which reported values ranges between -6.6 and -18.2 mmol m^{-2} d^{-1} and -19.5 and -38.6 mmol m^{-2} d^{-1}, respectively. Although we cannot disregard the fact that some analytical artefacts or spatial heterogeneity are
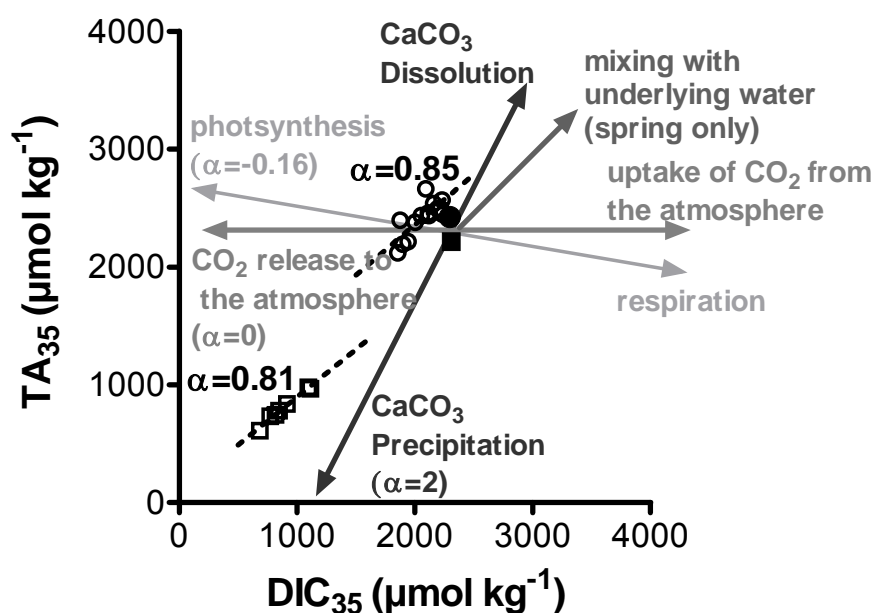
Figure II.9 : DIC and TA normalized at a salinity of 35. Open squares and open circles denote, respectively, spring and summer samples; slope of the corresponding regression lines is reported as "α". Full squares and circles denote mean values of the underlying water in spring and summer, respectively. Arrows represent the theoretical variation of DIC_{35} and TA_{35} according to specific biogeochemical processes.

responsible of these differences, we surmise that the explanation lays in the occurrence of surface communities at the atmospheric interface. We paid attention to measure CO_2 fluxes over most sea ice from which surface biological communities were absent, while reported eddy correlation measurements were carried out over slush and melting ponds, known to berth highly productive algae communities (*Legendre et al.*, 1992). These surface communities benefit from high light level and primary production is fuelled by nutriments from seawater flooding as snow loading or sea ice rafting depress the ice surface below the freeboard. Such surface flooding occurs over 15-30% of the ice pack in Antarctica (*Wadhams et al.*, 1987). These surface communities exhibit photosynthetic rates comparable to those of open ocean Antarctic phytoplankton (*Lizotte and Sullivan*, 1992) and might be responsible for the majority of sea surface productivity in Antarctic Sea Ice (*Legendre et al.*, 1992). These communities confined at the surface can easily exchange CO_2 with the atmosphere through the porous snow cover and this rapid exchange could be responsible for the diel cycle of CO_2 fluxes sometimes observed over arctic pack ice (*Lisa Miller, Institute of Ocean Sciences (CA), pers. Commun.*). This emphasizes that surface communities may enhance significantly the uptake of CO_2.

In a highly heterogeneous environment such as sea ice, the inherent small space scale resolution of chamber CO_2 flux measurements allows to

comprehensively compare measured fluxes with pCO_2 within the ice. CO_2 fluxes appear to be consistent with the status of brine CO_2 saturation, with the exception of the transition around -5°C. The pCO_2 gradient between the atmosphere and the brines of the top layer of sea ice is the main driver of CO_2 fluxes. However, the magnitude of these fluxes is modulated by several factors and in particular by the sea ice temperature and snow structure. Despite the occurrence of high pCO_2 values in ice around -7°C the CO_2 fluxes were weak, due to a permeability decrease of the ice. Below -10°C no CO_2 flux was detected at all indicating efficient impermeability of the sea ice. While snow allows a rapid exchange of gases with the atmosphere *(Massman et al.,* 1997, *Albert et al.*, 2002, *Takagi et al.*, 2005), no CO_2 flux was detected once lenses of ice formed above the sea ice. Such superimposed ice forms after a severe snow melting event, when percolating freshwater refreezes when contacting of sea ice. Superimposed ice, as is freshwater ice, is impermeable to gas transport (*Albert and Perron*, 2000). The formation of superimposed ice at the top of sea ice and subsequent inhibition of air-ice CO_2 flux leads to a drastic decrease of pCO_2 down to 30 ppm. This highlights the role of CO_2 invasion from the atmosphere that balances the CO_2 removal from primary production in summer, and maintains sea ice pCO_2 above 200 ppm.

Budget of air-sea ice CO$_2$ fluxes

In order to assess the possible significance of CO_2 flux over sea ice, we attempted a first scaling of CO_2 fluxes over Antarctic sea ice in spring and summer. As discussed
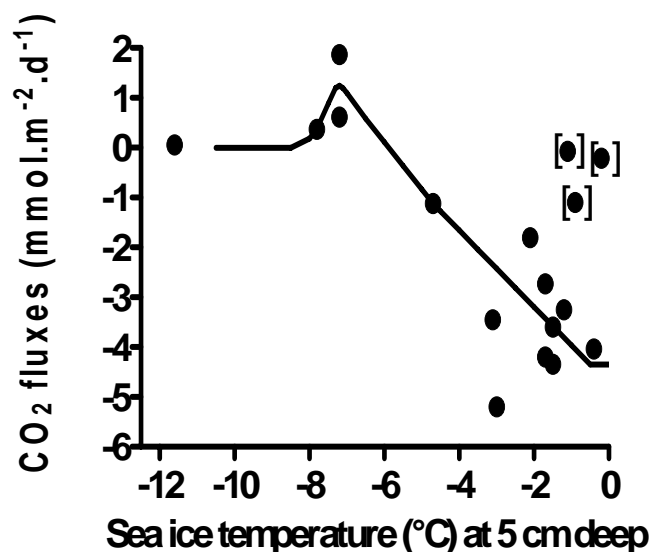
Figure II.10: Air-sea ice CO_2 fluxes versus sea ice temperature at 5 cm depth. Data within brackets correspond to superimposed ice events. Solid curve represents the relationship (flux$_{CO2}$) which relates air-sea ice CO_2 fluxes to sea ice surface temperature.

above, sea ice temperature exerts a strong control on both sea ice pCO_2 and permeability and ultimately on CO_2 transfer at the air-ice interface (**Figure II.10**). The relationship between CO_2 flux and sea ice temperature allows reconstructing CO_2-flux fields using sea ice temperature and concentration data derived from ASMR-E L3 data (Advanced Microwave Scanning Radiometer – Earth Observing System, available at http://nsidc.org/data/amsre/). ASMR-E L3 data provide sea ice concentration and temperature at the air-ice interface with a resolution of 25 km * 25 km at a daily frequency (*Cavalieri et al.* 2005).

We derived a relationship, denoted $flux_{CO_2}$, between CO_2 flux over both first year and multiyear ice against sea ice temperature at 5cm depth (**Figure II.10**). We then reconstructed fields of weekly CO_2 flux for September to January which corresponds to the time period covered by in situ measurements taking into account both AMSR-E sea ice temperature and sea ice concentration:

$$F_{CO_2} = flux_{CO_2}(T_{ice}) \times C_{ice} \times A_{node}$$

where F_{CO_2}, T_{ice}, C_{ice} and A_{node} denote the CO_2 fluxes over a week, AMSR-E L3 temperature and concentration of sea ice and grid node area, respectively.

The budget of CO_2 fluxes takes only into account those regions with >65% sea ice extent, corresponding to the range of sea ice extentions encountered during the
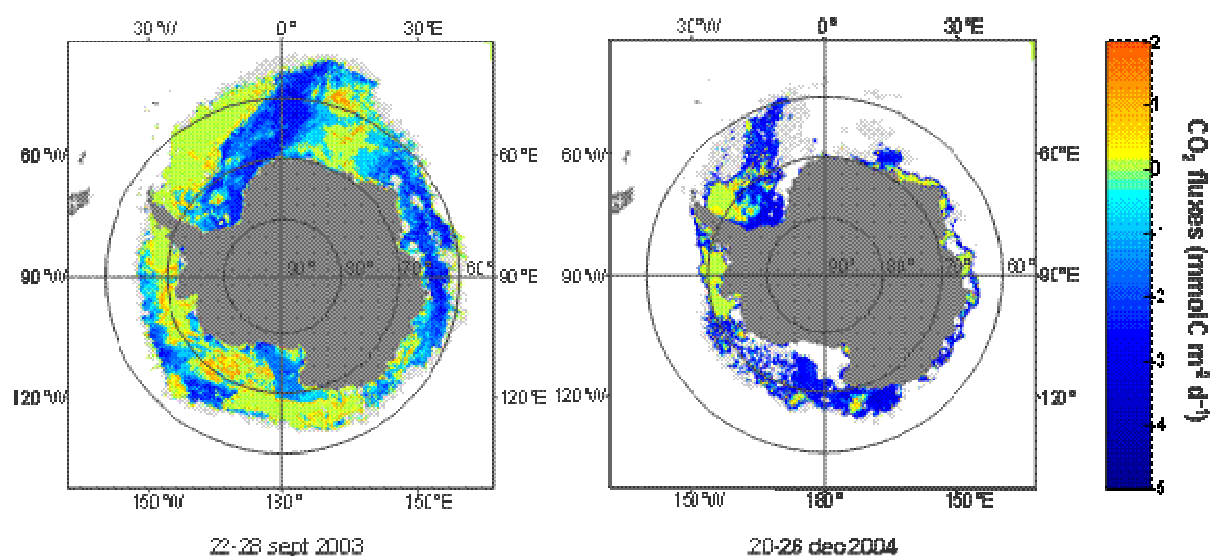
Figure II.11: Reconstructed air-sea ice CO_2 fluxes over Antarctic sea ice in spring 2003 and summer 2004. Light grey areas correspond to regions with sea ice concentration lower than 65%.

cruise. We reconstructed and budgeted air-ice CO_2 flux fields in spring and summer (**Figure II.11**) for the period from 2002 - 2005 (**Table II.3**). Compact Antarctic sea ice (ice concentration >65%) acts as a sink for atmospheric CO_2 from September to January with values ranging from 0.015 to 0.024 PgC. This represents 6% to 9% of the uptake of the Southern Ocean south of 50°S if we consider that current assessments of the oceanic uptake of CO_2 south of 50°S converge towards 0.26 pgC yr^{-1} (*Matear and Hirst,* 1999, *Takahashi et al.,* 2002, *Roy et al.,* 2003, *Takahashi* 2003, *Nicolas Metzl, LOCEAN (FR), pers. commun.*). Spring and summer CO_2 uptake by Antarctic sea ice is therefore significant. We stress that this tentative estimate is a conservative one, since surface phytoplankton communities, when present, will significantly enhance CO_2 uptake and this impact is not accounted for in the present budget.

Table II.3: Air-sea ice CO_2 fluxes over Antarctic sea ice in spring and summer for regions with sea ice concentrations above 65%.

	CO_2 flux (PgC)
Sep 2002 – Jan 2003	-0.015
Sep 2003 – Jan 2004	-0.017
Sep 2004 – Jan 2005	-0.024
Average	-0.018

II.2. Potential export from New Production

Regional variation of spring new production: Clivar SR3 cruise

The study of nitrogen cycling in the surface ocean provides helpful information to better understand the primary production and its export flux. Indeed, the determination of nitrogen uptake enables the separation of new from regenerated production — i.e. of primary production sustained by nitrate and N_2 from that sustained by regenerated N-nutrients (*Dugdale and Goering,* 1967)) — and the estimation of "export" production via the use of f-ratio (*Eppley and Peterson*, 1979). Although the concept of new production as a proxy of export production has been questioned and revised (*Bronk et al.,* 1994), new production and f-ratio remain useful tools to characterize ecosystem functioning. Yet, new production should be considered as "exportable production" rather than "export production" (e.g. *Sambrotto*

and Mace, 2000). We report here new production estimates for surface waters of the Southern Ocean during the austral spring 2001.

Nitrate, ammonium and urea uptake rates as well as new production were studied during the CLIVAR SR3 cruise (**Figure I.8** and **Table I.1** see **section I.3.2**). Seven stations were visited when cruising southward; stations at 63.9°, 60.9° and 51.0°S were re-visited during the return transect after a delay of 11, 17 and 31 days, respectively. Fronts and zones of the Southern Ocean and their acronyms are indicated in **Figure I.8**. Seawater was sampled using Niskin bottles at four depths from 5m down to 70m or 100m.

Uptake rates were estimated from incubations using ^{15}N and ^{13}C as tracers of N and C uptake. Details concerning the methodology can be found in *Savoye et al.* (2004a). *f*-ratio and new production were calculated as follows:

$$f\text{-ratio = nitrate uptake / N-uptake} \qquad \text{eq. 4}$$

where N-uptake is the sum of nitrate, ammonium and urea uptake rates.

$$\text{New production (mmol C m}^{-2}\text{d}^{-1}\text{) = carbon uptake x }f\text{-ratio} \qquad \text{eq. 5}$$

Uptake rates and new production were integrated over the upper 70m of the water column (**Figure II.12**). On the basis of N-uptake conditions and new production, three regions are distinguished:

(1) The Subantarctic Zone (SAZ) and the Subantarctic Front (SAF), in the north of the study area (48.8–51.0°S), are characterized by low N-uptake rate (4.4 ± 0.3 mmol m^{-2} d^{-1}), low new production (6.2 ± 1.8 mmol C m^{-2} d^{-1}) and by dominance of small phytoplankton cells (*Savoye et al.,* 2004a; *Kopczynska et al.,* subm.) over a time scale of one month. The N-uptake conditions of this region are versatile since there was a shift from a system dominated by regenerated production (*f*-ratio = 0.38 ± 0.05) to a system dominated by new production (*f*-ratio = 0.82) within one month. During the second visit of the SAF, surface water was more influenced by northern water (higher water temperature and salinity). SAZ waters were higher in iron concentration (*Sedwick et al.,* 2002) and perhaps this may explain the observed increase in *f*-ratio (cf *Armstrong,* 1999), although the lack of iron measurements during the second visit precludes a clear examination of this possibility.

(2) The polar Fronta Zone (PFZ) and the Inter Polar Front Zone (IPFZ), in the central part of the study area (53.7–56.9°S), are characterized by slightly higher N-uptake rates (5.6 ± 0.1 mmol m^{-2} d^{-1}), low new production (5.9 ± 2.5 mmol C m^{-2} d^{-1}) and dominance of small phytoplankton (*Savoye et al.,* 2004a; *Kopczynska et al.,* subm.). N-uptake is slightly dominated by nitrate uptake (*f*-ratio = 0.56 ± 0.01).

However, as this area was not re-visited, temporal variability of the production conditions could not be assessed.

(3) AZ-S and SIZ (60.9–64.9°S) are characterized by high *f*-ratio (0.61 ± 0.08). Large phytoplankton (*Savoye et* al., 2004a; *Kopczynska et al.,* in prep.) dominated the community. N-uptake and new production are the highest along the transect but appear variable at relatively short time scale since the N-uptake decreased from 11.0 ± 1.7 to 7.6 ± 0.8 mmol m^{-2} d^{-1} and the new production from 19.8 ± 3.9 to 10.5 ± 3.2 mmol C m^{-2} d^{-1} within about two weeks.
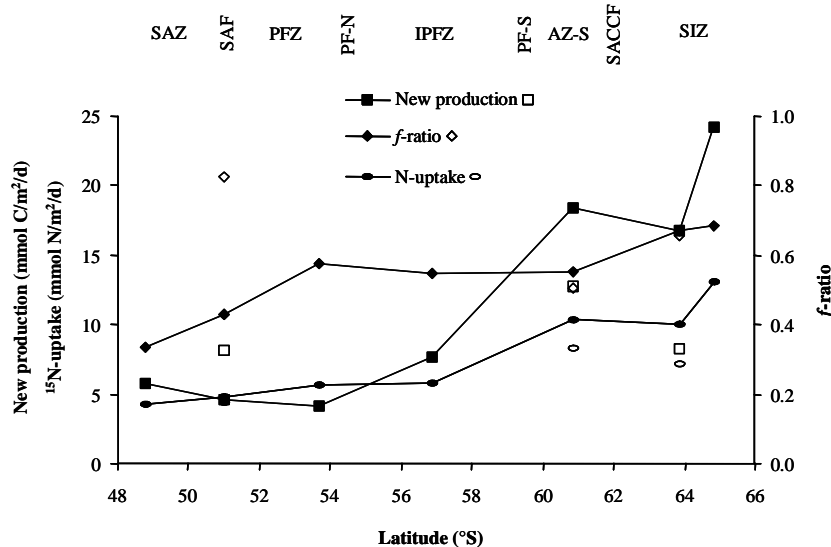
Figure II.12: Integrated nitrogen uptake rates *f*-ratio, and new production. Closed and open symbols correspond to first and second visits, respectively. SAZ, SAF, PFZ, PF-N, IPFZ, PF-S, AZ-S, SACCF and SIZ as indicated in Figure I.8.

The latitudinal pattern of N-uptake conditions during spring fits with the nitrogen regime in nitrate excess (in the North) and silicate excess (in the South) areas as reported by *Goeyens et al.* (1998): low new production in the North and pulsed system in the South. The latitudinal trend of new production is similar to the [234]Th fluxes measured during the same cruise (*Savoye et al.,* 2004b; see section II.3) and is in agreement with C fluxes from sediment trap records covering the SAZ and PFZ growth season of 1997-1998 (*Trull et al.,* 2001b). It appears that AZ-S and SIZ constitute the region of highest exportable production while lowest is observed for the PFZ. This is consistent with previous results of *Trull et al.* (2001b) and *Elskens et al.* (2002) for the northern part of this same transect (140°E), and of *Sambrotto and Mace* (2000) along 170°W. However, for the Inter-Polar Frontal Zone (IPFZ) there is a strong contrast between the 140°E (present study) and 170°W (*Sambrotto and*

Mace, 2000) transects. New production in the IPFZ at 140°E is low and close to values observed more northward whereas at 170°W new production is high and close to values observed more southward. This may be due to the physics: the Polar Front at 140°E divides into two branches 4-5° apart from each other whereas the Polar Front at 170°W is much narrower (1.5°).

The present N-uptake and new production results are in the lower range of the literature data for spring and are only slightly higher than summer values reported for the same 140°E transect (*Elskens et al.,* 2002).

When excluding the results for the SAF station (second visit, see above), which is an outlier, *f*-ratio appears strongly correlated with sea surface temperature (R^2=0.83, $p<0.01$) as well as with integrated nitrate concentration (R^2=0.80, $p<0.01$). Temperature and integrated nitrate concentration were also strongly correlated (R^2=0.95, $p<0.01$; all data). Such a relationship between *f*-ratio and temperature has been proposed by *Laws et al.* (2000) on the basis of a simple ecosystem model emphasizing differential responses of autotrophs and heterotrophs to temperature. However there are many other possible reasons for its occurrence, including variations in phytoplankton community responses alone, correlations of mixed layer depths and thus light levels with temperature, .. .

II.3- Measured export from the upper mixed layer under natural and Fe-amended conditions

The radioisotope ^{234}Th is produced from ^{238}U decay. Because of the short half-life of ^{234}Th (24.1d) and its strong affinity for particles, its deficit with respect to ^{238}U has been used as a powerful tool to study biogenic particle export from the surface ocean (*Coale and Bruland,* 1985). Here we report two studies of ^{234}Th / ^{238}U disequilibria performed in the upper mixed layer of the Southern Ocean: (1) WOCE SR3 transect (CLIVAR-SR3 cruise; Australian sector, 30 October – 14 December 2001) and (2) the European Iron Fertilization Experiment (EIFEX cruise; Atlantic sector; 20 January – 25 March 2004).

Clivar SR3 cruise: export under natural Fe condition in different zones of the Southern Ocean

Details regarding this cruise and its scientific strategy can be found in section II.2, while details regarding the methods can be found in *Savoye et al.* (2004b) and *Pike et al.* (2005). Briefly, ^{230}Th was added as a yield monitor to a 4L-seawater sample. After equilibration, Mn precipitate was formed by addition of $KMnO_4$ and $MnCl_2$ to scavenge Th and filtered on quartz fiber filter. Beta radioactivity was

measured on board generally over a 12-24 hour counting period using low level beta counters (Risø, Denmark). Filters were re-counted after 6 months for beta background, after which ^{230}Th was analyzed by ICP-MS and Th yield calculated. Average Th recovery was 91%. The final relative uncertainty on total decay corrected ^{234}Th activity was 2%. ^{238}U activity was calculated from salinity following *Chen et al.* (1986). Total accuracy of the method was evaluated by comparison to deep water samples where ^{234}Th activity = ^{238}U activity.

A deficit of ^{234}Th relative to ^{238}U was found in the mixed layer all along the SR3 transect (**Figure II.13**), indicating export of particles at all stations. ^{234}Th reached secular equilibrium with ^{238}U at the base or just below the mixed layer. ^{234}Th fluxes were calculated at 100m using steady state and non-steady state models (*Buesseler et al.,* 1992; *Savoye et al.,* accepted) depending on whether stations were visited only once or twice, respectively. We assume in these models that supply and loss of ^{234}Th via horizontal and vertical mixing are small, compared to the rates of ^{234}Th production from ^{238}U, ^{234}Th decay, and ^{234}Th loss on sinking particles. Physical processes have only been found to impact ^{234}Th activity balances significantly only in sites of intense upwelling or in coastal regions where tidal pumping and activity gradients are a larger component of the ^{234}Th activity balance (*Buesseler,* 1998). Uncertainty on fluxes is 50 dpm m^{-2} d^{-1}.
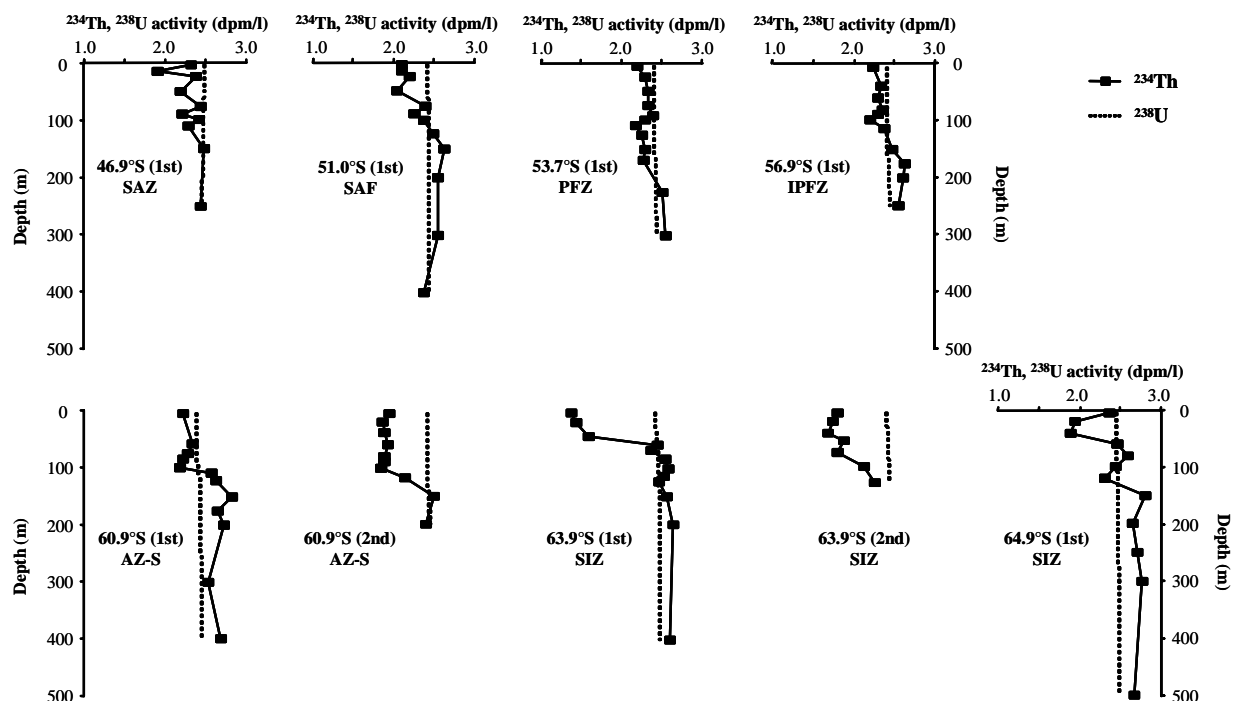
Figure II.13: ^{234}Th and ^{238}U activity profiles for the first (1st) and second (2nd) visits of stations during the Clivar SR3 cruise in the Australian sector of the Southern Ocean (spring 2001). SAZ: Sub-Antarctic Zone; SAF: Sub-Antarctic Front; PFZ: Polar Front Zone; IPFZ: Inter-Polar Front Zone; AZ-S: southern Antarctic Zone; SIZ: Seasonal Ice Zone.

During austral spring 2001, ^{234}Th fluxes were low in the north (ca. 630 dpm m^{-2} d^{-1}), minimal in the Polar and Inter Polar Front Zones (ca. 300 dpm m^{-2} d^{-1}) and high in the south (ca. 3000 dpm m^{-2} d^{-1}). The latter were similar to fluxes reported by *Buesseler et al.* (2001) at 170°W but much higher than fluxes reported by *Rutgers van der Loeff et al.* (1997) in the Atlantic sector for early spring conditions. In contrast, for SAZ and IPFZ, ^{234}Th fluxes were much smaller in our study than generally reported in the literature, being similar only with early spring values (*Rutgers van der Loeff et al.,* 1997).

^{234}Th export fluxes were converted into particulate organic carbon (POC) flux by multiplying them with the POC/^{234}Th ratio of large particles (55-210µm), assumed to represent the sinking particles. During the CLIVAR-SR3 cruise export production (i.e. the POC export flux) ranged from 20 mg C m^{-2} d^{-1} in the PFZ to 670 mg C m^{-2} d^{-1} in the SIZ at 64°S. Our results indicate low particle export in the SAZ and SAF, very low particle export in the PFZ and IPFZ and high export in the AZ-S and SIZ during spring 2001 (**Figure II.14**). This latitudinal trend is in quite good agreement with new production measured data from the same cruise (**Figure II.14**). The very low export production and new production in the PFZ and IPFZ contrast with the widely accepted idea that the Polar Front enhances primary and export production (e.g. *Usbeck et al.,* 2002). This could be specific to the Australian sector because of specific hydrodynamic conditions. For instance, in the Australian sector at 140°E the Polar Front divides into two branches 4-5° apart (*Trull et al.,* 2001). Elsewhere, the Polar Front branches are located closer to each other (*Pollard et al.,* 2002).
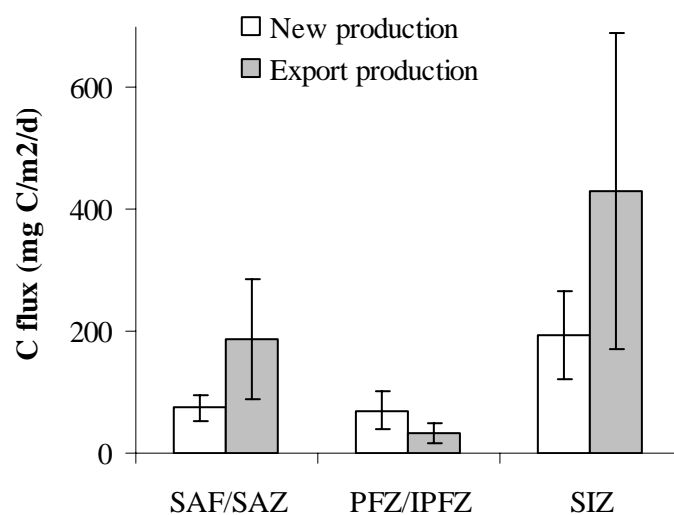
Figure II.14: Export production at 100 meter depth (grey bars) and new production integrated over the upper 70m (white bars) during the CLIVAR-SR3 cruise in the Australian sector of the Southern Ocean (spring 2001). Error bars correspond to standard deviation. SAZ, SAF, PFZ, IPFZ, SIZ as in Figure I.8.

The European Iron Fertilization Experiment (EIFEX): export under Fe-enriched conditions in the Southern Ocean

Since the SOIREE experiment (Southern Ocean Iron Release Experiment; Australian sector) and EisenEx (Iron Experiment) the role of Fe in enhancing Southern Ocean primary production and phytoplankton biomass has been evidenced (Boyd et al., 2000; Gervais et al., 2002), whereas its role in enhancing Southern Ocean export production was evidenced during the SOFEX experiment (Southern Ocean Fe Experiment; Buesseler et al., 2005; Pacific sector). However, it was not clear from SOFEX to what extent export production was enhanced, since field work was interrupted when the export was still high. The European Iron Fertilization Experiment (EIFEX; Atlantic sector, summer 2004) focused on the fate of the bloom induced by the iron addition: its export to mesopelagic water and its transfer to the food web. Both processes lead to carbon sequestration.

EIFEX took place in a mesoscale eddy pinched off from the meandering Polar Front. The water was characteristic of the Polar Front Zone. This eddy had low temperatures, high nutrient concentrations and was iron-depleted. There was evidence of quite large biological activity prior the experiment (pCO$_2$ undersaturation, large ^{234}Th deficit and large mesopelagic Ba$_{xs}$ concentrations (for the latter see section II.4.2). The eddy was fertilized with Fe and monitored for 36 days afterwards. A phytoplankton bloom dominated by diatoms was induced with chlorophyll contents reaching 2.9 µg l^{-1} three weeks after the iron infusion (*Klaas et al., Assmy et al.*, unpublished).

During the whole experiment, ^{234}Th activity was measured in the upper 1000m. Fluxes at 100m were calculated using a non steady state model (*Buesseler et al., 1992; Savoye et al.,* in press), which assumes supply and loss of ^{234}Th via horizontal and vertical mixing are small, relative to rates of ^{234}Th production from ^{238}U, ^{234}Th decay, and ^{234}Th loss on sinking particles. Because the horizontal ^{234}Th gradient was negligible and the turbulent diffusion coefficient was very low (2.10^{-4} m^2 s^{-1}; *Leach,* pers. com.), ^{234}Th diffusion was considered negligible. ^{234}Th advection has still to be checked, but physical processes have only been found to impact ^{234}Th activity balances significantly in sites of intense upwelling or coastal regions where tidal pumping and activity gradients are a larger component of the ^{234}Th activity balance (*Buesseler,* 1998).

The ^{234}Th export fluxes (**Figure II.15**) decreased to zero within the first two weeks after the iron infusion. Such a decrease of ^{234}Th flux (i.e. an increase in ^{234}Th activity) within ca. 15 days after the iron addition has also been reported during SOIREE (*Charette and Buesseler,* 2000). After this decrease ^{234}Th export fluxes increased until day 32, reaching values as high as 8000 dpm m^{-2} d^{-1} which lasted for a short period of four days (days 28-32). During the last four days of the experiment,

the ^{234}Th flux again decreased to 1400 dpm m^{-2} d^{-1}. A ^{234}Th flux value of 8000 dpm m^{-2} d^{-1}, is the highest ever recorded and suggests that the Fe- induced bloom broke up rather fast and sunk massively. However, when calculated over the time span between days 28 and 36, the ^{234}Th flux is only 4500 dpm m^{-2} d^{-1}, which is only about twice as large as the natural ^{234}Th export flux of 2600 dpm m^{-2} d^{-1} for the same area as reported *Usbeck et al.* (2002) and observed in the present study between days -1 and 9. When integrated over the full period of export (i.e. days 15 to 36), the sink of the Fe-induced bloom exported 44700 ± 8800 dpm m^{-2} d^{-1} of ^{234}Th. One of the main features of this study is that the experiment ran until the decrease of the export flux, in contrast to other iron experiments in the Southern Ocean.
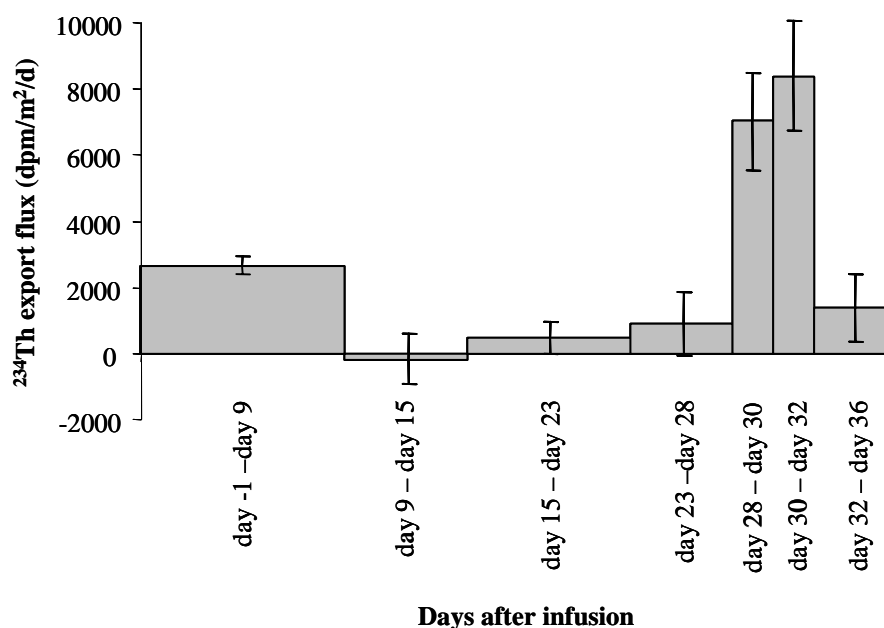
Figure II.15: ^{234}Th export flux during the European Iron Fertilization Experiment in the Atlantic sector of the Southern Ocean (summer 2004).

As discussed below in section II.4, the change of ^{234}Th vs. time during EIFEX is strikingly similar to the one of the meso-Ba$_{xs}$ although the two proxies are conceptually independent, giving confidence in the proxies and strengthening the conclusions drawn.

II.4 Organic matter mineralisation

II.4.1 Dissolved Ba and the Ba$_{xs}$ proxy

The potential of Ba$_{xs}$-Barite as a proxy of mesopelagic mineralization of sinking organic material derives from the role played by aggregates as micro-environments in which barite precipitates and which convey this mineral to mesopelagic waters, where it is released as micron-sized particles on degradation of the organic carrier (*Dehairs et al.,* 1997; *Cardinal et al.,* 2005). The exact mechanism by which barite precipitates remains debated, however. Ba subtraction from ambient solution, release of biogenic Ba or oxidation of organic sulfur are put forward as possible processes leading to BaSO$_4$ saturation inside biogenic aggregates, inducing barite precipitation. Other hypotheses involve the role of bacteria or Acantharia in mediating barite precipitation.

Providing clues on Ba dynamics will allow to better constrain the use of the Ba proxy, especially for reconstruction of organic matter mineralisation in intermediate and deep waters. Therefore, we investigated the dynamics of Ba cycle by confronting dissolved Ba (Ba$_d$) behavior with those of nutrients and alkalinity and by investigating particle – solute interaction. here We report results for the WOCE SR3 transect (Australian sector, SAZ'98 cruise, summer 1998 and CLIVAR-SR3 cruise, spring 2001; *Jacquet et al.,* 2004) Other data pertaining to the Crozet Kerguelen basin (Indian sector, ANTARES-4 cruise, 1999) were published in *Jacquet et al.,* 2005).

High resolution dissolved Ba section across the Southern Ocean

We examined the Ba$_d$ distribution over the whole water column along WOCE SR3 line (145°E) in the Southern Ocean (Australian sector, spring 2001; CLIVAR SR-3 cruise). Details regarding the cruise (location and strategy) were given in section I.3.2. Analytical methods for dissolved and particulate Ba are given in *Jacquet et al.* (2004; 2005) and *Cardinal et al.* (2005).

Figure II.16 shows the tight overprinting of the frontal zones by Ba$_d$ gradients, highlighting hydrodynamics as a major process controlling the Ba$_d$ distribution. However, biogeochemical processes are also acting as witnessed by enhanced Ba$_d$ contents in deep waters of the SAF zone and by a local mesopelagic minimum in the Inter PFZ.
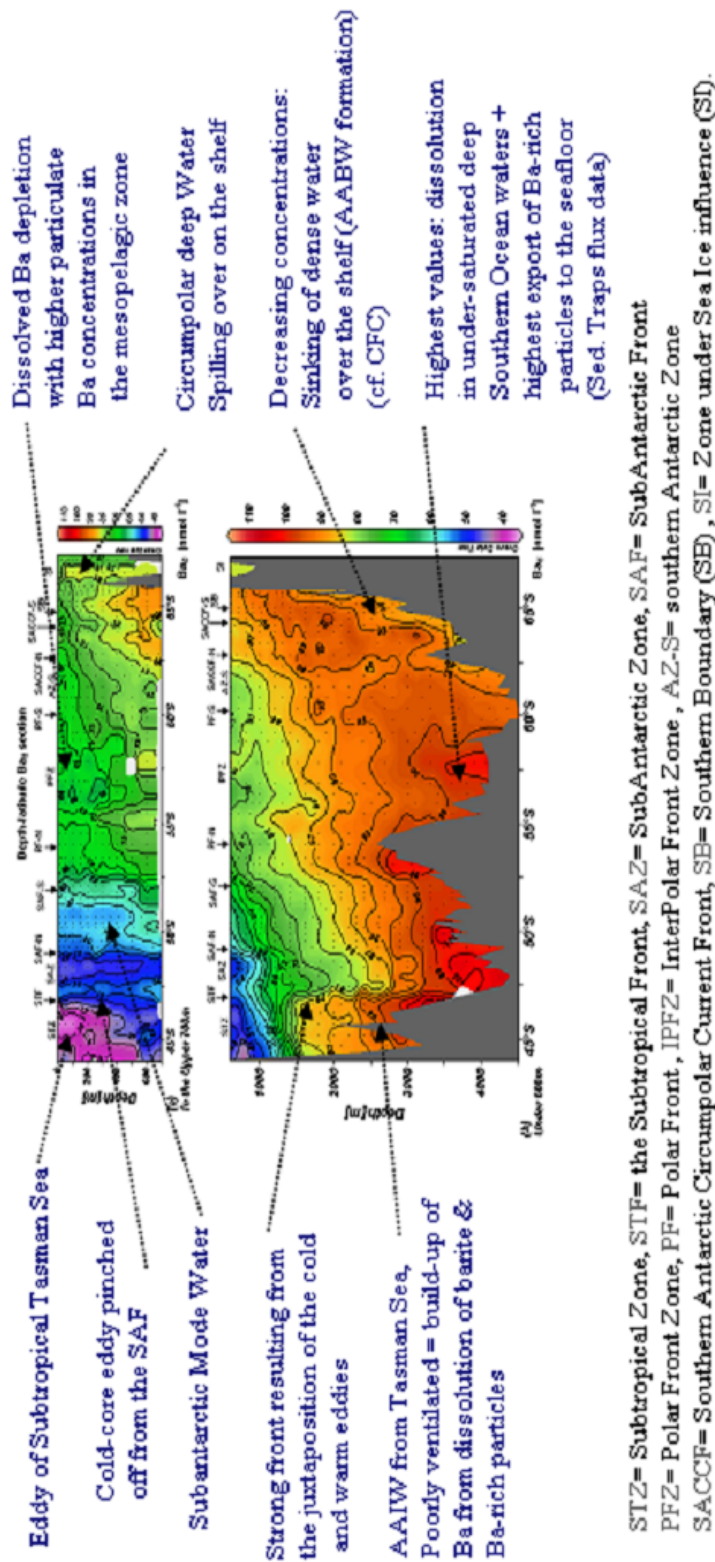
Figure II.16: High resolution whole water column Ba$_d$ distribution (nmol l^{-1}) along SR3 transect from Tasmania to Antarctica (October-November 2001); (a) in the upper 700m and (b) between 600m and seafloor. Position of fronts and zones are as given in *Sokolov and Rintoul* (2002).

These features are respectively ascribed to the dissolution of Ba-rich phases and possibly Ba transfer from solution to particles. The latter observation fits with the observation of higher particulate Ba concentrations in the mesopelagic waters at ~ 57°S (see discussion below). Between 47.5° and 53°S bottom waters reach the highest Ba_d values observed along the whole transect. This probably reflects dissolution of Ba-rich phases, such as barite, in the undersaturated deep Southern Ocean waters (*Monnin et al.,* 1999; *Rushdi et al.,* 2000). However, since deep water barite undersaturation prevails throughout the Southern Ocean basin, these high bottom water content probably also reflect higher export of Ba-rich particles to the seafloor between 47.5° and 53°S. This is corroborated by sediment trap flux data showing higher Ba fluxes in the deep water column at 47°-51°S compared to 54°S. It is also possible that the high Ba concentrations are due to epibenthic fluxes of Ba, in which case as well they would reflect a larger flux or rain rate of Ba-rich particles to the sea floor in the SAZ region.

Dissolved Ba versus nutrients and alkalinity

Regression analysis on the entire data set for spring (CLIVAR-SR3, 2001) indicates silicate and temperature explain 96 and 4% of the Ba variability, respectively (with silicate and alkalinity being multi-colinear). However, zooming in on surface and mesopelagic waters reveals (i) an inverse relationship between Ba and alkalinity; (ii) a correlation between Ba and nitrate and (iii) uncoupling of Ba and silicate (**Figure II.17**). In the intermediary and deep waters, on the contrary, Ba-silicate and Ba-alkalinity correlate positively, while Ba-nitrate relation becomes uncoupled. These regressions appear mainly driven by conditions in the intermediate (AAIW) and sub-surface water ($\sigma<27.55$), while throughout the deep basin (where
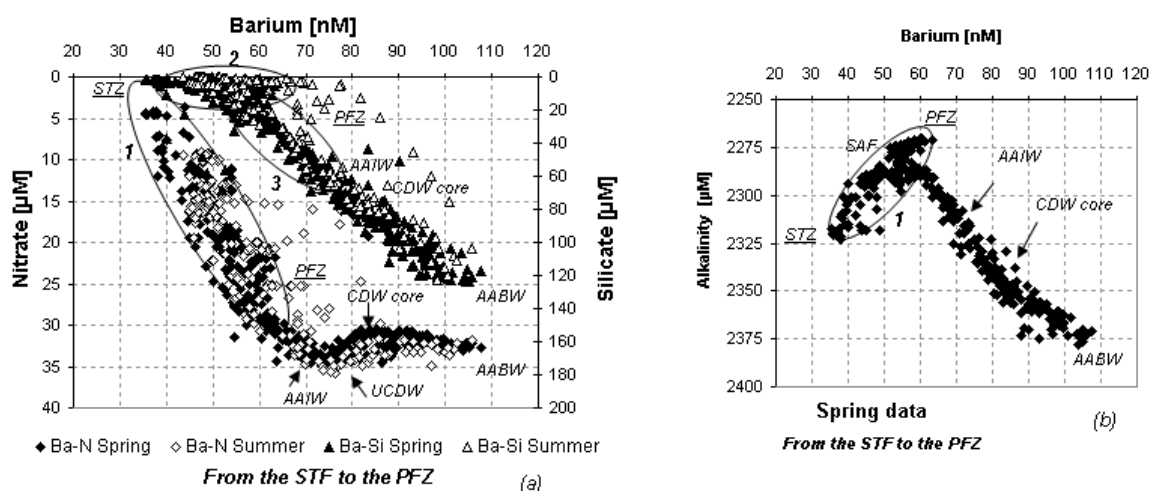
Figure II.17: Dissolved Ba (nM) versus (a) nutrients (silicate and nitrate; μM) and (b) alkalinity (μM) from the STF to the PFZ (CLIVAR-SR3 and SAZ'98 cruises).

Circumpolar deep water CDW and AABW are the dominant water masses) the Ba-silicate and Ba-alkalinity correlative behavior is much more homogenous. Dissolution of suspended biogenic barium and skeletal parts is the likely reason for this.

In the following section we confront dissolved and particulate Ba profiles obtained during different seasonal settings along WOCE SR-3 line (summer: SAZ'98 cruise, February – April, 1998; spring: CLIVAR-SR3 cruise; October – December, 2001), to investigate Ba seasonal dynamics.

Confrontation of spring and summer Ba data along WOCE SR-3 line (145°E)

We investigated the interlinkage between the dissolved and particulate Ba phases (**Figure II.18**). Summer Ba_d profiles show more variability than spring profiles in the upper 600 m and show depletions in the mesopelagic zone. Excess particulate Ba profiles (Ba_{xs} = an estimate of biogenic Ba from total particulate Ba after small corrections for lithogenic Ba, based on Al) display a maximum between ~150 and 450 m, with the average Ba_{xs} content in this depth region being systematically higher in summer than in spring. Differences in turn-over rate between the two Ba phases could explain why spring particulate Ba_{xs} maxima are not accompanied by significant Ba_d depletions. Considering that the first SR3 cruise took place in summer (SAZ'98; 1998) about 3 months later in the season compared to the second SR3 cruise (CLIVAR-SR3; 2001), a time window of several months seems necessary for the dissolved signal to build up the observed Ba_d depletion. We calculated the subsurface-mesopelagic Ba_d depletion over the growth season and compared this value with the increase of Ba_{xs} content in the mesopelagic and deep waters (see below, section II.4.2). During the spring 2001 cruise we noticed that the increase rate of mesopelagic Ba_{xs} between repeat visits (3 weeks interval) of some the study sites is about 10 times larger (~3.1 µmol m^{-2} d^{-1}) than the increase rates based on time spans of 3 months (from 0.3 to 0.7 µmol m^{-2} d^{-1}; i.e. the difference between the summer and spring cruise values) and is more similar to the calculated Ba_d subtraction rates (from 4.6 to 11.7 µmol m^{-2} d^{-1}). This may indicate that the mesopelagic Ba_d depletion reflects Ba uptake integrated over the growth season (a few months), while the Ba_{xs} stock fluctuates much more on a shorter time scale (a few weeks) as tuned for instance by pulses in primary production and export.

It is interesting to note similarities between Ba_d subtraction and Ba_{xs} flux in the deep ocean (the latter = sediment trap data; *Cardinal et al.,* 2005). Deep sea Ba_{xs} fluxes (from 0.4 to 1.2 µmol m^{-2} d^{-1}) explain about one tenth of the mesopelagic Ba_d subtraction, but latitudinal trends between both are similar: Ba_d subtraction is larger in the SAZ compared to PFZ and likewise, sediment trap Ba_{xs} fluxes in the SAZ are larger than in the PFZ (*Cardinal et al.,* 2001; 2005) mimicking the trend observed for

sediment trap carbon fluxes (*Trull et al.,* 2001). These conditions potentially reflect the role of $CaCO_3$ mineral ballast in favoring deep export north of the PF, while dominance of diatoms south of the PF would favor mineralization in mesopelagic waters (*Savoye et al.,* 2004; *Cardinal et al.,* 2005), in agreement with conclusions by *François et al.* (2002) on the respective role of $CaCO_3$ and opal as particle ballast.

Overall our results highlight the interlinkage between dissolved and particulate Ba and the sensitivity of dissolved Ba to biological processing.
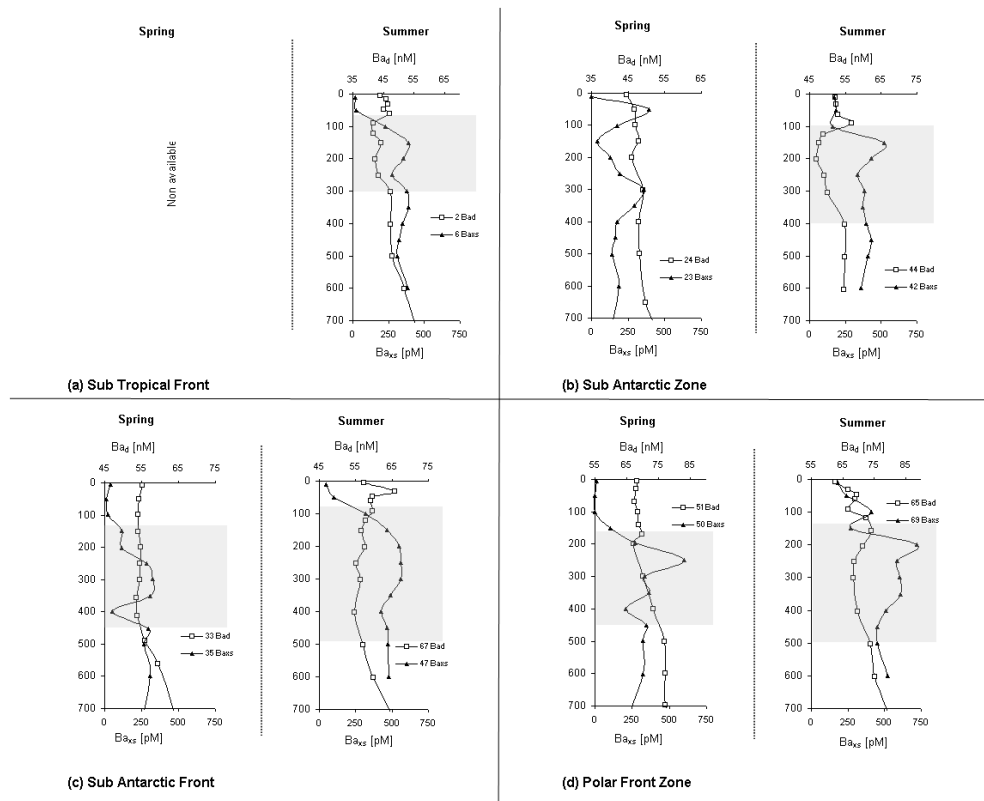
Figure II.18: Spring and summer dissolved (open squares curve, nM) and particulate (full triangles curve, pM) Ba profiles in the first 1000 m water column (SAZ'98 and CLIVAR-SR3 cruises). Shaded areas identify the occurrence of the dissolved Ba depletion facing high particulate Ba_{xs} contents.

II.4.2 Mesopelagic excess-Ba and organic matter mineralisation

Water column profiles of excess particulate Ba (Ba_{xs}; see section II.4.1) were measured in the upper 1000m during CLIVAR-SR3 (spring 2001; WOCE SR3 line, 145°E) and EIFEX (summer 2004; Polar Front Zone, Atlantic sector; see section II.3) cruises (*Cardinal et al.,* 2001). A recurrent feature for the Southern Ocean (and elsewhere) is the presence of a mesopelagic Ba_{xs} maximum (*Dehairs et al.,* 1991,

1992, 1997; *Cardinal et al.,* 2001). For CLIVAR-SR3 all profiles display such a mesopelagic Ba_{xs} maximum between ~150 and 450m (*Cardinal et al.,* 2005 DSR), while for EIFEX this Ba_{xs} maximum is less pronounced, but is spread out over a 1000m depth layer.

CLIVAR-SR3

      The latitudinal variation of mesopelagic Ba_{xs} (meso-Ba_{xs}150-400m) is shown in **Figure II.19**. The continuous increase of meso-Ba_{xs} (meso-Ba_{xs}) from SAZ to PFZ reported for late summer 1998 (SAZ'98 cruise; *Cardinal et al.,* 2001) was observed again during the CLIVAR SR-3 spring cruise, reflecting consistency of the regional Ba signal over the years. Note that average deep Ba_{xs} fluxes from sediment traps exhibit the reverse pattern, i.e., higher fluxes in the SAZ compared to the PFZ (no deep sea flux data are available for the area further south; >55°S). Deep sea Ba_{xs} fluxes closely follow POC fluxes (*Trull et al.,* 2001; *Cardinal et al.,* 2005-DSR), a feature that will be addressed in the next section. A clear seasonal evolution is observed for meso-Ba_{xs} contents, which are systematically higher during late summer (SAZ'98) compared to spring (CLIVAR-SR3).

      The repeat station at 60.9°S (CLIVAR-SR3 cruise) is characterized by a dramatic meso-Ba_{xs} increase between the first and second visit, 17 days later (**Figure II.19**). This increase over time emphasises the general latitudinal trend of increasing Ba_{xs} contents south of the SAF and confirms the evidence of seasonal evolution. Interestingly, nitrogen-uptake (except at 64.9°S) and cell numbers were the highest during the first sampling at 60.9°S (*Savoye et al.,* 2004a and section II.2). Moreover between the two visits a large increase of biomass and [234]Th deficit occurred (*Savoye et al.,* 2004b and section II.3 above) whereas N-uptake, new production and cell numbers decreased (*Savoye et al.,* 2004a). Indeed at this station, a comparison of the flux results based on each of the three proxies during the two successive samplings enables a reconstruction of the dynamics of C production export from the mixed layer and mesopelagic mineralisation. During the first visit production was high in the mixed layer, and [234]Th flux data indicate that the produced biomass was not yet converted to a high particle export (see section II.3 and *Savoye et al.,* 2004b). However, during the second visit the effects of high biological activity were translated into biomass, increased [234]Th deficit (i.e. carbon export flux) and mesopelagic Ba_{xs} content. It thus appears that mixed layer Ba_{xs} was transferred to the mesopelagic zone within three weeks via the transport (export) of relatively large particles (most of Ba_{xs} was associated with particles larger than 20µm in the mixed layer, *Cardinal et al.,* 2005 DSR). Since the Ba_{xs} decrease in the mixed layer does not account for the increase in the mesopelagic layer, underway barite precipitation must have occurred within the large particles and aggregates.
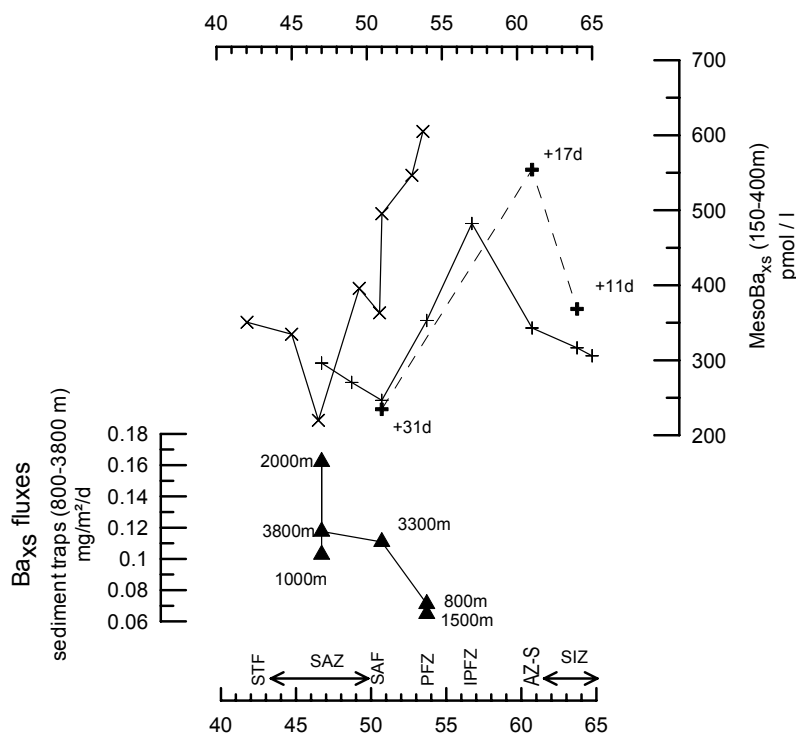
Figure II.19: WOCE SR3 section south of Tasmania (140° - 145°E). Top: latitudinal variation of mesopelagic Ba_{xs} content; x = data for the SAZ'98 summer cruise; + = data for the CLIVAR-SR3 spring cruise. Bottom: deep ocean Ba_{xs} sediment trap fluxes at indicated mooring depths.

This general scenario fits with the preferential pathway put forward by Chow and *Goldberg* (1960) and *Bishop* (1988) and in which aggregates play a central role. Furthermore, *Ganeshram et al.* (2003) report that labile Ba carried by phytoplankton is easily released when phytoplankton is left to decay and leads to the formation of barite micro-crystals. Our data confirm that the final step setting the mesopelagic Ba_{xs} signal involves the release of discrete barite particles from remineralised aggregates in the mesopelagic zone as demonstrated by *Dehairs et al.* (1997). Furthermore, the latter authors reconstructed O_2 consumption from meso-Ba_{xs}. Clearly, meso-Ba_{xs} is very sensitive to progress of the growth season but reacts with a delay and it took somewhat less than three weeks for the signal of high phytoplankton activity to be transferred to the mesopelagic layers as a result of export and mineralisation.

<u>EIFEX</u>

Temporal variation of meso-Ba_{xs} during the EIFEX in situ Fe enrichment experiment (Polar Front Zone, Atlantic sector; summer 2004; see section II.3) are shown in **Figure II.20**. Meso-Ba_{xs} contents where high before Fe infusion, indicating that a bloom-supported relatively high POC export and mineralization was ongoing

some time before (days-weeks) the start of the EIFEX experiment, well in agreement with other data like nutrients, phytoplankton counts (*P. Assmy*, pers. comm.), POC and BSi contents (*C. Klaas*, pers. comm.) and, [234]Th deficit (section II.3). Evolution of the mesopelegic Ba_{xs} content suggested thet mesopelagic mineralization increased between day 11 and 20 and reached its maximum at day 29 for in-patch stations; thereafter the Ba_{xs} signal decreased again. [234]Th-deficit followed a similar pattern (**Figure II.15**) and mixed layer diatom cells numbers were the highest at day 25, decreasing afterwards in accordance with evidence of a decaying bloom (*P. Assmy,* pers. comm.).
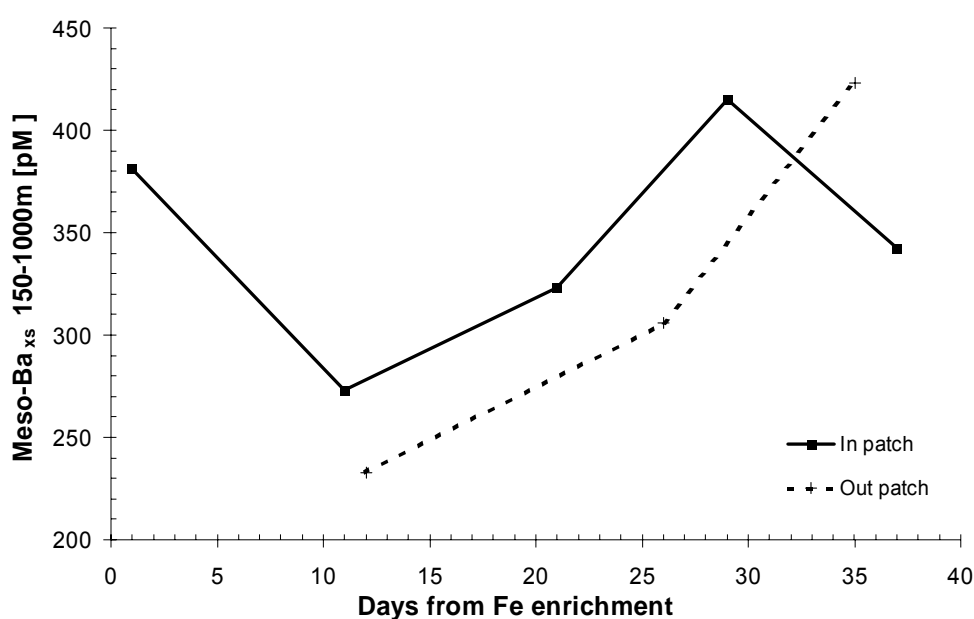
Figure II.20: EIFEX Fe fertilization experiment; summer 2004, Atlantic sector. Depth weighted average mesopelagic Ba_{xs} content (150 – 1000m) inside and outside the Fe fertilized patch.

There is a striking similarity between the temporal trends of meso-Ba_{xs} for the in- and out-patch stations too, but with a 5-10 days delay. Therefore, in contrast to the situation in surface waters, the differentiation between in and out patch does not hold for mesopelagic waters, probably due to the physical properties of the eddy. Meso-Ba_{xs} data indicate that the export from the mixed layer has induced mesopelagic POC mineralization over a broad area, and not just in waters underlaying the surface fertilized patch. This calls for the necessity to adopt a 3D approach for biogeochemical studies in such eddies.

Overall these results suggest that Fe enrichment has induced carbon export and mesopelagic mineralisation starting 10 days from Fe infusion. Increasing export and mineralisation was sustained during the next 20 days (i.e. up to ~day 30) and then started to decay. The maximum of mesopelagic remineralisation was however not higher than the one naturally occurring just before the Fe induced bloom contrasting with the very large ^{234}Th deficit measured between days 28 and 32. Even if these meso-Ba$_{xs}$ and ^{234}Th measurements have not been translated into C fluxes yet, they indicate a likely limited impact of Fe enrichment on the oceanic carbon cycle at both time and spatial (water column) scales.

II.4.3 ^{234}Th excess: toward a new proxy of remineralization in mesopelagic waters

Even though mesopelagic ^{234}Th data were reported since the first study of ^{234}Th in the ocean (*Bhat et al.,* 1969), mesopelagic ^{234}Th was poorly sampled and even less discussed. This is mainly because the surface water was of interest and because ^{234}Th is usually in secular equilibrium with ^{238}U below the mixed layer. However, mesopelagic ^{234}Th excess with respect to ^{238}U has been reported in coastal and shelf waters (e.g. *Amiel et al.,* 2002; *Coppola et al.,* 2002) as well as in all main oceans: Indian Oceans (*Bhat et al.,* 1969; *Buesseler et al.,* 1998), Atlantic Ocean (*Charette and Moran,* 1999), Pacific Ocean (e.g. *Coale and Bruland,* 1987; *Murray et al.,* 1996) and Southern Ocean (e.g. *Rutgers van der Loeff et al.,* 1997; *Buesseler et al.,* 2001).

In fact, only four recent studies clearly discuss about mesopelagic ^{234}Th excess. In a yearly time-series study with monthly sampling, *Benitez-Nelson et al.* (2001) report that either surface or mesopelagic export appears to be the source of mesopelagic remineralization, depending of the period of the year, in the North Pacific Subtropical Gyre. *Usbeck et al.* (2002) have found that the balance between ^{234}Th surface export and mesopelagic remineralization reconciles the discrepancies between high production rates and low sediment trap material in the Weddell Gyre (Southern Ocean). *Savoye et al.* (2004b) compared the depth profiles of ^{234}Th, density, oxygen concentration and Ba$_{xs}$ — a proxy of mesopelagic remineralization — in the Southern Ocean and found that these profiles nicely superpose (**Figure II.21**). *Buesseler et al.* (2005) report that the mesopelagic ^{234}Th excess was persistent and decreasing in iron depleted and iron enriched waters, respectively, in the course of the Southern Ocean Iron Experiment; authors argued that it implied a change in the nature of sinking particles (i.e. faster settling, less labile) and/or a

subsurface change in the processes responsible for remineralization (e.g. change in zooplankton migration for feeding).
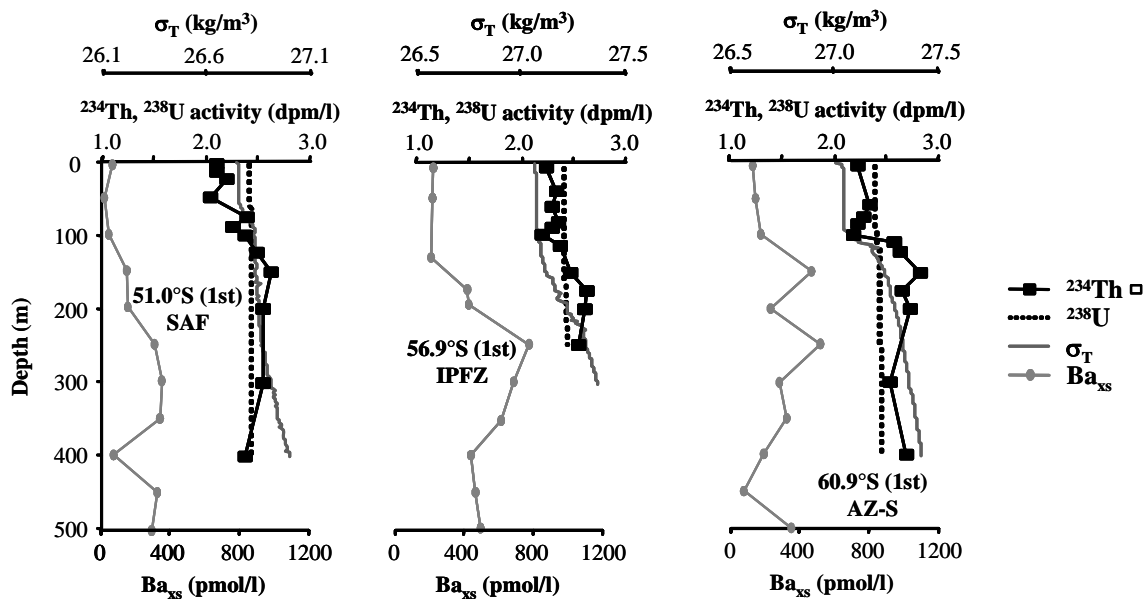
Figure II.21: ^{234}Th and ^{238}U activity, density (σ_T) and biogenic particulate barium (Ba_{xs}) profiles during the CIIVAR-SR3 cruise in the Australian sector of the Southern Ocean (spring 2001). SAF, IPFZ, AZ-S: see Figure Th1. Note the ^{234}Th excess with respect to ^{238}U below the mixed layer.

Thus, at depths where ^{234}Th and ^{238}U activities are normally at secular equilibrium, or are close to, processes that could explain the observed ^{234}Th excess are (1) particle accumulation and (2) particle remineralization (i.e. transfer of ^{234}Th from particulate to dissolved phase). Indeed, the only *in situ* source of ^{234}Th in seawater is ^{238}U decay which leads to a maximal $^{234}Th{:}^{238}U$ ratio of 1 when secular equilibrium is reached. So, only non-local particulate sources coming from upper layers can leads to ^{234}Th excess in open ocean. In most of the cases, ^{234}Th excess appears below the mixed or euphotic layer, i.e. in a layer where particles are not produced. To accumulate, particles need to not sink or to sink slowly. Mesopelagic accumulated particles come either from surface particles which sink slowly or from surface fast-sinking particles which break-up or disaggregate within the mesopelagic layers. As soon as particles accumulate in the mesopelagic layer, their remineralization may become an important source of dissolved ^{234}Th.

^{234}Th fluxes responsible for mesopelagic ^{234}Th excess have been calculated to be up to 1100 dpm m^{-2} d^{-1} in the North Pacific Subtropical Gyre (*Benitez-Nelson et al., 2001*) and 3800 dpm m^{-2} d^{-1} in the Australian sector of the Southern Ocean (*Savoye et al., 2004b*). The conversion of these ^{234}Th fluxes into carbon fluxes (e.g. by using a dedicated C/^{234}Th ratio representative of the involved processes) would be highly

interesting in the study of carbon sequestration by the global ocean. This represents a challenge for future studies.

II.4.4 Carbon remineralisation fluxes

In **Table II.4** we have translated the meso-Ba_{xs} data into remineralized carbon fluxes by using the relationship (equations 6 and 7) empirically obtained in *Dehairs et al.* (1997) and we compare these respired carbon fluxes to new production estimates from *Elskens et al.* (2002) for the summer SAZ'98 cruise and from *Savoye et al.* (2004a) for the spring CLIVAR SR3 cruise.

$$J_{O_2} = (mesoBa_{xs} - Ba_{bkg})/17199 \qquad \text{eq. 6}$$

$$C_{respired} = 250 \times J_{O_2} \times RR \qquad \text{eq. 7}$$

Where JO_2 is the O_2 consumption in μmol l^{-1} d^{-1}; Ba_{bkg} is the Ba_{xs} background in the water column (here taken as 200 pmol l^{-1} in accordance with Dehairs et al. 1997 and the average deep Ba_{xs} contents during CLIVAR-SR3 and SAZ98, **Figure II.19**); $C_{respired}$ is the carbon remineralised rate (in mmolC m^{-2} d^{-1}) and RR the Redfield O_2:C mole ratio (175:127).

Table II.4 : Comparison between new production estimates and mesopelagic respired carbon for spring 2001 (CLIVAR-SR3 and summer (SAZ'98). From *Cardinal et al.* (2005).

Latitude	Zone	NP[a] (mgC m^{-2} d^{-1})	Export production[b] (mgC m^{-2} d^{-1})	Respired C[c] (mgC m^{-2} d^{-1})	Zonal average respired[d] (%)
Spring					
46,9	SAZ	-	117	12	
48,8	SAZ	69		9	
51,0	SAF	55	256	6	
51,0	SAF[e]	98		4	9.4 ± 4.4
53,7	PFZ	49	22	19	
56,9	IPFZ	92	45	36	39 ± 0.3
60,9	AZ-S	221	*475*	18	
60,8	AZ-S[e]	153		45	
63,9	SIZ	202	*667*	15	
63,9	SIZ[e]	100		21	
64,9	SIZ	291	153	13	25 ± 6[e]
Summer					
42,0	STF	35		19	
45,0	SAZ	150		17	
46,8	SAZ	56		3	
49,5	SAZ	62		25	
50,9	SAF	22		21	
51,0	SAF	57		37	45 ± 34
53,0	PFZ	37		44	
53,7	PFZ	41		51	122 ± 5

[a] New Production estimates are based on N uptake results from Elskens et al. (2002) for summer (SAZ98) and from Savoye et al. (2004a) for spring (CLIVAR-SR3).

[b] Export production is calculated from ^{234}Th deficit (Savoye et al., 2004b). See text for details

[c] Respired C is estimated from the Dehairs et al. (1997) relationship between meso-Ba_{xs} and O_2 consumption. Summer Ba_{xs} are from SAZ98 (Cardinal et al., 2001) and spring Baxs from this study

[d] Zonal average respired is the average NP:Respired C ratio (in %) per system (STF/SAZ/SAF, PFZ/IPFZ and AZ-S/SIZ).

[e] Refers to repeat CLIVAR SR-3 stations only.

Carbon respired (from meso-Ba_{xs}) appears to account for a larger fraction of carbon exported (from New Production, NP, that can be considered as exportable C production, **Section II.2** and *Savoye et al.*, 2004a) in the PFZ and south of the PF, compared to the SAF and SAZ (**Table II.4**). This is clearly seen in the PFZ-IPFZ system where 39±0.3% (spring) and 122±5% (summer) of the exported carbon is remineralised in the mesopelagic zone whereas this proportion decreases to 9.4±4.4% (spring) and 45±34% (summer) in the SAZ-SAF characterized by a highly variable contribution of new production to total production (variable *f*-ratio; *Elskens et al.*, 2002; *Savoye et al.,* 2004a). For the AZ-S and SIZ only spring data are available and these show quite a large variability (14 ± 8 %).

When considering only the repeat stations of AZ-S and SIZ the remineralized carbon fraction reaches 25 ± 6 %, quite similar to the values observed in PFZ-IPFZ. These higher remineralisation rates in the PFZ - IPFZ and AZ-S - SIZ are also reflected by the [234]Th results for the same cruise (*Savoye et al.*, 2004b), showing higher mesopelagic [234]Th-excess in IPFZ and SIZ compared to SAF. Moreover, *Savoye et al.* (2004b) report vertical [234]Th activity gradients which are very similar to those of Ba_{xs} and density (**Figure II.21**) and propose [234]Th-excess activity as a potential remineralization proxy.

These variations of reconstructed remineralisation efficiencies reconcile the opposite latitudinal patterns of meso-Ba_{xs} and deep Ba_{xs} fluxes along SR-3 (**Figure II.19**). They are moreover well in accordance with the recent review of POC fluxes from world ocean sediment traps (*François et al.*, 2002) showing calcium carbonate secreting phytoplankton to be relatively more efficient in terms of deep C export and vertical transport, probably as a result of a ballast effect (*Ittekkot et al.,* 1992; *Klaas and Archer,* 2002) while diatom dominated production systems are reported to be more prone to efficient mineralisation in mesopelagic waters. This is what our observations for meso-Ba_{xs} and deep Ba_{xs} fluxes stress: higher carbon remineralisation in the AZ-S where diatoms are a major contributor of the phytoplankton biomass, but higher deep carbon fluxes in SAZ where coccolithophorids were observed to be a major component of the phytoplankton community for C export (*Trull et al.,* 2001b).

Our findings on regional differences in deep export pattern between SAZ and PFZ are also supported by the nutrient depletion data estimating higher C export in the SAZ than in the PFZ (*Lourey and Trull, 2001*), by the C fluxes measured in sediment traps (*Trull et al.,* 2001b) and by N-uptake (a proxy of exportable C from the mixed layer) and [234]Th deficit (a proxy of particle export from the upper 100m) from the CLIVAR-SR3 cruise (section above and *Savoye et al.,* 2004a, b). Our data south of the PFZ are restricted to spring and we do not yet have sediment trap results from

the AZ that would detail the latitudinal pattern of deep POC export. Additional data on sediment traps and core tops from the study area are needed to confirm this view.

In the SAZ, SAF and PFZ, we observed that summer remineralisation rates and efficiencies were higher than in spring (**Table II.4**) whereas in terms of NP they are slightly higher in spring than in summer (*Savoye et al.,* 2004a). For instance during summer in the PFZ, it seems that all the new production is remineralised in the upper mesopelagic zone. Although spring blooms have been reported to sustain high C export in the Southern Ocean (*Laubscher et al.,* 1993; *Rutgers van der Loeff et al.*, 1997; *Brzezinski et al.,* 2001), they occur over short time scales and consequently account for only a fraction of the annual C export (Rutgers van der Loeff et al., 2002). For instance, by integrating observations during spring, summer and fall in the Ross Sea, *Cochran et al.* (2000) report higher C fluxes from the mixed layer in summer and fall compared to spring. Our meso-Ba$_{xs}$ data indicate that on a monthly time scale, mesopelagic remineralisation is clearly more important in summer than in spring. This is also the case for the deep POC fluxes from the sediment traps (*Trull et al.,* 2001b).

II.4.5 Effect of Fe on bacterial activity and mineralization of phytoplankton-derived DOM: experimental work

Introduction

Heterotrophic bacteria may influence the efficiency of carbon export through the remineralisation of particulate organic matter POM associated to the aggregates but also of dissolved organic matter (DOM). Indeed, the seasonal persistence of dissolved organic carbon can participate to carbon exportation by the advection of surface water masses to deeper depth. Such persistence of DOM in the surface water and/or slowly degradability of POM during its export indicate that some factors limit bacterial utilisation of the available organic carbon. Iron, an essential nutrient, which limits primary productivity in the HNLC regions, has been put forward as one of the factors limiting the bacterial growth in the Southern Ocean (*Tortell et al.* 1996). Nevertheless, the extent to which Fe regulates bacterial dynamics in the HNLC area remains unresolved. The response of heterotrophic bacteria to iron supply might be twofold: either directly to the Fe supply and/or indirectly due to the supply of higher concentration and/or better quality of organic substrates derived of iron-enhanced phytoplankton production (*Pakulski et al.* 1996; *Church et al.* 2000; *Kirchman et al.* 2000). In this work, the response of bacterial community to the iron supply was investigated through re-growth experiments monitoring the bacterial response to organic substrates derived from *Phaeocystis antarctica* and two diatoms

Chaetoceros dichaeta and *Thalassiosira gravida* grown under iron-enriched and -deplete conditions.

In particular, we studied the resulting effect of iron limitation on genetic diversity, specific bacterial activities (5-cyano-2,3-ditotyl tetrazolium chloride (CTC) reducing cells, SYTOX positive cells), ectoenzymatic activities, growth rates, growth efficiency and organic carbon utilisation. Our results will be presented and discussed in term of significance on the efficiency of the carbon biological pump.

Material & methods

Experimental procedure- Re-growth experiments were realised by mixing phytoplankton-derived organic matter with an inoculum (10 %) of Antarctic bacteria. Phytoplankton-derived organic matter was prepared from pure cultures of *Phaeocystis antarctica, Chaetoceros dicheata and Thalassiosira gravida.*

Phytoplankton cultures- Phytoplankton were grown and acclimated for several generations to enriched (+2nM) and low iron Antarctic seawater (<1nM). Cultures were grown in an illuminated and thermostatised culture cabinet (RUMED) at 2°C and with a day:night cycle of 16 h: 8 h at 180 µE m^{-2} s^{-1}. An inoculum (15 ml) of phytoplankton pre-adapted to iron-deplete and -enriched conditions was respectively added to 20L low-iron and iron-enriched Antarctic seawater.

Bacteria- The bacteria inoculum was prepared from an Antarctic seawater sample (Ross Sea, November 2002) by pre-incubating these bacteria in low (<1nM) and enriched iron (>2nM) Antarctic seawater. Bacteria were grown in the dark at 2°C.

As shown in **Figure II.22**, two pools of organic matter were prepared from exponentially growing phytoplankton cultured under low (phyto -Fe) and enriched (phyto +Fe) iron conditions: (I) DOM (Dissolved Organic Matter) obtained by gently filtration (< 0.3 atm) onto 0.1 µm Nuclepore filters, (II) TOM (Total organic matter) including DOM and POM (Particulate organic matter) obtained after artificially induced phytoplankton lysis in an ultrasonic bath. In the case of *Thalassiosira gravida*, one extra set of re-growth experiments was realised including organic matter derived from Fe-depleted phytoplankton culture but inoculated at time 0 with 2.5 nM FeCl$_3$.
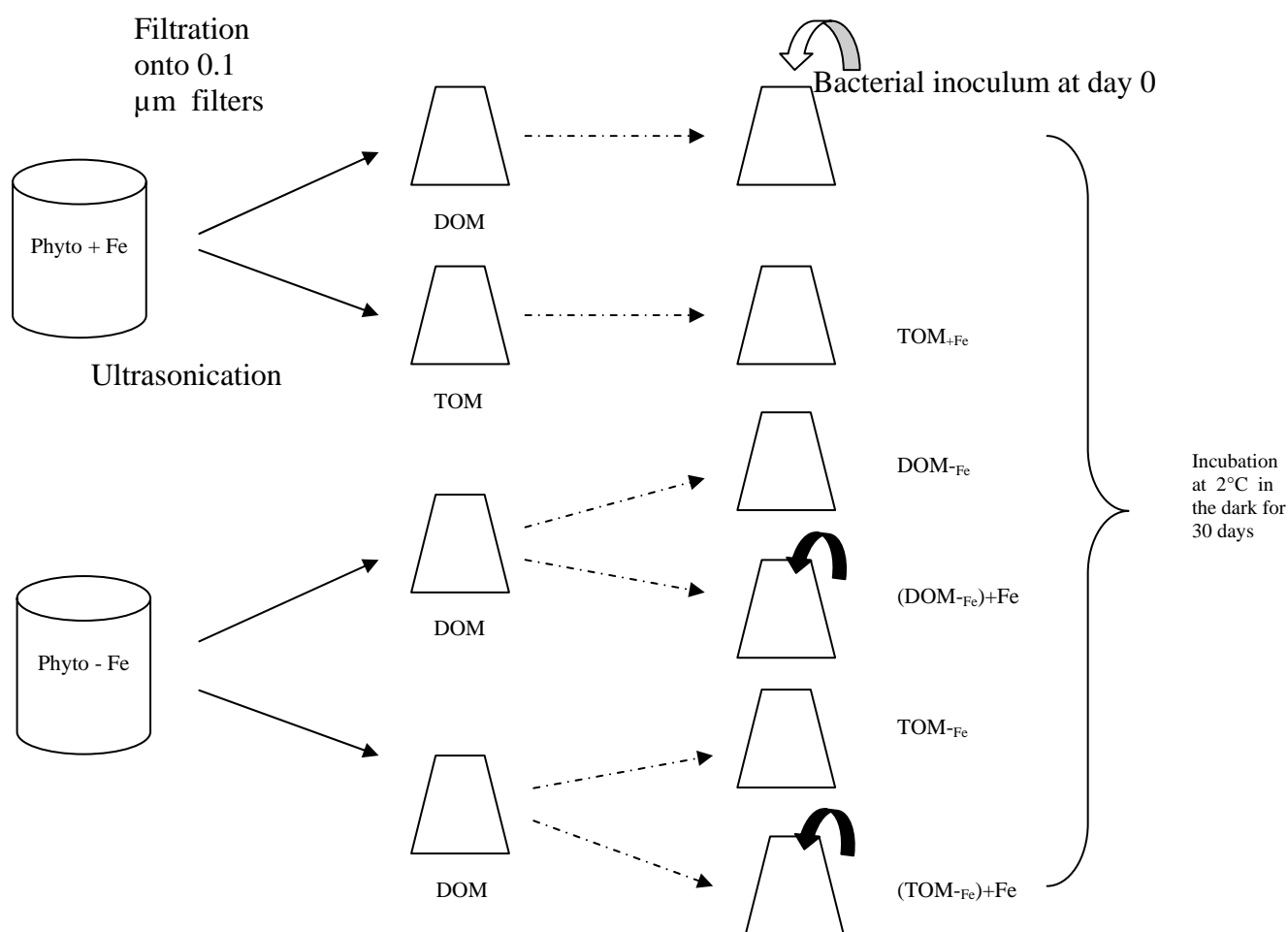
Figure II.22: Scheme of re-growth experiments conducted under laboratory controlled conditions.

Bacteria were inoculated in the organic matter filtrate (2 L) in a 1:10 volume ratio. The bioassays were then incubated at 2°C in the dark for about 30 days. Sub-samples were taken to monitor the time-evolution of bacterial biomass, genetic diversity, CTC and SYTOX positive cells, enzymatic activities, bacterial growth rates, bacterial growth efficiency and organic carbon utilisation.

Analytical procedures

Iron- Samples were acidified to pH<2 with ultraclean quartz distilled concentrated nitric acid. Total dissolvable iron (unfiltered) was measured according to a chemiluminescence method adapted from *Obata et al.* (1993) (see *Bucciarelli et al.,* 2001).

Chl-a- Chlorophyll *a* was quantified fluorimetrically following *Yentsch and Menzel* (1963).

POC/PON- Particulate organic carbon and nitrogen was analysed with a Carlo Erba NA 2000 elemental analyser.

DOC and TOC- Organic carbon was measured by high temperature catalytic oxidation (HTCO; procedure of Sugimura & Suzuki, 1988) with a Dohrmann Apollo 9000 analyser. The biodegradable organic matter (BOC) was measured by the method proposed by Servais (1989). This method relies upon the measurement of organic carbon (DOC-dissolved organic carbon and TOC-total organic carbon) in re-growth experiments before and after incubation for 30 days. BOC was calculated as the difference between the initial and final OC concentrations.

Bacterial biomass- bacterial biomass was determined by epifluorescence microscopy after DAPI staining (*Porter & Feig* 1980).

DGGE- The genetic diversity was analysed using denaturing gradient gel electrophoresis of PCR-amplified 16S rRNA genes. The DNA extraction, PCR-DGGE was made according to *Schäfer & Muizer'*s methods (2001). Primer combination: 341F-GC/907R. DGGE fingerprints were processed by image analysis (DOC-PRINT, Proxylab). For genetic diversity analysis, one band on the electrophoresis gel was considered as one species.

CTC positive cells- The number of 5-cyano-2,3-ditotyl tetrazolium chloride (CTC) reducing bacteria were determined by using a final concentration of 2.5 mM CTC and incubating the sample at 2°C for 2 h (Rodriguez *et al.*, 1992).

SYTOX positive cells- The number of SYTOX positive bacterial cells were determined by using a final concentration of 1 µM SYTOX GREEN (molecular probes) and incubating the sample at 37°C for 10 min. The number of SYTOX negative bacterial cells (cells with intact membranes) was determined by difference between total bacterial cell (enumerated with DAPI) and SYTOX positive bacterial cell numbers.

Ectoenzyme activities- Ectoenzyme activities (ectoprotease and ecto-ß-glucosidase) were measured at 2°C after addition to the sample of a saturating concentration of artificial substrates (L-Leucine-7-amino-4-méthylcoumarin and 4-methylumbelliferyl-β-glucoside) that produce fluorescent products when hydrolysed by ectoenzymes present in the sample.

Bacterial growth rate- Bacterial cell production was estimated by incorporation of ^{3}H-thymidine (*Fuhrman & Azam*, 1982). The specific growth rates (µ, h^{-1}) were calculated using the following model: specific growth rate µ = ln (1+P/N), where P is the bacterial cell production and N is bacterial abundance.

Bacterial growth efficiency- Bacterial growth efficiency (BGE) was calculated from the rate of decline in organic carbon and the rate of increase in bacterial biomass in the re-growth-experiments.

Results and discussion

1. Iron control on organic matter quantity and quality

Dissolved organic carbon concentrations were 1.4 to 3.3 times higher in the iron-enriched conditions than in deplete ones. Interestingly, DOC decreased for *Phaeocystis antarctica* growing in the iron-enriched conditions and was in the same order of magnitude than POC. The control of iron on the organic matter quality wasn't so clear. On one hand, the C/N ratios for *Phaeocystis antarctica* cultures differed significantly between iron-enriched and iron-deplete conditions. On the other hand, C/N ratios for *Thalassiosira gravida* cultures were around 5 and non-significantly different in both iron conditions. Very few studies have investigated the iron effect on the phytoplankton Redfield ratio and the C/N ratio can either decreased or increased or still remained roughly constant (Kudo *et al.* 2000, *van Leeuwe et al.* 1997, *Sarthou et al.* 2005).

The particulate organic carbon increased by a factor 3 for *Phaeocystis antarctica* and *Thalassiosira gravida* cultures and by a factor 21 for *Chaeoceros dichaeta* culture (**Table II.5**). This trend also was observed in other laboratory experiments (*Martin & Fitzwater* 1988; *de Baar et al.* 1990; *Buma et al.* 1991) and *in situ* iron enrichment experiments (*Boyd et al.* 2000, *Gervais et al.* 2002).

Table II.5: Chlorophyll a, particulate organic carbon (POC) and nitrogen (PON), dissolved organic carbon (DOC), C/N ratio and iron concentrations in the phytoplankton cultures (*Phaeocystis antarctica*, *Chaetoceros dichaeta*, *Thalassiosira gravida*) grown under Fe-deplete (-Fe) and enriched (+Fe) conditions.

Parameters	*Phaeocystis antarctica*		*Chaetoceros dichaeta*		*Thalassiosira gravida*	
	-Fe	+Fe	-Fe	+Fe	-Fe	+Fe
Iron, nM	0.85	2.76	<1*	>2*	1.13	3.71
Chlorophyll a, µg l^{-1}	0.39	8.7			0.08	3.25
POC, µgC l^{-1}	360	1070	240	5130	53	140
PON, µgN l^{-1}	52	253			11	32
C/N (mol/mol)	8.1	4.9			5.9	5.1
DOC, mgC l^{-1}	1.81 +/- 0.21	1.06 +/-0.15	2.34 +/-0.21	7.74 +/-0.19	1,23 +/-0.11	1.71 +/-0.22

Dissolved organic carbon concentrations were 1.4 to 3.3 times higher in the iron-enriched conditions than in deplete ones. Interestingly, DOC decreased for *Phaeocystis antarctica* growing in the iron-enriched conditions and was in the same order of magnitude than POC. The control of iron on the organic matter quality wasn't so clear. On one hand, the C/N ratios for *Phaeocystis antarctica* cultures differed significantly between iron-enriched and iron-deplete conditions. On the other hand, C/N ratios for *Thalassiosira gravida* cultures were around 5 and non-significantly different in both iron conditions. Very few studies have investigated the iron effect on the phytoplankton Redfield ratio and the C/N ratio can either decreased or increased or still remained roughly constant (*Kudo et al.* 2000, *van Leeuwe et al.* 1997, *Sarthou et al.* 2005).

2. Iron control on the bacterial community composition and activities

In these experiments, the bacteria can be co-limited by two major factors; the availability of iron and the quantity/quality of organic matter. The effect of iron alone was investigated only in the *Thalassiosira gravida* experiment ((DOM-Fe)+Fe, (TOM-Fe)+Fe). The current view is that bacterioplankton are not directly Fe limited, but rather carbon-limited as a consequence of the low primary production of Fe-limited phytoplankton (*Hutchins et al.* 1998; *Church* et *al.* 2000; *Kirchman et al.* 2000). Nevertheless, each process involved in the bacterial remineralisation of organic carbon could be differently regulated by iron.

Bacterial community composition

It is now generally accepted that iron availability is structuring the phytoplankton community (*Watson* 2001), the iron control on the bacterial community assemblage remains less unclear. In this study, DGGE of PCR-amplified 16S rDNA, realised in the *Thalassiosira gravida* and *Phaeocystis antarctica* re-growth experiments, revealed between 7 and 20 bacterial species in each sample of which 3 species were detected in all bacterial communities.

Iron alone didn't change the bacterial community as observed in the case of *Thalassiosira gravida* ((DOM$_{-Fe}$)+Fe, (TOM$_{-Fe}$)+Fe) experiments. In contrast, the organic matter quantity and/or quality derived from phytoplankton growing in the Fe-enriched and –deplete conditions, structured the bacterial community assemblage. Only 3 (*Thalassiosira gravida* experiment) and 6 (*Phaeocystis antarctica* experiment) bacterial species were similar in both set of re-growth experiments. However, the major variations in the bacterial assemblage were observed for different phytoplanktonic sources of organic matter (*Phaeocystis antarctica* and *Thalassiosira gravida*). Therefore, iron by structuring the phytoplanktonic species and then the organic matter composition, controls the bacterial assemblage.

Our results indicate that long-term bottles (>10 days) mostly measure the activity of few opportunistic bacteria and not that of the original assemblage. Therefore, the effect on iron on the bacterial activities will be investigated in the first 10 days.

<u>Bacterial activities</u>

A significant fraction of individual cells within natural bacterial assemblages is not actively engaged in cellular metabolism (*Smith & del Giorgio*, 2003). Different controlling factors such as temperature, salinity, inorganic and organic substrates have been proposed. The control by iron has not yet been investigated.

The fraction of active individual cells within the bacterial assemblage was measured by two methods. In *Phaeocystis antarctica* and *Chaetoceros dichaeta* re-growth experiments, cell-specific respiration was measured by cyanoditolytetrazolium chloride (CTC) reduction while in *Thalassiosira gravida* re-growth experiment the membrane integrity was investigated with SYTOX stain.
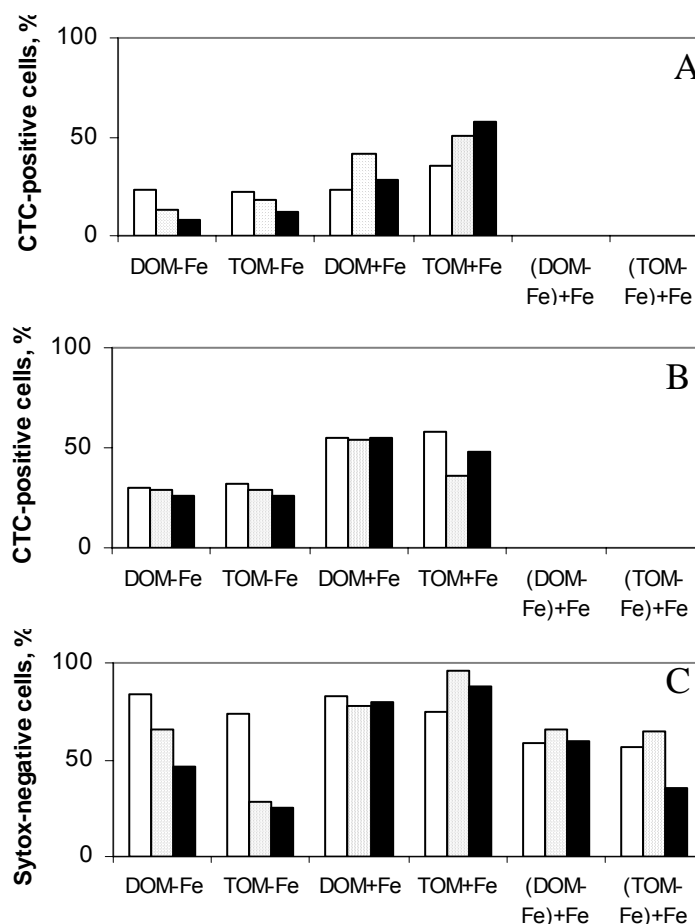
Figure II.23: Viability (CTC-postive and SYTOX-negative cells) in the re-growth experiments; time 0 (white column), time 3-4 days (doted column), time 10 days (black column). A. *Phaeocystis antarctica*-derived organic matter. B. *Chaetoceros dichaeta*-derived organic matter C. *Thalassiosira gravida*-derived organic matter.

As shown in **Figure II.23** the fraction of respiring, CTC-positive, cells ranged between 8 and 58% while the fraction of cells with intact membranes ranged between 28 and 96%. The difference between both physiological activities could possibly result from the fact that although bacteria were respiring, this fraction was too small to be detected by the CTC method, or that bacteria were dying but still had intact membranes.

In all re-growth experiments the fraction of active cells decreased with time under iron-depleted conditions. The organic matter derived from iron-enriched phytoplankton cultures clearly stimulated the cell-specific activities, particularly the fraction of respiring cells (**Figure II.23A,B**). The iron availability nevertheless could be directly controlled the percentage of CTC-positive cell because the majority of the cellular Fe in heterotrophic bacteria is compartmentalised in the respiratory electron chain (*Tortell et al.* 1999). The membrane integrity of bacterial cells seems controlled by two co-factors: the organic matter and iron. Indeed, while iron alone maintained stable the fraction of membrane intact cells (**Figure II.23A,C**; see (DOM-Fe)+Fe and (TOM-Fe)+Fe), the organic matter quantity/quality combined with high iron availability increased this fraction.

Iron seems to have a direct and indirect effect on the proportion of bacterial cells involved in metabolic processes and subsequently in remineralisation of organic matter.

Ectoenzymatic activities

The hydrolysis of organic matter is the first preliminary step in the remineralisation of organic matter, this process is thus crucial in the evaluation of biological carbon pump efficiency. Our study shows that the ectoenzymatic (ectopeptidase and ecto-β-glucosidase) activities increased in response of organic matter enrichment, resulting of iron-enriched conditions (**Figure II.24**; DOM_{-Fe} & TOM_{-Fe}). During the Eisenex iron fertilisation experiment, the highest ectoenzymatic activities were also observed inside the iron patch (*Arrieta et al.* 2004). Nevertheless, iron alone did not stimulate ectoenzymatic activities (**Figure II.24D**; (DOM_{-Fe}) +Fe & (TOM_{-Fe})+Fe). Unexpectedly, very high activities (EPA and EGA) were measured in the presence of TOC in iron-deplete *Phaeocystis* re-growth experiments (**Figure II.24A,C**; TOM-Fe).

Particulate organic matter, operating as chelating agent for iron, can affect the bioavailability of Fe to bacteria under iron-limiting conditions (*Maranger & Pullin* 2003). Under major iron limitation enhanced enzymatic hydrolysis of POM could thus liberate iron chelated onto organic matter.
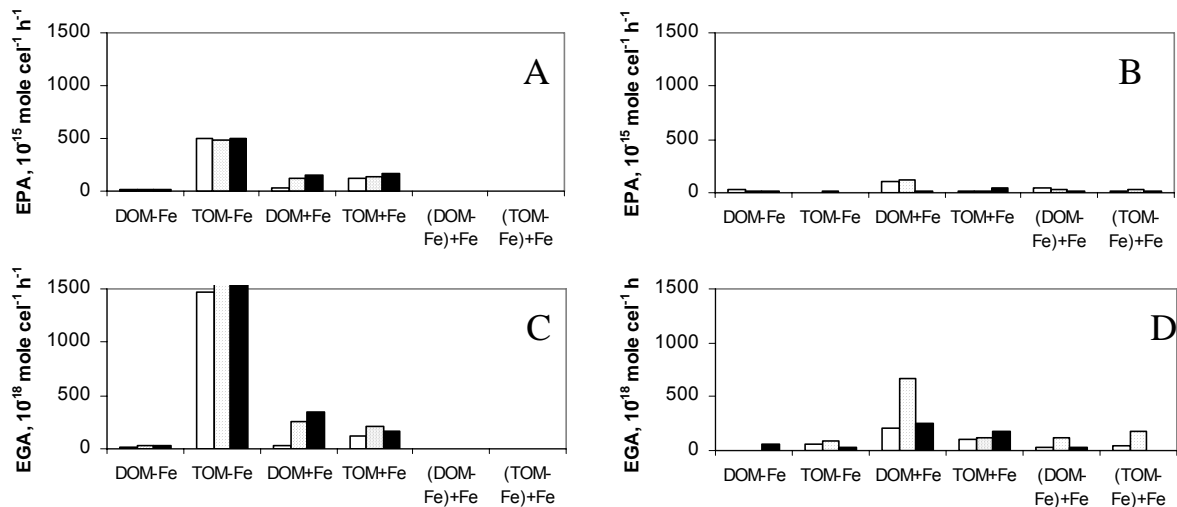
Figure II.24. Ectoenzymatic activities (Ectoprotease activities and ecto-β-glucosidase activities) in the re-growth experiments; time 0 (white column), time 3-4 days (doted column), time 10 days (black column). A & C: *Phaeocystis antarctica*-derived organic matter. B & D: *Thalassiosira gravida*-derived organic matter.

Bacterial growth efficiency:

Quantifying the flux of carbon into the bacterial compartment is dependent on the accuracy with which bacterial growth efficiency (BGE) is assessed. BGE is defined as the ratio of biomass produced to substrate assimilated (*del Giorgio & Cole*, 2000). The environmental factors (e.g. nutrient loading or substrate quality) which control BGE thereby regulate the role of bacterioplankton as a link or sink of carbon in aquatic systems (*Williams*, 2000).

BGE values in natural aquatic systems are generally below 40%, most often between 5 and 30%. In oligotrophic systems, BGE is as low as 10%. Planktonic bacteria appear to maximise carbon utilisation rather than BGE. A consequence of this strategy is that maintenance energy costs (and therefore maintenance respiration) seem to be highest in oligotrophic systems (*del Giorgio & Cole*, 2000). The experiments of *Tortell et al.* (1996) and *Kirchman et al.* (2003) suggest that BGE increases in iron-enriched conditions. Nonetheless, these studies do not allow distinguishing between direct or indirect control by iron. Our study showed that BGE increased in the presence of organic matter derived from iron-enriched cultured phytoplankton. In contrast, under addition of iron alone the measurement of BGE in *Thalassiosira gravida* re-growth experiments (i.e., (DOM-Fe)+Fe and (TOM-Fe)+Fe), BGE was not significantly different from the control experiments (i.e., DOM-Fe and TOM-Fe). BGE was thus indirectly controlled by iron availability.

Table II.6: Bacterial growth efficiency (%) in presence of dissolved (DOM) and total (TOM) organic matter derived from Fe-deplete (M-Fe) and –enriched (M+Fe) phytoplankton cultures (*Phaeocystis antarctica*, *Chaetoceros dichaeta* and *Thalassiosira gravida*) and from Fe-depleted phytoplankton culture (*Thalassiosira gravida*) but inoculated with $FeCl_3$ ((M_{-Fe})+Fe).

	Phaeocystis antarctica		*Chaetoceros dichaeta*		*Thalassiosira gravida*		
	M_{-Fe}	M_{+Fe}	M_{-Fe}	M_{+Fe}	M_{-Fe}	M_{+Fe}	(M_{-Fe})+Fe
DOM	n.s.	29	7	17	n.s.	8	n.s.
TOM	25	30	12	15	n.s.	10	n.s.

Bacterial growth rates

The bacterial growth rates in the presence of organic matter derived from the iron-enriched phytoplankton culture were on average 235 % higher than growth rates in Fe-deplete conditions. Yet, this increase was not observed in the presence of iron alone. These results are similar to those reported by *Church et al.* (2000), who show that bacteria are limited in the first place by organic carbon concentration and in the second place by iron availability.

Interestingly, the specific growth rates estimated from the CTC-positive cells were in the same range, whether organic matter was derived from iron-enriched or iron-deplete conditions (*Phaeocystis antarctica* and *Chaetoceros gravida* re-growth experiments), suggesting an actively growing sub-population of bacteria especially adapted to iron-depleted conditions.
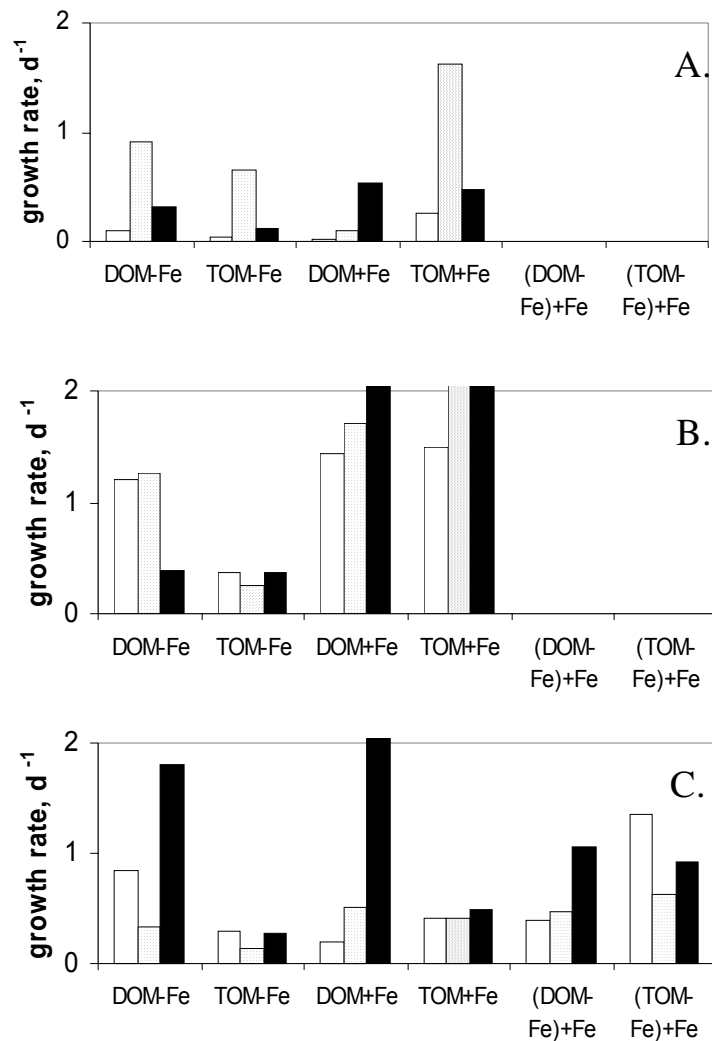
Figure II.25: Bacterial growth rate (d^{-1}) in the re-growth experiments (Time 0 (white column), time 3-4 days (doted column), time 10 days (black column)). A. *Phaeocystis antarctica*-derived organic matter. B. *Chaetoceros dichaeta*-derived organic matter C. *Thalassiosira gravida*-derived organic matter.

3. Iron role on organic matter remineralisation and carbon biological pump efficiency.

Our results suggested that the bacterioplankton activities were mainly controlled by the organic matter quantity/quality as a consequence of Fe-enhanced phytoplankton production. The control by iron on the bacterioplankton remineralisation was indirect. Due to these high bacterial ectoenzymatic activities and growth rates, the contribution of biodegradable organic carbon (BOC_{30days}) into total organic carbon was enhanced in iron-enriched phytoplankton cultures (**Table II.7**). Moreover, it can be observed that the total organic carbon was more

biodegradable than the dissolved organic carbon. This increase of the BDOC contribution into total organic carbon around 1.4 was however less significant than expected from the growth rates, which increased by a factor about 2.4. Indeed, the quantity of remineralised organic carbon in Fe-enriched conditions by bacteria cell produced was reduced due to increase of bacterial growth efficiency. The link between organic carbon and bacterial biomass was more efficient in iron-enriched conditions.

Table II.7: The contribution (after 30 days) of biodegradable dissolved (DOC) and total (TOC) organic carbon to total organic carbon (%) derived from Fe-deplete (M_{-Fe}) and Fe-enriched (M_{+Fe}) phytoplankton cultures.

	Phaeocystis antarctica		*Chaetoceros dichaeta*		*Thalassiosira gravida*	
	M_{-Fe}	M_{+Fe}	M_{-Fe}	M_{+Fe}	M_{-Fe}	M_{+Fe}
DOC	12	25	15	20	n.s.	5
TOC	47	64	45	52	n.s.	5

Finally, a major question concerns the impact of bacterial limitation by iron on efficiency of the the Southern Ocean carbon pump. In iron-limited systems, phytoplankton productivity is limited and dominated by small species. Export of particulate organic matter from the surface waters is minimal and DOM accumulation is not observed. In spite of the fact that bacterial processes are indirectly limited by iron, ratios of bacterial carbon demand over primary production are high (*Cochlan, 2002; Hall & Safi,* 2001) due to strong microzooplankton control on nanophytoplankton. Bacterial growth efficiency is limited by iron availability and consumed carbon by the bacteria is largely respired. As a result, the efficiency of the biological carbon pump is reduced.

An iron pulse induces a shift from recycling microbial food web to large blooming phytoplankton. Bloom-forming species are 'grazer-resistant' large phytoplankton (>20μm) subject to carbon export due to their significant sinking rate and their ability to form chains, colonies and/or aggregates. At the decline of phytoplankton bloom, DOC accumulation can be observed as a consequence of phytoplanktonic lysis due to nutrient and then iron limitation. As suggested by our experiments, the bacterial activities are not directly reduced by iron availability and the dissolved organic carbon is therefore remineralised through the microbial loop. Remineralisation of the DOC prior to overturning circulation prevents it from making a

major contribution to export in the Southern Ocean. As an illustration, in the Ross Sea, DOC concentrations increase by 15-30µM where the blooms of *Phaeocystis* and diatoms are particularly strong (*Hansell & Carlson,* 2001). The bacterial remineralisation up to the fall reduced the mean DOC concentrations to less than 5 µM, above background. The vertical export of DOC in this system represented only 2% of the total annual export of total organic carbon. In the iron-enriched systems, the bacterial carbon demand/ primary production ratios were low in the euphotic depth (*Cochlan* 2001; *Hall & Safi* 2001). A large part of primary production is directly exported by aggregation and settling. While we know from sediment trap data that particle flux decrease rapidly with the depth between euphotic depth and 500-1000m, we have little knowledge of the processes that control this remineralisation. Bacterial decompostion but also zooplankton consumption and chemical dissolution are all likely to alter the efficiency of the biological pump (*Ducklow et al.* 2001).

III. MODELING CLIMATE VARIABILITY AND CHANGE IN THE SOUTHERN OCEAN

III.1. Recent and future climate changes

The transient response of coupled atmosphere-ocean models to an increase in the atmospheric concentration of greenhouse gases is generally stronger at the surface in the Northern Hemisphere than in the Southern Hemisphere. This asymmetry is generally attributed to the higher fraction of the area covered by ocean in the Southern Hemisphere that induces a higher thermal inertia there. Using the low resolution atmospheric-sea-ice-ocean model ECBILT-CLIO, we have shown that the response of the Southern Ocean to an increase in atmospheric greenhouse gas concentrations can actually be decomposed in two different phases (*Goosse and Renssen*, 2001). Firstly, the ocean indeed damps the surface warming because of its large heat capacity. Secondly, one century after the major increase in greenhouse gases, the warming is amplified because of a positive feedback that is associated with a stronger oceanic meridional heat transport toward the Southern Ocean. Consequently, the long-term decrease in ice area in the Southern Ocean is much larger than in the Northern Hemisphere.

In order to test this hypothesis, a suite of simulations have been performed with ECBILT-CLIO driven by natural and anthropogenic forcings covering the period 1000-2000 AD. Model results have first been successfully compared to observations and proxy evidence of past changes in the Southern Ocean (*Goosse et al*, 2004; *Goosse and Renssen*, 2005). Over the last 250 years, the ice area has decreased by about 1×10^6 m^2 in annual mean. A comparison with experiments driven by only natural forcings suggests that this reduction is due to both natural and anthropogenic forcing, the latter playing a larger role than natural forcing over the last 150 years. Despite this contribution from anthropogenic forcing, the simulated ice area at the end of the 20th Century is similar to the one simulated during the 14th Century because of the slow response of the Southern ocean to radiative forcing (**Figure III.1**). This slow response of the Southern Ocean is perfectly consistent with the simulation of future changes described above. Furthermore, sensitivity experiments performed with the model show that the model initial conditions have a large influence on the simulate ice cover and that it is necessary to start simulations at least two centuries before the period of interest in order to remove this influence.

Time (yr AD)
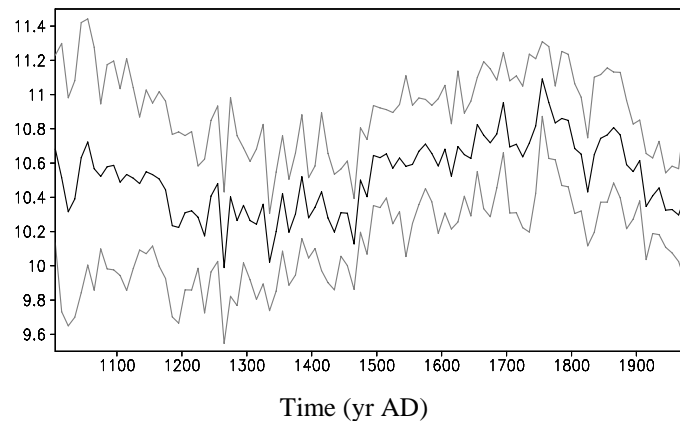
Figure III.1: Annual mean ice area in the Southern Hemisphere (in 10^6 km^2) during the last 1000 years averaged over 10 simulations performed with ECBILT-CLIO that differ only in their initial conditions (black solid) The mean over the ensemble of 10 simulations plus one and minus one standard deviation of the ensemble are in grey (measuring the uncertainty associated with the internal variability of the system). Data were grouped as 10-year long averages.

Recently, outputs from simulations performed with current atmosphere-ocean general circulation models for the Fourth Assessment Report of Intergovernmental Panel on Climate Change (IPCC AR4) have been used to investigate the evolution of sea ice over the 20th and 21st centuries (*Arzel et al.* 2005). We first use the results from the "Climate of the 20th Century Experiment" to assess the ability of these models to reproduce the observed sea ice cover changes over the period 1981-2000. The projected sea ice changes over the 21st century in response to the IPCC Special Report on Emission Scenarios A1B have been then examined. Overall, there is a large uncertainty in simulating the present-day sea ice coverage and thickness and in predicting sea ice changes in both hemispheres. Over the period 1981-2000, we find that the multimodel average sea ice extent agrees reasonably well with observations in the Northern Hemisphere despite the wide range of model responses but larger uncertainties appear in the Southern Hemisphere. The climate change projections over the 21st century reveal that the amplitude of the seasonal cycle of sea ice extent increases in a warming climate and the annual mean sea ice extent decreases at similar rates in both hemispheres.

In particular, we have examined the geographical distribution of the projected sea ice cover averaged over 2081-2100. The multimodel average sea ice cover responses over 2081-2100 are illustrated in **Figure III.2**. This figure has been constructed following *Flato* (2004) and displays the fraction of the model population

that have ice at a given grid point. The observed sea ice edge averaged over 1981-2000 from the HadISST dataset (thick, black line, *Rayner et al.* 2003) is represented for comparison. Overall, the most noticeable difference with the average ice climatology over 1981-2000 is that the area in which more than 90% of the model population have ice has totally disappeared in summer. By contrast, during wintertime, this area has decreased less (about -40% in the Southern Hemisphere). These results suggest that under the considered warming scenario, ice can survive in winter because temperatures are still cold enough in polar regions. Indeed, the simulated median sea ice edge in late winter averaged over 2081-2100 is not very far from the observed one averaged over 1981-2000, except in the Atlantic sector of the Southern Ocean.
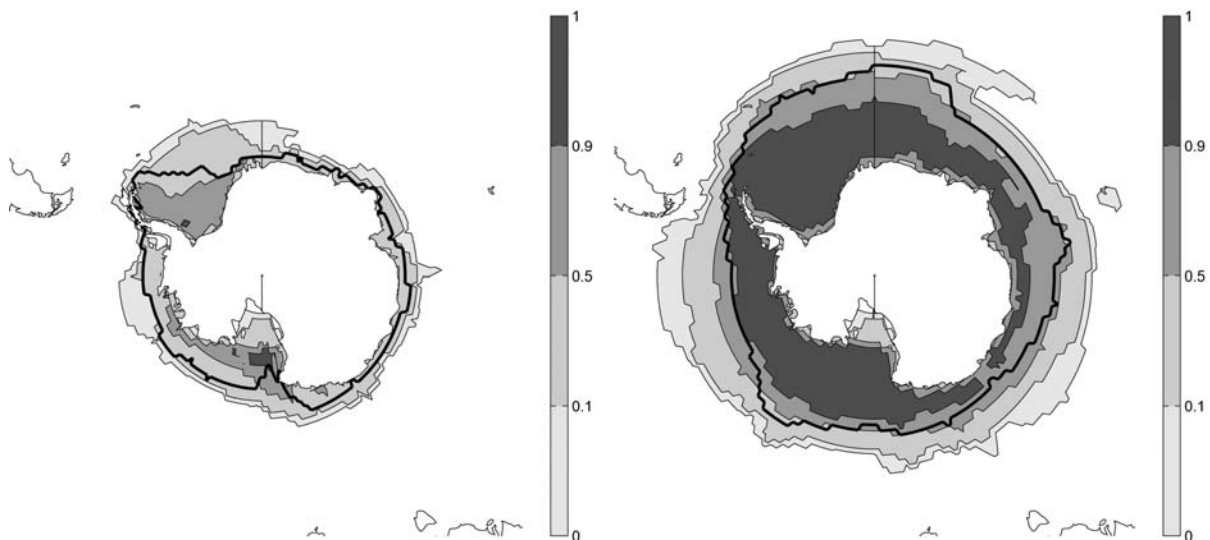
Figure III.2:. Percentage (%) of climate models which have ice on average over the period 2081-2100 (experiments A1B) in March (left) and September (right). The analysis is based on 10 models (for a complete list see *Arzel et al.* 2005) For comparison, the thick black line represents the observed sea ice edge averaged over 1981-2000, derived from the HadISSR dataset (*Rayner et al.,* 2003).

III.2. Modelling the ice-ocean system

In order to study the ice-ocean system in the Southern Ocean, the model ORCA2-LIM is used. It results from the coupling of the Louvain-la-Neuve sea ice model (LIM) (*Fichefet and Morales Maqueda*, 1997) with the hydrostatic, primitive equation ocean model OPA (Océan PArallélisé) (*Madec et al.*, 1999). OPA is a finite difference ocean general circulation model with a free surface and a non-linear

equation of state in the *Jackett and McDougall* (1995) formulation. In the ORCA2-LIM configuration, lateral tracer mixing is done along isopycnals. Eddy-induced tracer advection is parameterized following *Gent and McWilliams* (1990) with the coefficients decreased between 20°N and 20°S. Momentum is mixed along model level surfaces using coefficients varying with latitude, longitude and depth. Vertical eddy diffusivity and viscosity coefficients are computed from a level-1.5 turbulence closure scheme based on a prognostic equation for the turbulent kinetic energy (*Blanke and Delecluse*, 1993). Double diffusive mixing (i.e. salt fingering and diffusive layering) is computed following *Merryfield et al.* (1999). In locations with a statically unstable stratification, a value of 100 m^2 s^{-1} is assigned to the vertical eddy coefficients for momentum and tracers. The *Beckmann and Döscher* (1997) bottom boundary layer scheme ensures an improved representation of dense water spreading over topography in this geopotential-coordinate model.

The thermodynamic part of LIM uses a three-layer model (one layer for snow and two layers for ice) for sensible heat storage and vertical heat conduction within snow and ice. Vertical and lateral sea ice growth/decay rates are obtained from energy budgets at the upper and lower surfaces of the snow-ice cover, and at the surface of leads present within the ice pack. At the upper surface, a prognostic treatment of the temperature in a very thin surface layer is used. The effect of the subgrid-scale snow and ice thickness distributions is accounted for through an effective thermal conductivity, which is computed by assuming that the snow and ice thicknesses are uniformly distributed between zero and twice their mean value over the ice-covered portion of the grid cell. Storage of latent heat inside the ice resulting from the trapping of shortwave radiation by brine pockets is taken into account. When the load of snow is large enough to depress the snow-ice interface under the water level, seawater is assumed to infiltrate the entirety of the submerged snow and to freeze there, forming a snow ice cap. The ice concentration, the snow volume per unit area, the ice volume per unit area, the snow enthalpy per unit area, the ice enthalpy per unit area, and the brine reservoir per unit area are advected with the ice drift velocity.

The sea ice velocity field is determined from a momentum balance considering sea ice as a two-dimensional continuum in dynamical interaction with atmosphere and ocean. The viscous-plastic constitutive law proposed by *Hibler* (1979) is used for computing internal stress within the ice for different states of deformation.

In the configuration used in this section and the following one, the model is run on a global grid with 2° nominal resolution and a mesh refinement in high latitudes and near the equator. As a consequence, the meridional resolution increases to 0.5° close to the Antarctic continent, corresponding to a horizontal grid width of ~50 km. Vertical discretization uses 30 z-levels, with 10 levels in the top 100 m.

Daily 2-m air temperatures and 10-m winds from the NCEP/NCAR reanalysis project for the period 1948–1999 (*Kalnay et al.,* 1996), and monthly climatologies of surface relative humidity (*Trenberth et al.,* 1989), cloud fraction (*Berliand and Strokina,* 1980), and precipitation rate (*Xie and Arkin,* 1996) are utilized to drive the model. The surface fluxes of heat and moisture are determined from these data by using empirical parameterizations described by *Goosse* (1997). Evaporation/sublimation is derived from the turbulent flux of latent heat. In addition, a correction of ocean surface freshwater fluxes has been derived from the time-mean restoring salinity flux diagnosed from the experiment described by *Timmermann et al.* (2004a) in order to circumvent the surface salinity drift that occurs through the lack of any stabilizing feedback if the model is forced with slightly incorrect evaporation, precipitation and/or river runoff fields. The momentum fluxes at the various interfaces are obtained from standard bulk formulas. The parameterization of *Large and Pond* (1981) is utilized to compute the drag coefficient between air and water. For the drag coefficients between air and snow/ice and between ice and water, we use constant values of 2.25×10^{-3} and 5×10^{-3}, respectively. This leads to a ratio of these two coefficients of 0.45, which is consistent with values adopted in other modelling studies of the Antarctic sea ice (e.g., *Stössel,* 1992; *Fischer and Lemke,* 1994; *Harder and Fischer,* 1999). Further details of the coupled model are given by *Timmermann et al.* (2004; 2005).
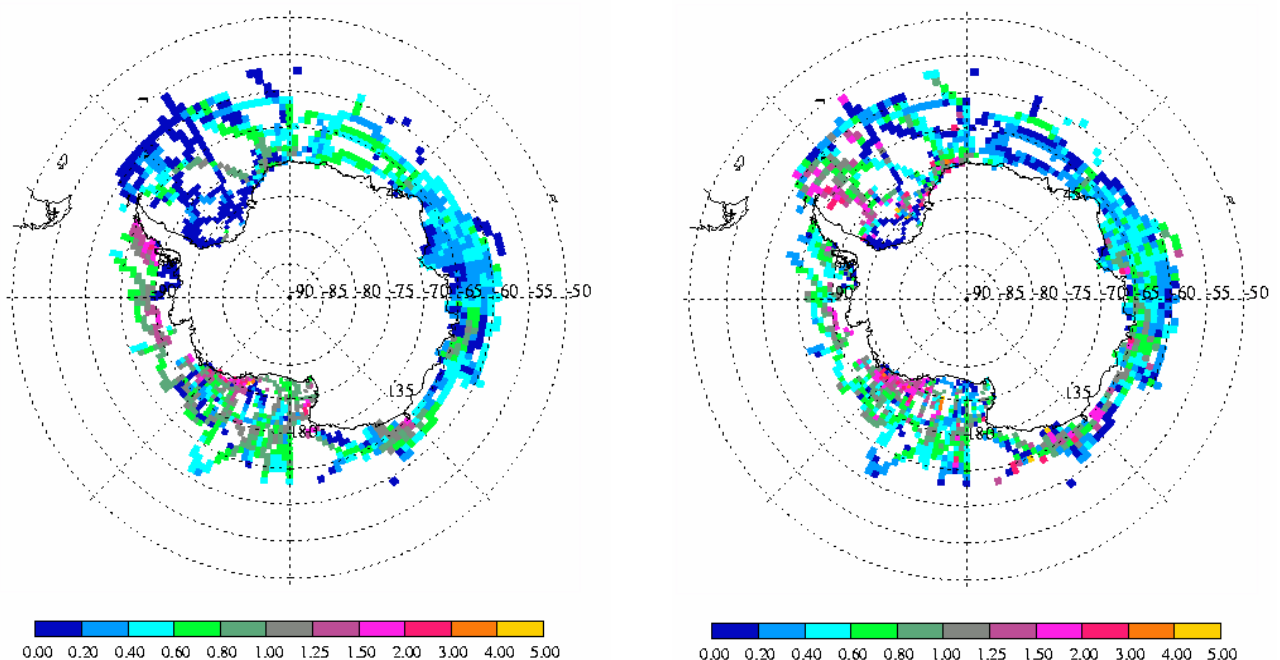
Figure III.3: Composite means of (left) the simulated sea-ice thickness in ORCA-LIM sampled at the same time and location as the observed one (m) and (right) the observed ice thickness.

The coupled model provides reasonable results as discussed in *Timmermann et al.* (2005). In particular, the simulated sea ice thickness has been compared with thicknesses from the Antarctic Sea Ice Processes and Climate (ASPeCT) database in *Timmermann et al.* (2004). We find a qualitative agreement of the large-scale patterns of ice thickness distribution (**Figure III.3**). Regional averages for the various sectors of the Southern Ocean yield a very good correspondence between observations and model data. Exceptions are the eastern Bellingshausen Sea and northwestern Weddell Sea. A poor representation of the Antarctic Peninsula in the atmospheric forcing data and the related overestimation of westerly winds in this region lead to a spurious accumulation of sea ice on the western side of the peninsula and to an underestimation of sea ice coverage on the eastern side. Since the spatial scale of observations is not comparable to the size of a model grid cell, there is little agreement between individual observations and the corresponding model ice thicknesses. A model analysis of the seasonal and interannual variability indicates that the ASPeCt data underestimate the climatological ice thickness in the central and southern Weddell Sea and the eastern Ross Sea by up to 1 m. Because of a winter bias in the observations an overestimation of similar magnitude is expected in the Bellingshausen Sea. Ice thickness data in most of the Indo-Pacific sector appear to be representative for the long-term climatology. A model estimate of the bias has been used to compute a revised distribution of climatological sea ice thickness.

III.3. Influence of the Southern Annular Mode on the sea ice–ocean system

First of all we have used the ORCA2-LIM model to confirm previous results showing that the Southern Annular Mode (SAM) has a clear and strong impact on the structure of ocean currents over large parts of the water column in the Southern Ocean. At the surface, transport anomalies associated with a positive phase of SAM are directed towards the northwest at high latitudes (south of 45°S) inducing an upwelling that features a maximum around 65°S and a downwelling at about 45°S. Due to continuity, this is balanced by a southward return flow below 1500 m. Furthermore, the enhanced wind during years with positive SAM index implies a stronger stirring of the water column and a deeper mixed layer during all seasons. The latter and the modification in the intensity of the upwelling, which have both an impact on the availability of nutrients in the upper ocean, might well affect the biological production in the Southern Ocean.

The impact of the SAM on the ocean surface temperature or on the ice-covered area varies strongly for the different regions of the Southern Ocean. Because of a low pressure anomaly in the Amundsen-Bellingshausen sector during

positive SAM years, the Weddell and Bellingshausen Seas are subject to more northerly winds, while the Ross Sea tends to have more southerly winds. This induces a cooling at the surface and an increase in the ice-covered area in the Ross and Amundsen Seas during years with positive SAM index while, at the same time, the SST increases and the ice-covered area decreases in the Weddell Sea. In summary, our results indicate that the main response of the ice concentration to the SAM is a dipole between the Weddell and the Ross Seas with a decrease of ice in the Weddell sector, and an increase in the Amundsen sector and parts of the Pacific sector for years with a positive SAM index. Integrated over the Southern Ocean, these regional differences tend to cancel out, so that signals in the zonally integrated SST and ice concentration are very small.

Those conclusions are statistically significant and in good agreement with observations, and with previous investigations (*Kwok and Comiso*, 2002; *Liu et al.*, 2004). This suggests that, despite the errors in the NCEP-NCAR data set and although the forcing used to drive our simulation does not include interannual variability of cloud cover, precipitation and relative humidity, we are able to capture, at least qualitatively, the main characteristics of the response of the sea ice–ocean system to the SAM.

Our results also indicate that the recent changes in ice-covered area in the Southern Ocean cannot be attributed to the general increase in the SAM index during the last 20 years. Indeed, an increase in SAM index would imply a less extensive ice cover in the Weddell Sea and a larger area of ice in the Ross Sea. For the Ross Sea, this is consistent with observation of the trend performed by *Zwally et al.* (2002), but not for the Weddell Sea. We conclude that the trend observed in the sea ice coverage by Zwally et al. (2002) cannot be attributed to the long-term trend of the SAM index. This clearly illustrates that the behavior of the ice cover in the Southern Ocean is a complex phenomena and understanding its evolution needs to take into account all the factors that could affect it (e.g., *Yuan and Martinson,* 1997; *Kwok and Comiso,* 2002; *Van den Broeke,* 2000).

The large regional differences in the response of the Southern Ocean to the SAM may appear strange in the context of an annular mode. Nevertheless, a zonal asymmetry of the temperature pattern can easily be attributed to the non-symmetric land distribution, even with purely zonal winds as argued by *Thompson and Solomon* (2002) to explain the temperature changes over the Antarctic Peninsula. Furthermore, despite its name, the definition of the SAM does not impose that it is strictly an annular phenomenon; the meridional components of the wind appear to play an important role in controlling the ice cover, in particular the low pressure anomaly over the Bellingshausen-Amundsen Seas during years with positive SAM index.

We have also used the same sea ice-ocean model driven by a standard forcing for the year 1980-1999 plus an idealized anomaly based on the regression of the NCEP-NCAR reanalysis data onto SAM. In order to extract the role of the wind stress and the air temperature forcing associated to SAM, we have made a series of runs, some with only the mechanical part of the anomaly of the forcing, others with only the thermal part of the idealized anomaly. We have seen that the thermal part (air temperature) resulted in more ice, when the SAM index is positive because of the lower air temperature, mainly in autumn and winter, except in the Weddell Sea and around the Peninsula where the warmer air temperature is responsible for the decreased ice concentration.

The response to the mechanical forcing (wind stress) can be decomposed in different terms. The first one is related to changes in ice velocities, which is largely due to the non-annular part of the mechanical forcing. This is responsible for a decrease in winter sea ice concentration and thickness east of the Antarctic Peninsula. It is also responsible for the increase in ice area in the Ross Sea as it pushes ice away of the continent. A second part of the response is induced by the higher upward oceanic velocities close to the Antarctic continent due to an increased Ekman pumping when SAM is high. As a result, warmer water rises and the ice melts. This effect can be seen in the Indian, the Pacific, the Ross and the Amundsen-Bellingshausen Sector. Another effect of this pumping is the rise in surface salinity in Weddell which destabilises the water column. The result is an increased mixing layer depth and a lesser ice area. As a consequence, the mechanical forcing has not only an effect on the ice extent but also on the currents (northward surface currents and southward deeper in the ocean, pumping close to the continent, downwelling around 40°S) and on the mixed layer depth (increase mixed layer depth due to increased wind stirring) and the salinity.

The response to the SAM forcing can be explained as the sum of the responses to the distinct mechanical and thermal forcings. The combination of the two gives a dipole in winter, with less ice in the Weddell Sector and more ice in the Ross Sector (**Figure III.4**). The Eastern Bellingshausen Sector follows the Weddell Sector, whereas the Western Amundsen Sector has a similar behaviour as the Ross Sector. In the other sectors, the decreases in sea ice concentration due to the enhanced pumping in the winter sea ice concentration are compensated by the increases due to the lower air temperatures. These changes are all in good agreement with the observations and with our previous experiments (*Lefebvre et al*, 2004) (**Figure III.4**).
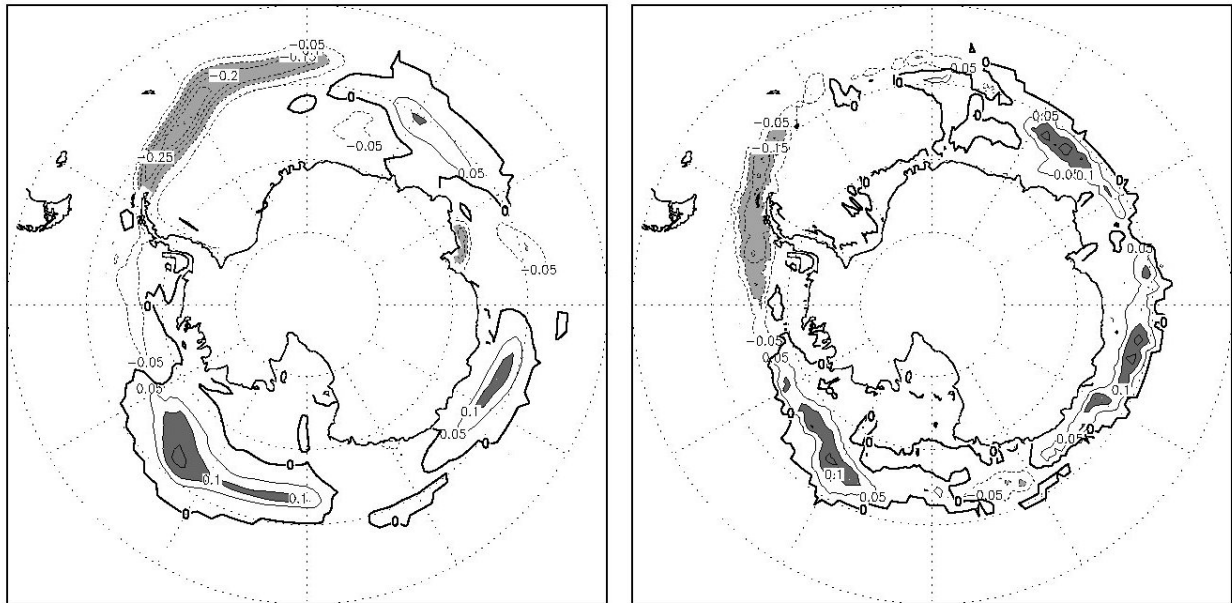
Figure III.4: (left) The difference in sea ice concentration at the end of July due to SAM simulated in idealized simulations performed with ORCA-LIM. (right) Regression between the seasonal mean SAM index and the July mean ice concentration for the period 1980-1999 in the HadISST1 (*Rayner et al.,* 2003) observations. Contour interval is 0.05. Solid lines are positive values, while dotted lines show negative values. Shading in dark gray means a value of more than 0.1, whereas shading in light gray shows a value of less than –0.1.

When integrated over the different sectors (**Table III.1**), we see that the decrease in ice extent in the Weddell Sea and the increase in the Ross Sea is noticed in nearly all the runs. For those two areas, the thermal and mechanical effects tend thus to reinforce each other. On the other hand, mechanical and thermal forcings tend to have opposite responses in the other sectors, resulting in weaker total changes. The responses to the thermal and mechanical forcing have more or less the same amplitude. This shows that despite the low correlation between the SAM index and the air temperature, the thermal forcing could by no means be neglected. This is due on the one hand to the large variability of the air temperature in the polar areas (low correlations are thus not associated with small temperature changes) and on the other hand to the strong impact of temperature changes on the ice cover.

Table III.1 also illustrates that integrated over the whole Southern Ocean, the thermal forcing induces an increase in the ice extent, while the mechanical forcing is responsible for a decrease of the ice extent. The latter is mainly due to the annular

part of the forcing since the non-annular part is associated with an increase of the ice extent. Overall, SAM is associated with an decrease of the ice extent in winter in our simulations. Nevertheless, the complexity of the geographical distribution of the response and of the mechanisms involved with compensating effect of thermal and mechanical forcing imply that any long term influence of SAM on the ice extent integrated over the Southern Hemisphere is very difficult to estimate from the available information.

Table III.1: Ice area winter (JAS) differences between the different simulations in 1.000.000 km^2. T: Role of the Thermal Forcing. M: Role of the Mechanical Forcing. Ann: Role of the Annular Mechanical Forcing. NA: Role of the Non-Annular Mechanical Forcing. S: Role of the Total Forcing. The division in sectors is as follows: Weddell Sea (60°W-20°E), Indian Ocean (20°E-90°E), Pacific Ocean (90°E-160°E), Ross Sea (160°E-140°W) and the Amundsen-Bellingshausen Seas (140°W-60°W).

	Weddell	Indian	Pacific	Ross	Amundsen-Bellingshausen	Total
T	-0.035	0.136	0.117	0.091	0.030	0.339
M	-0.326	-0.118	-0.071	0.035	-0.051	-0.530
Ann	-0.219	-0.089	-0.029	-0.015	-0.052	-0.403
NA	0.058	0.098	0.029	0.078	0.015	0.279
S	-0.382	-0.020	0.034	0.110	-0.010	-0.269

IV. MODELING AIR-TO-SEA CO$_2$ EXCHANGES

IV.1 The idealized SWAMCO-4 biogeochemical model: linking biogeochemical cycles and ecosystem structure and function

The estimate of the role of the ocean in global carbon cycling and its response to or influence on climate change needs a proper description of blooming phytoplankton species and the related trophic bifurcations, most notably the shift from the C-retaining microbial network towards the C-exporting linear food chain, under the multiple control of light, nutrients and biology such as grazing pressure and cell lysis. The most recent models of ocean carbon cycling set up to predict biotic responses to climate change (e.g. *Aumont et al.*, 2003; *Moore et al.*, 2002) include explicit or implicit description of these vital ecosystem processes. Yet some of these representations are very crude or empiric and lack mechanistic understanding. As a first step to improve the mechanistic representation of ocean biogeochemical processes in global ocean models we developed the complex ecological model SWAMCO-4. This model (**Figure IV.1**) explicitly describes the cyclying of C, N, P, Si and Fe and incorporates the processes directing the structure of the planktonic system composed of four taxonomic phytoplankton groups and their forcing functions. SWAMCO-4 results of the extension of ecosystem model SWAMCO [Sea WAter Microbial Community model of *Lancelot et al.* (2000) modified as in *Hannon et al.* (2001) for consideration of air-sea CO$_2$ exchanges] based on 2 taxonomic phytoplankton groups (diatoms and pico/nano phytoplankton), with two key phytoplankton taxons considered as important players in the biogeochemical cycles in different provinces of the Southern ocean and feedbacks to atmospheric CO$_2$. These are the worldwide-distributed colony-forming *Phaeocystis spp* and the calcified coccolithophorids with *Emiliana huxleyi* as main representative. The SWAMCO-4 parameterisations are based on physiological principles and were estimated from independent targeted process-level studies performed under field and/or laboratory conditions over the last 20 yr (*Lancelot et.*,1991, 2000, *Timmermans et al.* 2001, 2004), and on a review of literature on diatom (*Sarthou et al.*, 2005), *Phaeocystis* (Schoemann et al. 2005) and coccolithophoridae (Paasche, 2000) ecophysiology. Taxon-specific parameters are summarized in **Table IV.1**.
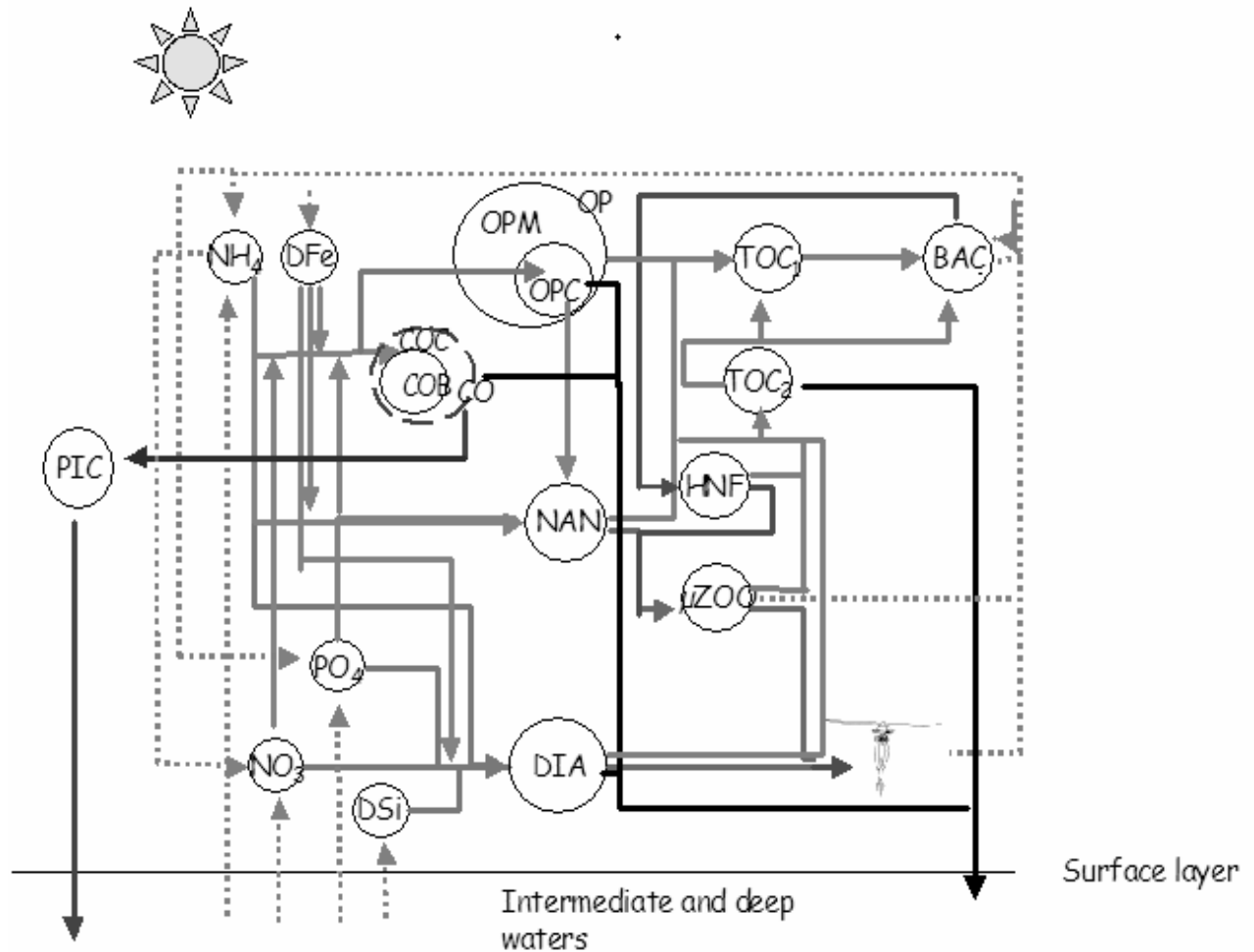
Figure IV.1: Diagrammatic structure of the ecosystem model SWAMCO-4. Processes (arrows) and state variables (circles). NH_4: ammonium; NO_3: nitrate; PO_4: phosphate; DSi: dissolved silica, DIA: diatom; NAN: nanophytoflagellate; OP, OPC, OPM: *Phaeocystis* colony, cell, colony polysaccharide matrix; CO, COB, COC: Coccolithophorid cell, biomass, attached coccoliths; PIC: COC+detached liths; TOCi: fast (i=1) and slowly (i=2) biodegradable organic matter; BAC: bacteria; HNF: heterotrophic nanoflagellate; μZOO: microzooplankton.

Table IV.1: Taxon-specific parameters in SWAMCO-4 (*Pasquer et al.*, in revision)

| Parameter	DIA	NAN	CO	OP
Growth				
Max gwth, h^{-1}	0.06	0.06	0.065	0.06
Max photo, h^{-1}	0.12	0.1	0.08	0.22
Photo.efficiency, $\mu mole\ m^{-2}s^{-1}h^{-1}$	0.0008	0.0011	0.0001	variable
Add. Energy cost	no	no	calcification	no
Iron limitation of max photo.	$\dfrac{0.75*DFe}{K_{Fe}+DFe}+0.25$	$\tanh(5*DFe)^{2.5}$		
Photo. efficiency		$\tanh(10*DFe)$		
Optimal T, °C	7.3	16.5	22	15.5
ΔT, °C	5.3	13	9	14
Nutrient uptake and stoichiometry				
K_N, mmol m^{-3}	1	1	0.2	2
K_P, mmol m^{-3}	0.1	0.1	10^{-3}	10^{-4}
K_{Si}, mmol m^{-3}	0.4			
K_{Fe}, mmol m^{-3}	micro: $6.4\ 10^{-4}$ nano: 10^{-4}	$3\ 10^{-4}$	$3\ 10^{-4}$	$1.5\ 10^{-3}$
Fe:C, mmol:mol	0.04	0.04	0.04	Cell: 0.04 Mucus: 0.08
Si:C	$-0.39*DFe+1.52$			
N:P	16	16	16	Cell:16
Losses				
grazing				
mesozoo	Hannon et al., 2001	N	N	N
microzoo	N	Lancelot et al.,2000	Pasquer et al.,in revision	After col. disruption
Autolysis	Lancelot et al 2000			
Aggregation	Y	N	Y	After col. disruption

IV.2 Testing 1D-SWAMCO-4 in the ice-free and marginal ice zone of the Southern Ocean

Implementation - The performance of SWAMCO-4 was evaluated in the 1D vertical physical frame throughout its cross application at positions of time-serie stations characterized by contrasted key species dominance (*Longhurst*, 1998), export production (*Schlitzer*, 2002), CO_2 air-sea fluxes (*Takahashi et al.*, 2002 revised in http://www.ldeo.columbia.edu/res/pi/CO2/) and where biogeochemical data are available for model initialisation and comparison of results. The following two JGOFS sites were chosen: the ice-free Southern Ocean Time Series station KERFIX (50°40S, 68°E) for the period 1993-2002 and the sea-ice associated Ross Sea domain (station S; 76°S, 180°W) of the Antarctic Environment and Southern Ocean Process Study AESOPS. The 1D vertical physical model was derived from the 3D CLIO (Coupled Large-scale Ice Ocean) model of *Goosse et al.* (2000). Input fields consist of daily surface air temperatures and winds from the NCEP–NCAR reanalysis project for the period 1993–2002 (*Kalnay et al.*, 1996) as well as climatological monthly surface relative humidities (*Trenberth et al.*, 1989), cloud fractions (*Berliand and Strokina*, 1980), and precipitation rates (*Xie and Arkin*, 1996). Atmospheric input of bioreactive Fe is deduced from modelled fluxes reported by *Lefevre and Watson* (1999). For the Antarctic region in particular, a daily atmospheric input of bioreactive iron of 0.5 nmole m^{-2} d^{-1} (*Lefevre and Watson*, 1999) was assumed to be accumulated in the ice during Austral winter and released in the surface layer at the time of ice-melting.

For each investigated area, simulations were carried out up to year 2002 after a 4 years spin-up run with first year conditions (KERFIX: 1993; AESOPS: 1996). Nutrients, DFe, dissolved inorganic carbon (DIC), and Chl a initial winter conditions were retrieved from the JGOFS database (http://usjgofs.whoi.edu/jg/dir/jgofs/). When not measured DFe was extracted from the recently published compilation of iron data (*de Baar and de Jong*, 2001). Atmospheric CO_2 concentration was set at 352 ppm in 1991 and an annual increase of 1.2 ppm was considered (*Conway et al.*, 1994).

Validation - The prediction capability of 1D-SWAMCO-4 can be appraised on **Figure IV.2 and Table IV.2**

Figure IV.2 compares the annual simulation of sea surface temperature (SST), DFe, total phytoplankton (Chl *a*), the dominant phytoplankton group (diatom, *Phaeocystis* colonies) and the surface water CO_2 fugacity (fCO_2) obtained at KERFIX (**Fig.IV.2** left pannel) and in the Ross Sea (**Fig.IV.2** left pannel) locations. As a general trend, 1D-SWAMCO-4 reproduces reasonably well the order of magnitude of observed spring-summer maxima of phytoplankton biomass and associated dominant phytoplankton group. The maximum Chl *a* reached is positively linked to the maxima of winter DFe. For the SWAMCO-4 application in the Ross Sea, the snow/ice accumulation over the Austral winter of iron from above was found crucial to explain the elevated surface concentration of DFe (up to 8 nM) often observed at the time of ice melting (*Sedwick and Di Tullio*, 1997). In our simulations this process is responsible for the sudden increase of DFe (from 0.2 to 10 µmole m^{-3}) simulated by SWAMCO-4 in November 1996. A significant undersaturation of surface water CO_2 is simulated in summer and coincides with the time of diatom (KERFIX) of *Phaeocystis* (Ross Sea) bloom decline (Fig. IV.2).

SWAMCO-4 annual primary production, carbon export production at 100m and air-sea CO_2 fluxes at 2 JGOFS site locations (**Table IV.2**) compare fairly well with the few existing data. Predicted export production varies by a factor 2 being the lowest at KERFIX and the highest in the Ross Sea. Interestingly enough, export production at the latter location represents a low (25%) fraction of primary production in comparison with KERFIX (55%) giving support to the currently admitted assumption that *Phaeocystis* colony production contributes less to the vertical flux of particles to the deep ocean when compared to diatom production. On an annual mean an atmospheric CO_2 sink is predicted at the two test locations (**Table IV.2**). These numbers are in fairly good agreement with revised estimates by Takahashi et al. (**Table IV.2**) for year 1995. Comparison with 1D-SWAMCO-4 estimates obtained when biological activity is set at zero (**Table IV.2**) points out the significant contribution of biological processes to the atmospheric CO_2 sink in the Southern Ocean and especially in the marginal ice zone of the Ross Sea. In the absence of biological activity, these two locations are predicted to act as a source rather than a sink for atmospheric CO_2.
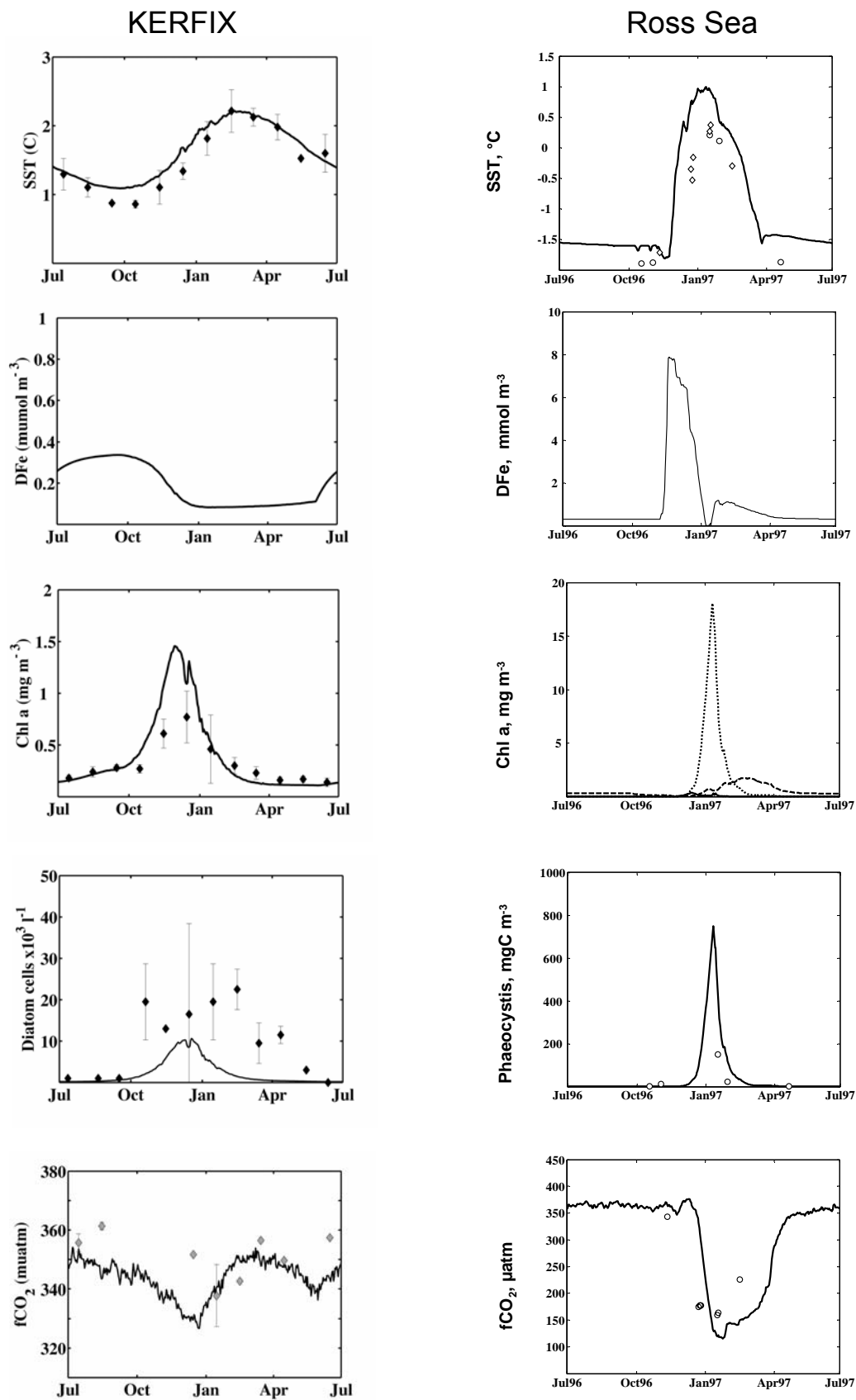
Figure IV.2 Observations and SWAMCO-4 simulations at st. KERFIX (Climatology 1993-2003) and Ross Sea (1996-1997).

Table IV.2. 1D-SWAMCO-4 estimations of annual primary production, carbon export production at 100m and air-sea CO_2 fluxes at 3 JGOFS sites locations. Comparison with published estimates

| JGOFS-site	Prim. Prod. $gC\ m^{-2}y^{-1}$	Export $gC\ m^{-2}\ y^{-1}$		Air-sea CO_2 $mole\ m^{-2}y^{-1}$		
	SWAMCO-4	SWAMCO-4	Data[1]	SWAMCO-4	Data[2]	SWAMCO-4 No biology
KERFIX	37	22	20-30	-0.4	-1- 0	+1.2
Ross Sea	83	21	5	-1.4	-2-0	+0.4

[1] *Schlitzer*, 2002

[2] *Takahashi et al.*, 2002 revised in
http://www.ldeo.columbia.edu/res/pi/CO2/carbondioxide/pages/air_sea_flux_rev1.htm

Forecasting of the ocean response to increased atmospheric CO_2 - Despite the obvious limitations of the 1 D representation of the water column, we performed long-term SWAMCO-4 runs to investigate the effects of changing atmospheric forcing (Temperature, wind, Global Solar Radiation, pCO_2) over the last decade with particular attention paid to the impact of atmospheric CO_2 increase. For this purpose we compared air-sea CO_2 fluxes obtained by running 1D SWAMCO-4 with prescribed increased atmospheric pCO2 and by maintaining it at a constant value corresponding for each test area at the spin-up year (**Fig.IV.3**). For all simulated regions, the ocean responds positively to the 1.2 ppm annual increase of atmospheric CO_2 imposed to the model over the simulated period but the predicted interannual variability of the air-sea CO_2 fluxes is regionally variable. At the KERFIX location, an average increased CO_2 uptake by the upper ocean of 0.27 mol C m^{-2} y^{-1} with respect to nominal year 1993 is simulated over the 1993-2002 period. Actually the highest atmospheric sink CO_2 is predicted in 2001, reaching - 0.9 mol m^{-2} y^{-1} *i.e.* about 3 times its value in 1994 (**Fig. IV.3**).

The effect of the oceanic conditions on the annual CO_2 are appraised by comparing current predictions with those obtained by keeping constant the atmospheric CO_2 of 1993 (**Fig. IV.2**). This comparison clearly suggests that the only meteorological forcing is modulating the increment of increased atmospheric CO_2 uptake by ±30%. However, our simulations at KERFIX clearly suggest that, after 1997, the effect of

increased atmospheric CO_2 has a larger impact on the predicted CO_2 sink than ocean conditions only
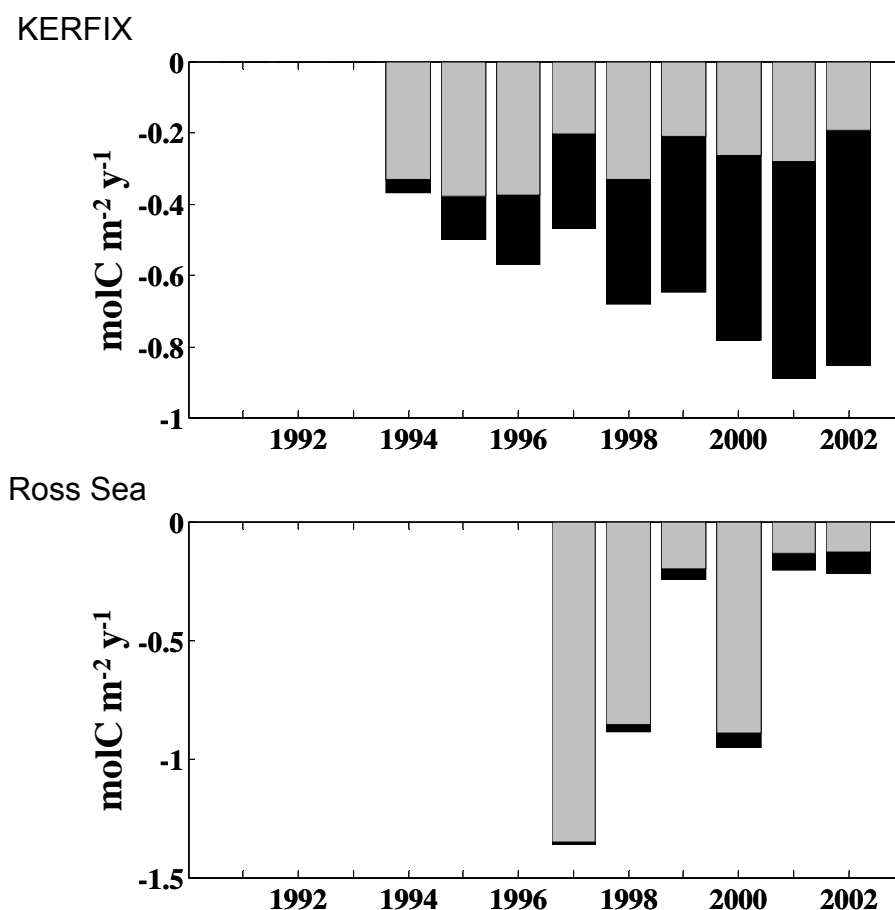
Figure IV.3. Long term SWAMCO-4 estimates of annual air-sea CO_2 fluxes for increasing (total vertical blocks) and constant (grey vertical blocks) atmospheric CO_2 corresponding to that of the spin-up year.

The largest interannual fluctuations of air-sea CO_2 fluxes were obtained in the marginal ice zone of the Ross Sea with values ranging between – 1.36 (1997) and – 0.2 (2001) mol C m^{-2} y^{-1} (**Fig.IV.3**). These fluctuations are clearly driven by the ice-covered conditions (shown from the comparison with model runs at constant atm. pCO$_2$ of 1991; **Fig.IV.3**) which determine the physical structure of the water column and hence the light conditions, the iron concentration and the responding dominant phytoplankter.

IV.3 Implementation and first results of ORCA-LIM-SWAMCO-4

As a first step towards the assessment of the Southern Ocean uptake of atmospheric CO_2, the SWAMCO model was coupled to the 3D ice-ocean ORCA2-LIM model (Timmermans et al., 2005) implemented in the domain south of latitude 30° with a grid of ~ 50km. Prior to its coupling with ORCA2-LIM, the trophic resolution of SWAMCO-4 was simplified based on numerical experimentations aiming at obtaining identical ecosystem behaviour with however a reduced number of state variables. Results of the sensitivity tests allowed decreasing the phytoplankton cell state variables from 3 to 2 and those describing organic matter from 4 to 2 (Pasquer, 2005).

ORCA-LIM-SWAMCO simulations were run from September 1999 to August 2000, using daily atmospheric forcing (*Timmermans et al.*, 2005). Initial conditions were those corresponding to the KERFIX station and no additional source (from below and/or from the top) of Fe was considered. Figure IV.4 compares monthly simulations of sea ice cover, surface Chl *a* and surface DFe during the process of ice retreat (September to February). Clearly the simulated temporal shift of algal blooms towards south latitudes indicates that the model well describes the dual effect of light (combination of latitudinal and ice coverage effects) and Fe limitation in controlling primary production. However, ORCA2-LIM-SWAMCO4 is presently ineffective in describing the well-observed algal blooms associated with the ice retreat. This results of both the absence of any external source of Fe in the model as well as a badly constrained mesozooplankton grazing which is the closure term of SWAMCO4. Further work will seek for improving the mesozooplankton parameterization and the description of iron sources in the Southern Ocean.
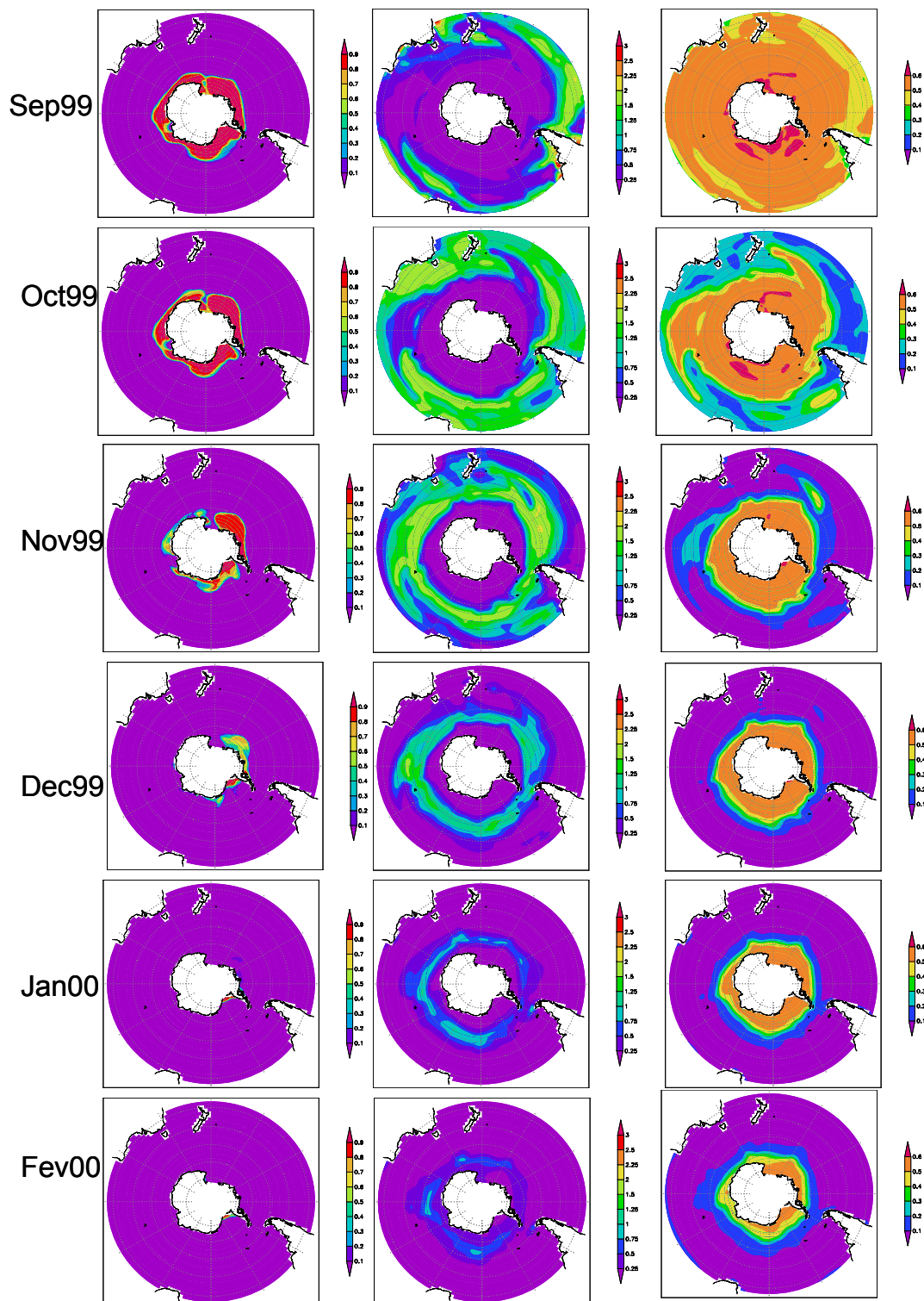
Figure IV.4: Monthly ORCA2-LIM-SWAMCO4 simulations of sea ice cover (left), surface Chl a (center) and surface DFe (right).

In order to assess the relative importance of thermodynamical and biological processes in determining the simulated ocean CO_2 pump, Figure IV.5 compares the winter and summer means of ORCA2-LIM-SWAMCO4 simulated fields of air-sea
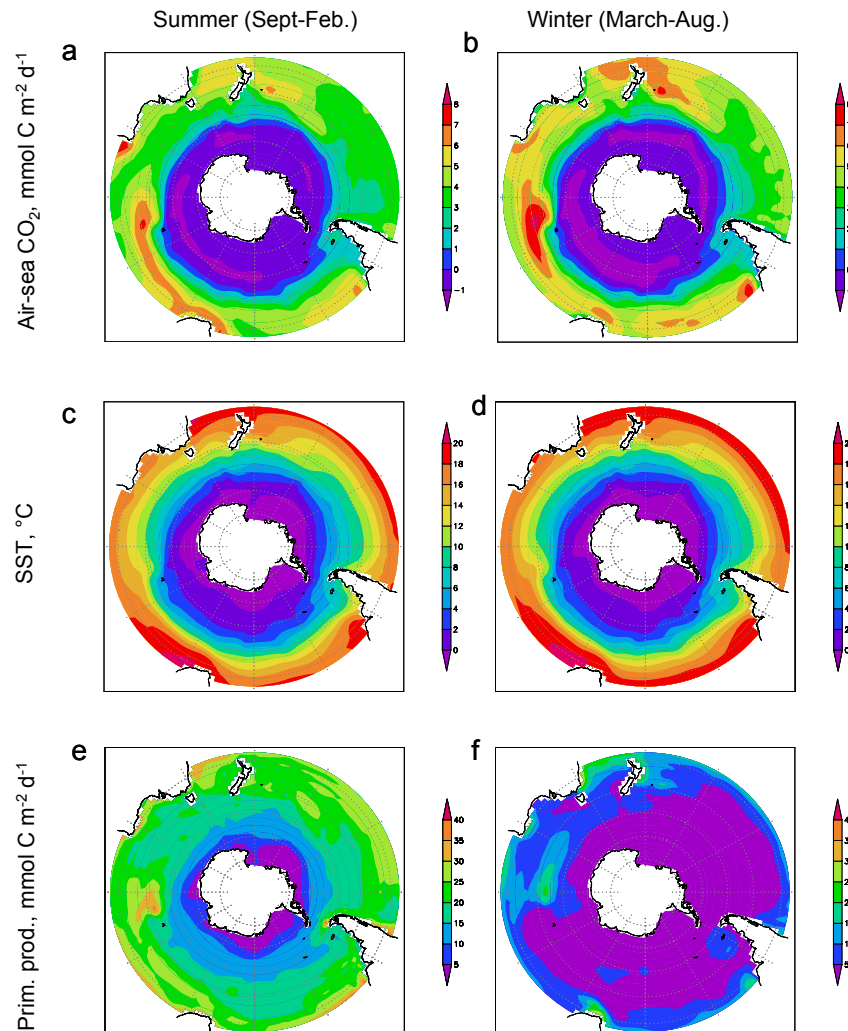
Figure IV.5. Winter and Summer mean ORCA2-LIM-SWAMCO4 simulations of air-sea daily CO_2 fluxes (a, b), SST (c, d) and daily primary production (e, f).

CO_2 fluxes with those of SST and primary production. Clearly thermodynamical processes are driving the simulated air-sea CO_2 fluxes in the area south of 50-55°S (~2°C isotherm) due to low simulated temperature and primary production. This conclusion might change when simulation of primary production in the marginal ice zone will be improved. North to latitude 50-55°S, however, the simulated field of air-sea CO_2 is clearly distinct from that of SST due to the significant diatom production (*Pasquer*, 2005).

Acknowledgements

References

Albert, M.R. and Perron, F.E., 2000. Ice layer and surface crust permeability in a seasonal snow pack. *Hydrological Processes,* 18: 3207-3214.

Albert, M.R., Grannas, A.M., Bottenheim, J., Shepson, P.B., and Perron, F.E., 2002. Processes and properties of snow-air transfer in the high Arctic with application to interstitial ozone at Alert, Canada. *Atmospheric Environment*, 36(15-16), 2779-2787.

Alleman, L.Y., Cardinal, D., Cocquyt, C., Plisnier, P.-D., Descy, J.-P., Kimirei, I., Sinyianza, D., and André, L., 2005. Silicon isotopic fractionation in Lake Tanganyika and its main tributaries. *Journal of Great Lakes Research,* 31:4, 509-519.

Altabet, M.A., and François, R., 2001. Nitrogen isotope biogeochemistry of the Antarctic Polar Frontal Zone at 170°W. *Deep-Sea Research II*, 48, 4247-4273.

Amiel, D., Cochran, J.K., and Hirschberg, D.J., 2002. ^{234}Th/^{238}U disequilibrium as an indicator of the seasonal export flux of particulate organic carbon in the North Water. *Deep-Sea Research II*, 49, 5191-5209.

Anderson, L.G., and Jones, E.P., 1985. Measurements of total alkalinity, calcium and sulfate in natural sea ice. *Journal of Geophysical Research*, 90(C5), 9194-9198.

Anderson R.F., Chase, Z., Fleisher M.Q. and Sachs. J., 2002. The Southern Ocean's biological pump during the Last Glacial Maximum. *Deep-Sea Research II*, 49, 1909-1938.

Armstrong, R.A., 2001. An optimization-based model of iron-light-ammonium colimitation of nitrate uptake and phytoplankton growth. *Limnology and Oceanography*, 44(6), 1436-1446.

Arrigo, K.R., 2003. Primary production in sea ice, in Sea ice: an introduction to its physics, chemistry, biology and geology, eds Thomas, D., and Dieckman, G. , 143-183.

Arzel, O., Fichefet, T., and Goosse, H., 2005. Sea ice evolution over the 20th and 21st centuries as simulated by current AOGCM. *Ocean Modelling* (submitted).

Aumont, O., Maier-Reimer, E., Blain, S., Monfray, P., 2003. An ecosystem model of the global ocean including Fe, Si, P co-limitations. *Global Biogeochemical Cycles*, 17: 1060, doi:10.1029/2001GB001745.

Beckmann, A., and Döscher, R., 1997. A method for improved representation of dense water spreading over topography in geopotential-coordinate models. *Journal of Physical Oceanography*, *27(4)*, 581-591.

Belkin, I.M., and Gordon, A.L., 1996. Southern Ocean fronts from the Greenwich meridian to Tasmania. *Journal of Geophysical Research,* 101, 3675-3696.

Benitez-Nelson, C. et al., 2001. Testing a new small-volume technique for determining thorium-234 in seawater. *Journal of Radioanalytical and Nuclear Chemistry,* 248: 795-799.

Berliand, M.E., and Strokina, T.G., 1980. Global distribution of the total amount of clouds (in Russian), 71 pp., *Hydrometeorological*, Leningrad, Russia.

Bishop J.K.B., 1988. The barite-opal-organic carbon association in oceanic particulate matter, *Nature*, 332, 341-343.

Blanke B., and Delecluse, P., (1993), Low frequency variability of the tropical Atlantic ocean simulated by a general circulation model with mixed layer physics, *J. Physical Oceanography*, *23*, 1363-1388.

Bhat, S.G., Krishnaswami, S., Lal, D., Rama and Moore, W.S., 1969. ^{234}Th/^{238}U ratios in the ocean. *Earth Planet. Sci. Lett.*, 5: 483-491.

Boyd, P., et al., 2000 A mesoscale phytoplankton bloom in the polar Southern Ocean stimulated by iron fertilization, *Nature*, 407, 695-702.

Brzezinski, M.A., Nelson, D.M., Franck, V.M., and Sigmon, D.E., 2001. Silicon dynamics within an intense open-ocean diatom bloom in the Pacific sector of the Southern Ocean. *Deep-Sea Research II*, 48, 3997-4018.

Brzezinski, M.A., Pride, C.J., Franck, V.M., Sigman, D.M., Sarmiento, J.L., Matsumoto, K., Gruber, N., Rau, G.H., and Coale, K.H., 2002. A switch from $Si(OH)_4$ to NO_3^- depletion in the glacial Southern Ocean. *Geophysical Research Letters*, 29, 10.1029/2001GL014349.

Brzezinski M.A., J.L. Jones, Bidle, K.D., and Azam, F., 2003a. The balance between silica production and silica dissolution in the sea: Insights from Monterey Bay, California, applied to the global data set. *Limnology and Oceanography*, 48, 1846-1854.

Bucciarelli, E., Blain, S., and Tréguer, P., 2001. Iron and Manganese in the wake of the Kerguelen Islands (Southern Ocean). *Marine Chemistry,* 73: 21-36.

Buesseler, K.O., et al., 1992b. Determination of thorium isotopes in seawater by non-destructive and radiochemical procedures. *Deep-Sea Research*, 39: 1103-1114.

Buesseler, K.O., et al., 1998. Upper ocean export of particulate organic carbon in the Arabian Sea derived from Thorium-234. *Deep-Sea Research II*, 45: 2461-2487.

Buesseler, K.O., et al., 2001. An intercomparison of small- and large-volume techniques for thorium-234 in seawater. *Marine Chemistry,* 74: 15-28.

Buesseler, K. O., Benitez-Nelson, C.R., Moran, S.B., Burd, A., Charette, M., Cochran, J.K., Coppola, L., Fisher, N.S., Fowler, S.W., Gardner, W.D., Guo, L.D., Gustafsson, Ö., Lamborg, C., Masque, P., Miquel, J.C., Passow, U., Santschi, P.H., Savoye, N., Stewart, G., and Trull, T.W., 2005. An assessment of particulate organic carbon to thorium-234 ratios in the ocean and their impact on the application of ^{234}Th as a POC flux proxy. *Marine Chemistry*, in press.

Buma, A.G.J., de Baar, H.J.W., Nolting, R.F., and van Bennekom, A.J., 1991. Metal enrichment experiments in the Weddell-Scotia Seas: effects of iron and manganese on various plankton communities. *Limnology and Oceanography,* 36, 1865-1878.

Cardinal, D., Dehairs, F., Cattaldo, T., and André, L., 2001. Geochemistry of suspended particles in the Subantarctic and polar Frontal Zones south of Australia: Constraints on export and advection processes, *Journal of Geophysical Research*, 106, 31,637– 31,656.

Cardinal, D., Savoye, N., Trull, T.W., André L., Kopczynska, E.E., and Dehairs, F., 2005. Variations of carbon remineralisation in the Southern Ocean illustrated by the Ba_{xs} proxy. *Deep-Sea Research I,* 52, 355–370.

Cardinal D., Alleman, L.Y., De Jong, J., Ziegler K., and André, L., 2003. Isotopic composition of silicon measured by multicollector plasma source mass spectrometry in dry plasma mode. *Journal of Analytical Atomic Spectrometry*, 18, 213-218, doi: 10.1039/b210109b.

Cardinal, D., Alleman, L.Y., Dehairs, F., Savoye, N., Trull, T.W., and André, L., 2005. Relevance of silicon isotopes to Si-nutrient utilization and Si source assessment in Antarctic waters. *Global Biogeochemical Cycles*, 19, GB2007 doi:10.1029/2004GB002364.

Cardinal D., Savoye, N., Trull, T.W., Dehairs, F., Kopczynska, E.E., Fripiat F., and André. L., Silicon isotopes in size fractionated spring Southern Ocean diatoms. *Marine Chemistry, in press.*

Carignan, J., Cardinal, D., Eisenhauer, A., Galy, A., Rehkämper, M., Wombacher, F., and Vigier, N., 2004. A reflection on Mg, Cd, Ca, Li and Si isotopic measurements and related reference materials. *Geostandards and Geoanalytical Research, 28:1, 139-148.*

Cavalieri, D.J., Comiso, J.C., and Markus, T., 2005. AMSR-E/Aqua Daily L3 25 km Tb, Sea Ice Temperature, and Sea Ice Conc. Polar Grids V001, September 2002 to January 2005.V001: National Snow and Ice Data Center

Chaigneau A., Morrow, R.A. and Rintoul, S.R., 2004. Seasonal and interannual evolution of the mixed layer in the Antarctic Zone south of Tasmania. *Deep-Sea Research I*, 51, 2047-2072.

Charette, M.A. and Buesseler, K.O., 2000. Does iron fertilization lead to rapid carbon export in the Southern Ocean? *Geochemistry, Geophysics, Geosystems - G 3*, 1.

Church, M.J., Hutchins, D.A., Ducklow, H.W., 2000. Limitation of bacterial growth by dissolved organic matter and iron in the Southern Ocean. *Applied Environmental Microbiololgy* 66: 455-466.

Chen, J.H., Edwards R.L., and Wasserburg G.J., 1986. ^{238}U, ^{234}U and ^{232}Th in seawater. *Earth and Planetary Science Letters*, 80, 241–251.

Chow, T.J., Goldberg, E.D., 1960. On the marine geochemistry of Barium. *Geochimica et Cosmochimica Acta* 20, 192.

Claquin P., Martin-Jézéquel, V., Kromkamp, J.C., Veldhuis, M.J.W., and Kraay, G.W., 2002. Uncoupling of silicon compared with carbon and nitrogen metabolisms and the role of the cell cycle in continuous cultures of Thalassiosira pseudonana (Bacillariophyceae) under light, nitrogen and phosphorus control. *Journal of Phycology*, 38, 922-930.

Coale, K.H., and Bruland, K.W., 1985. 234Th:238U disequilibria within the California current. *Limnology and Oceanography*, 30: 22- 33.

Cochlan, W.P., 2001. The heterotrophic bacterial response during a mesoscale iron enrichment experiment (IronEx II) in the eastern equatorial Pacific Ocean. *Limnology and Oceanography*. 46,428-435

Cochlan W.P., 2001. The heterotrophic bacterial response during a mesoscale iron enrichment experiment (IronEx II) in the eastern Equatorial Pacific Ocean. *Limnology and Oceanography,* 46: 428-435

Cochlan, W.P., Bronk, D.A. and Coale, K.H., 2002. Trace metals and nitrogenous nutrition of Antarctic phytoplankton: experimental observations in the Ross Sea. *Deep-Sea Research II*, 49(16), 3365-3390.

Cochran, J.K., Buesseler, K.O., Bacon, M.P., Wang, H.W., Hirschberg, D.J., Ball, L., Andrews, J., Crossin, G., Fleer, A., 2000. Short-lived thorium isotope (^{234}Th, ^{228}Th) as indicators of POC export and particle cycling in the Ross Sea, Southern Ocean, *Deep-Sea Research II* 47, 3451– 3490.

Conway, T.J., Tans, P.P., Waterman, L.S., Thoning, K.W., Kitzis, D.R., Masarie, K.A., and Zhang, N., 1994. Evidence for inter-annual variability of the carbon cycle from the National Oceanic and Atmospheric Administration/ Climate Monitoring and Diagnostics Laboratory Global Air sampling Network. *Journal of Geophysical Research*, 99(D11): 22831-22855.

Coppola, L., Roy-Barman, M., Wassmann, P., Mulsow, S. and Jeandel, C., 2002. Calibration of sediment traps and particulate organic carbon using ^{234}Th in the Barents Sea. *Marine Chemistry*, 80: 11-26.

Cox, G.F.N., and Weeks, W.F., 1983. Equations for determining the gas and brine volumes in sea-ice samples. *Journal of Glaciology*, 29, 306-316.

de Baar, H.J.W., Buma, A.G.J., Nolting, R.F., Cadee, G.C., Jaques, G., and Treguer, P.J., 1990. On iron limitation in the Southern Ocean: Experimental observations in the Weddell and Scotia Seas. *Marine Ecology Progress Series,* 65, 105-122.

de Baar, H.J.W., and De Jong, J.T.M., 2001. Distributions, sources and sinks of iron in seawater. In: Turner, D.R., and Hunter, K.A., (Editor), The biogeochemistry of iron in seawater. IUPAC Series on Analytical and Physical Chemistry of Environmental Systems., Chichester, pp. 125– 234.

de Freitas A.S.W., McCulloch, A.W., and McInnes, A.G., 1991. Recovery of silica from aqueous silicate solutions via trialkyl or tetraalkylammonium silicomolybdate. *Canadian Journal of Chemistry*, 69, 611-614.

De La Rocha, C.L., Brzezinski, M.A., and DeNiro, M.J., 1996. Purification, recovery and laser-driven fluorination of silicon from dissolved and particulate silica for the measurement of natural stable isotope abundances. *Analytical Chemistry*, 68, 3746-3750.

De La Rocha, C.L., Brzezinski M.A., and DeNiro, M.J., 1997. Fractionation of silicon isotopes by marine diatoms during biogenic silica formation, *Geochimica et Cosmochimica Acta*, 61, 5051-5056.

De La Rocha, C.L., Brzezinski, M.A., DeNiro, M.J., and Shemesh, A., 1998. Silicon-isotope composition of diatoms as an indicator of past oceanic change, *Nature*, 395, 680-683.

De La Rocha, C.L., Brzezinski, M.A., and DeNiro, M.J., 2000. A first look at the distribution of the stable isotopes of silicon in natural waters. *Geochimica et Cosmochimica Acta*, 64, 2467-2477.

De La Rocha, C.L., 2002. Measurement of silicon stable isotope natural abundances via multicollector inductively coupled plasma mass spectrometry (MC-ICP-MS). *Geochemistry, Geophysics, Geosystems*, 3(8), 10.1029/2002GC00310.

Dehairs, F., Stroobants, N., Goeyens, L., 1991. Suspended barite as a tracer of biological activity in the Southern Ocean. *Marine Chemistry* 35, 399– 410.

Dehairs, F., Baeyens, W., Goeyens, L., 1992. Accumulation of suspended barite at mesopelagic depths and export production in the Southern Ocean. *Science* 258, 1332– 1335.

Dehairs, F., Shopova, D., Ober, S., Veth, C., Goeyens, L., 1997. Particulate barium stocks and oxygen consumption in the Southern Ocean mesopelagic water column during spring and early summer: relationship with export production. *Deep-Sea Research. Part II*. 44 (1–2), 497– 516.

del Giorgio, P.A., and Cole, J.J., 2000. Bacterial energetics and growth efficiency. In: Kirchman D.L., (Ed). Microbial Ecology of the Oceans, Wiley-Liss Inc. 289-325.

Dickson, A.G. and Millero, F.J., 1987. A comparison of the equilibrium constants for the dissociation of carbonic acid in seawater media, *Deep-Sea Research Part I*, 34, 1733-1743.

Ducklow, H.W., Steinberg, D.K., and Buesseler, K.O., 2001. Upper Ocean Carbon Export and the Biological Pump, *Oceanography*, 14 (4 (JGOFS Special Issue)), 50-58.

Dortch, Q., 1990. The interaction between ammonium and nitrate uptake in phytoplankton. *Marine Ecology Progress Series*, 61, 183-201.

Dugdale, R.C., Goering, J.J., 1967. Uptake of new and regenerated forms of nitrogen in primary productivity. *Limnology and Oceanography*, 12: 196-206.

Elskens, M., Baeyens, W., Cattaldo, T., Dehairs, F., and Griffiths, B., 2002. N-uptake conditions during the summer in the sub-Antarctic and Polar Frontal Zones of the Australian sector of the Southern Ocean. *Journal of Geophysical Research*, 107(3), 1-11.

Eppley, R.W., and Peterson, B.J., 1979. Particulate organic matter flux and plankton new production in the deep ocean. *Nature*, 282, 677-680.

Fichefet, T., and Morales Maqueda, M.A., 1997. Sensitivity of a global sea ice model to the treatment of ice thermodynamics and dynamics, *Journal of Geophysical. Research, 102(C6)*, 12609-12646.

Flato, G.M. and Boer, G.J. 2001. Warming asymetry in climate change simulations. *Geophysical Research Letters*, 28, 195-198.

François, R., Honjo, S., Manganini, S.J., and Ravizza, G.E., 1995. Biogenic barium fluxes to the deep sea: Implication for paleoproductivity reconstruction, *Global Biogeochemical Cycles*, 9(2), 289-303.

François, R., Honjo, S., Krishfield, R., and Manganini, S., 2002. Factors controlling the flux of organic carbon to the bathypelagic zone of the ocean. *Global Biogeochemical Cycles* 16, 1087.

Frankignoulle, M., and Borges, A.V., 2001. Direct and indirect pCO_2 measurements in a wide range of pCO_2 and salinity values (the Scheldt estuary), *Aquatic Geochemistry*, 7: 267-273, doi:10.1023/A:1015251010481

Fripiat, F., 2005. Etude structurale et isotopique du silicium dans la glace de banquise Antarctique. M. Sc. Thesis, Université Libre de Bruxelles, 117pp.

Furhman, J.A., and Azam, F., 1982. Thymidine incorporation as a measure of heterotrophic bacterioplankton production in marine surface waters: Evaluation and field results. *Marine Biology* 66: 109-120

Fripiat F., Cardinal, D., Tison, J.-L., and André, L., Silicon isotopic fractionation induced by diatoms in Antarctic sea ice. In preparation.

Ganeshram, R. S., François, R., Commeau, J., and Brown-Leger, S.L., 2003. An experimental investigation of barite formation in seawater, *Geochimica Cosmochimica Acta*, 67, 2599–2605.

Gervais, F., Riebesell, U., and Gorbunov, M.Y., 2002. Changes in primary productivity and chlorophyll *a* in response to iron fertilization in the Southern Polar Frontal Zone, *Limnology and Oceanography*, 47, 1324-1335.

Gent, P.R., and McWilliams, J.C., 1990. Isopycnal mixing in ocean circulation models. *Journal of Physical Oceanography. 20*, 150-155.

Gleitz M., Rutgers van der Loeff M., Thomas D.N., Dieckmann G.S. and Millero F.J., 1995. Comparison of summer and winter inorganic carbon oxygen and nutrient concentrations in Antarctic sea ice brine. *Marine Chemistry*, 51, 81-91.

Gleitz, M., M.R.v.d.Loeff, D.N.Thomas, G.S.Dieckmann and F.J.Millero, 1995. Comparison of summer and winter in organic carbon, oxygen and nutrient concentrations in Antarctic sea ice brine, Marine Chemistry, 51(2), 81-91.

Gloor, M., Gruber, N., Sarmiento, J.L., Sabine, C.L., Feely, R.A., and Rödenbeck, C. 2003. A first estimate of present and preindustrial air-sea CO2 flux patterns based on ocean interior carbon measurements and models. *Geophysical Research Letters* 30(11), doi:10.1029/2002GL015594.

Goeyens, L., Semeneh, M., Baumann, M.E.M., Elskens, M., Shopova, D., and Dehairs, F., 1998. Phytoplanktonic nutrient utilization and nutrient signature in the Southern Ocean, *Journal of Marine Systems*, 17, 143– 157.

Golden, K.M., 2001. Brine percolation and the transport properties of sea ice. *Annals of glaciology*, 33: 28-36.

Goosse, H., 1997. Modelling the large-scale behaviour of the coupled ocean–sea-ice system, Ph.D. thesis, 231 pp., Fac. des Sci. Appl., Univ. Cath. de Louvain, Louvain-la-Neuve, Belgium.

Goosse, H., and Fichefet, T., 1999. Importance of ice-ocean interactions for the global ocean circulation: A model study, *Journal of Geophysical Research*, *104,* 23337-23355.

Goosse, H., Campin, J.M., Deleersnijder E., Fichefet T., Mathieu, P.P., Morales Maqueda, M.A., Tartinville, B., 2000. Description of the CLIO model version 3.0. Scientific Report 2000/3, Institut d'Astronomie et de Géophysique G. Lemaître, Louvain-la-Neuve, Belgium.

Goosse, H., Masson-Delmotte, V., Renssen, H., Delmotte, M., Fichefet, T., Morgan, V., van Ommen, T., Khim, B.K. and Stenni, B. 2004. A late medieval warm period in the Southern Ocean as delayed response to external forcing ? *Geophysical Research Letters* 31(6) L06203 doi:10.1029/2003GL019140.

Goosse, H. and Renssen, H., 2001. A two-phase response of Southern Ocean to an increase in greenhouse gas concentrations. *Geophysical Research Letters* 28, 3469-3473.

Goosse, H. and Renssen, H. 2005. A simulated reduction in Antarctic sea-ice area since 1750: implications of the long memory of the ocean*. International Journal of Climatology* 25, 569-579.

Gosink, T.A., Pearson J.G., and Kelley, J.J., 1976. Gas movement through sea ice, Nature, 263(2), 41-42.

Gurney, K.R., Law, R.M., Denning, A.S., Rayner, P.J., Pak, B.C., Baker, D., Bousquet, P., Bruhwiler, L., Chen, Y.H., Ciais, P., Fung, I.Y., Heimann, M., John, J., Maki, T., Maksyutov, S., Peylin, P., Prather, M., and Taguchi, S. 2004. Transcom 3 inversion intercomparison: Model mean results for the estimation of seasonal carbon sources and sinks. *Global Biogeochemical Cycles,* 18(GB1010) doi:10.1029/2003GB002111.

Hall J.A., and Safi K. 2001. The impact of in situ Fe fertilisation on the microbial food web in the Southern Ocean. *Deep-Sea Research II* 48: 2591-2613

Hannon, E., Boyd, P.W., Silvoso, M., and Lancelot C., 2001. Modelling the bloom evolution and carbon flows during SOIREE: Implications for future in situ iron-experiments in the Southern Ocean. *Deep-Sea Research II*, 48: 2745-2773.

Hansell, D.A. and C.A. Carlson. 2001. Marine dissolved organic matter and the carbon cycle. Oceanography 14: 41-49.

Harder, M. and Fischer, H. 1999, Sea ice dynamics in the Weddell Sea simulated with an optimized model, *Journal of Geophysical Research*, *104*, 11,151–11,162.

Hibler, W.D., III 1979. A dynamic thermodynamic sea ice model. *Journal of Physical Oceanography, 9(4)*, 815-846

Hutchins, D.A., DiTullio, G.R., Zhang, Y., and Bruland, W., 1998. An iron limitation mosaic in the California upwelling regime. *Limnology and Oceanography* 43: 1037-1054

Ittekkot, V., Haake, B., Bartsch, M., Nair, R.R., Ramaswamy, V., 1992. Organic carbon removal in the sea: the continental connection. In: Summerhayes, C.P., Prell, W.L., Emeis, K.C. (eds.), Upwelling Systems: evolution since the Early Miocene, vol. 64. Geological Society Special Publication, pp. 167–176.

Jacobson, A.R., Sarmiento, J., Gloor, M., Gruber, N., and Mikaloff Fletcher, S.E., 2005. Oceanic constraints on the size of the Terrestrial CO_2 fertilization sink. Seventh International Carbon Dioxide Conference, Boulder, Colorado, U.S.A., September 25-30.

Jacquet, S.H.M., Dehairs, F., Cardinal, D., Navez, J. and Delille, B. 2005. Barium distribution across the Southern Ocean Frontal system in the Crozet-Kerguelen Basin, *Marine Chemistry*, 95 (3-4): 149-162.

Jacquet S.H.M., Dehairs, F. and S., Rintoul. A high resolution transect of dissolved barium in the Southern Ocean, *Geophysical Research Letters*, 31, L14301, doi: 10,1029/2004GL20016.

Jacquet, S.H.M., Dehairs, F., Cardinal, D., Savoye, N., Elskens, M. and Trull, T., Barium-cycle dynamics in the Australian sector of the Southern Ocean, submitted to *Marine Chemistry*.

Jones, E.P., Coote A.R. and Levy, E.M. 1983. Effect of sea ice meltwater on the alkalinity of sewater, *Journal of Marine Research*, 41, 43-52.

Kalnay, E., Kanamitsu, M., Kistler, R. , Collins, W., Deaven, D., Gandin, L., Iredell, M., Saha, S., White, G., Woollen, J., Zhu, Y., Chelliah, M., Ebisuzaki, W., Higgins, W., Janowiak, J., Mo, K.C., Ropelewski, C., Wang, J., Leetmaa, A., Reynolds, R., Jenne, E., Joseph, D., 1996: The NCEP/NCAR 40-year reanalysis project. *Bulletin of the American Meteorological Society*, 77, 437-471.

Large, W. G., and S. Pond (1981), Open ocean momentum flux measurements in moderate to strong winds. *Journal of Physical Oceanography*.11, 324–336.

Karl, D.M., and Tien, G., 1992. MAGIC: A sensitive and precise method for measuring dissolved phosphorus in aquatic environments. *Limnology and Oceanography*, 37, 105-116.

Karsh, K.L., Trull, T.W., Lourey, M.J., and Sigman, D.M., 2003. Relationship of nitrogen isotope fractionation to phytoplankton size and iron availability during the Southern Ocean Iron RElease Experiment (SOIREE). *Limnology and Oceanography*, 48, 1058-1068.

Kirchman, D.L., Meon, B., Cottrell, M.T., and Hutchins, D.A., 2000. Carbon versus iron limitation of bacterial growth in the California upwelling regime. *Limnology and Oceanography,* 45 (8): 1681-1688

Klaas, C., and Archer, D.E., 2002. Association of sinking organic matter with various types of mineral ballast in the deep sea: implications for the rain ratio. *Global Biogeochemical Cycles,* 16, 1116.

Kopczyńska E. E., Savoye, N., Dehairs, F., Cardinal, D., and Elskens, M., Spring phytoplankton assemblages in the Southern Ocean between Australia and Antarctica; relationship to nitrogen regime, *Deep-Sea Research*, submitted.

Kostianoy, A.G., Ginzburg, A.I., Frankignoulle, M., and Delille, B. 2004. Fronts in the Southern Indian Ocean as inferred from satellite sea surface temperature data. *Journal of Marine Systems,*1-2: 55-73.

Kostianoy, A.G., Ginzburg, A.I., Lebedev, S.A., Frankignoulle, M., and Delille, B., 2003. Fronts and mesoscale variability in the southern Indian Ocean as inferred from the TOPEX/POSEIDON and ERS-2 altimetry data. *Oceanology*, 5: 632-642.

Kudo, I., Miyamoto, M., Noiri, Y., Maita Y., 2000. Combined effects of temperature and iron on the growth and physiology of the marine diatom Phaeodactylum tricornutum (Bacillariophyceae). *Journal of Phycology,* 36 (6): 1096–1102

Kwok, R. and Comiso, J.C. 2002), Southern Ocean climate and sea ice anomalies associated with the Southern Oscillation, *Journal of Climatology,* 15, 487-501.

Lancelot, C., Veth, C. and Mathot, S., 1991. Modelling ice-edge phytoplankton bloom in the Scotia-Weddell Sea sector of the Southern Ocean during spring 1988. *Journal of Marine Systems*, 2: 333-346.

Lancelot, C., Hannon, E., Becquevort, S., Veth, C. and de Baar, H.J.W., 2000. Modelling phytoplankton blooms and carbon export in the Southern Ocean: dominant controls by light and iron in the Atlantic sector in Austral spring 1992. *Deep-Sea Research I*, 47: 1621-1662.

Laubscher, R.K., Perissinotto, R. and McQuaid, C.D., 1993. Phytoplankton production and biomass at frontal zones in the Atlantic sector of the Southern Ocean. *Polar Biology* 13, 471–481.

Laws, E.A., Falkowski, P.G., Smith, Jr. W.O., Ducklow, H. and McCarthy, J.J., 2000. Temperature effects on export production in the open ocean. *Global Biogeochemical Cycles*, vol. 14, 4, 1231-1246.

Lefebvre, W., Goosse, H., Timmermann, R., and Fichefet, T., 2004. Influence of the Southern Annular Mode on the sea ice—ocean system, *Journal of Geophysical. Research*, 109, C09005, doi:10.1029/2004JC002403.

Lefèvre, N., and Watson, A.J., 1999. Modeling the geochemical cycle of iron in the oceans and its impact on atmospheric CO_2 concentrations. *Global Biogeochemical Cycles*, 13(3): 727-736.

Liu J., Curry, J.A. and Martinson, D.G. 2004. Interpretation of recent Antarctic sea ice variability, G*eophysical. Research Letters,* 31, L02205, DOI:10.1029/ 2003GL018732.

Liss, P.S. and Merlivat, L. 1986. Air-sea exchange rates: introduction and synthesis, in The role of air-sea exchanges in geochemical cycling (ed Buat-Ménard), 113-118. Reidel

Lizotte, M.P. 2001. The contributions of sea ice algae to Antarctic marine primary production. *American zoologist*,1: 57-73.

Lizotte, M.P. and C.W.Sullivan, 1992. Biochemical-composition and photosynthate distribution in sea ice microalgae of mcmurdo-sound, antarctica - evidence for nutrient stress during the spring bloom, *Antarctic Science*, 4(1), 23-30.

Longhurst, A., 1998. Ecological geography of the sea. Academic Press. San Diego (USA). 398pp.

Lourey, M. J., and Trull T. W., 2001. Seasonal nutrient depletion and carbon export in the Subantarctic and Polar Frontal Zones of the Southern Ocean south of Australia. *Journal of Geophysical Research*, 106(C12), 31,463– 31,487.

Madec G., Delecluse, P., Imbard, M. and Lévy, C. 1999. OPA 8.1 Ocean General Circulation Model reference manual, *Notes du Pôle de modélisation*, Institut Pierre-Simon Laplace (IPSL), France, X, 91 pp.

Maranger, R., and M. J. Pullin. 2003. Elemental complexation by dissolved organic matter in lakes: implications for Fe speciation and the bioavailability of Fe and P. Pages 185– 214 in Findlay S.E.G. and Sinsabaugh R.L., editors. Aquatic ecosystems: interactivity of dissolved organic matter. Academic Press/Elsevier Science, San Diego, California, USA.

Mariotti A., Germon, J.C., Hubert, P., Kaiser, P., Letolle, R., Tardieux, A., and Tardieux, P., 1981. Experimental determination of nitrogen kinetic isotope fractionation: some principles; illustration for the denitrification and nitrification processes. *Plant and Soil*, 62, 413-430.

Martin-Jézéquel V., Hildebrand M. and Brzezinski M.A., 2000. Silicon metabolism in diatoms: implications for growth. *Journal of Phycology*, 36, 821-840.

Martin, J.H. and Fitzwater S.E.. 1988. Iron deficiency limits phytoplankton growth in the north-east Pacific subarctic, *Nature*, 331, 341-343.

Matsumoto K. and J.L. Sarmiento and M.A. Brzezinski, 2002. Silicic acid leakage from the Southern Ocean: A possible explanation for glacial atmospheric pCO$_2$. *Global Biogeochemical Cycles*, 16(3), 10.1029/2001GB001442.

Massman, W.J., Sommerfeld, R.A., Mosier, A.R., Zeller, K.F., Hehn T.J. and Rochelle, S.G., 1997. A model investigation of turbulence-driven pressure-pumping effects on the rate of diffusion of CO$_2$, N$_2$O, and CH$_4$ through layered snowpacks, *Journal of Geophysical Research-Atmospheres*, 102(D15), 18851-18863.

Mehrbach, C., Culberson, C.H., Hawley, J.E., and Pytkowicz, R.M., 1973. Measurements of the apparent dissociation constants of carbonic acid in seawater at atmospheric pressure, Limnology and Oceanography, 18, 897-907.

Merryfield, W.J., Holloway, G. and Gargett, A.E., 1999. A global ocean model with double-diffusive mixing. *Journal of Physical Oceanography*, 29, 1124-1142.

Metzl, N., Poisson, A., Louanchi, F., Brunet, C., Schauer, B., and Brès, B., 1995. Spatio-temporal distribution of air-sea fluxes of CO_2 in the Indian and Antarctic Ocean. *Tellus* 56-69.

Metzl, N., Tilbrook, B., and Poisson, A., 1999. The annual fCO_2 cycle and the air-sea CO_2 flux in the sub-Antarctic Ocean. *Tellus B*: 849-861.

Mo, Ropelewski, C., Wang, J., Leetmaa, A., Reynolds, R., Jenne, R., and Joseph, D., 1996. The NCEP/NCAR 40-year reanalysis project, *Bulletin of American Meteorological Society*, 77, 437–470.

Monnin C., Jeandel C., Cattaldo T. and Dehairs F., 1999. The marine barite saturation state of the world's ocean. *Marine Chemistry*, 65: 253-261.

Moore, K.J., Doney, S.C., Kleypas, J.A., Glover, D.M., and Fung, I.Y., 2002. An intermediate complexity marine ecosystem model for the global domain. *Deep-Sea Research II*, 49: 403-462.

Murray, J.W. et al., 1996. Export flux of particulate organic carbon from the central equatorial Pacific determined using a combined drifting trap Th-234 approach. *Deep-Sea Research II*, 43(4-6): 1095-1132.

Nelson, D.M., Brzezinski, M.A., Sigmon, D.E., and Franck, V.M., 2001. A seasonal progression of Si limitation in the Pacific sector of the Southern Ocean. *Deep-Sea Research II*, 48, 3973-3995.

Obata H., Karatani, H., and Nakayama, E., 1993. Automated determination of iron in seawater by chelating resin concentration and chemiluminescence detection. Analytical Chemistry 5: 1524-1528

Opfergelt S., Cardinal D., Henriet C., Draye X., André L., and Delvaux, B,. Silicon isotope fractionation by banana (*Musa* spp.) grown in a continuous nutrient flow device. *Plant and Soil,* in press.

Orsi, A., Whitworth, III T., and Nowlin, W.D., 1995. On the meridional extent and fronts of the Antarctic Circumpolar Current, *Deep-Sea Research* I, 42, 641-673.

Orsi, A.H., Johnson, G.C., and Bullister, J.L., 1999. Circulation, mixing, and production of Antarctic Bottom Water, *Progress in Oceanography*, 43, 55-119.

Rushdi, A.I., McManus, J., Collier, R.W., 2000. Marine barite and celestite saturation in seawater. *Marine Chemistry* 69 (1–2), 19– 31.

Paasche, E., 2002. A review of the coccolithophorid Emiliana huxleyi (Prymnesiophyceae), with particular reference to growth, coccolith formation, and calcification- photosynthesis interactions. *Phycologia*, 40(6): 503-529.

Pakulski, J.D., Coffin, R.B., Kelley, C.A., Holder, S.L., Downer, R., Aas, D.P., Lyons, M.M., and Jeffrey, W.H., 1996. Iron stimulation of Antarctic bacteria. *Nature* 383: 133-143

Papadimitriou, S., Kennedy, H., Kattner, G., Dieckmann, G.S., and Thomas, D.N., 15-4-2004. Experimental evidence for carbonate precipitation and CO_2 degassing during sea ice formation, *Geochimica et Cosmochimica Acta*, 68(8), 1749-1761.

Pasquer, B., 2005. Modélisation de la pompe biologique de carbone dans l'océan Austral. PhD dissertation. Université Libre de Bruxelles. 220pp

Pasquer, B., Laruelle G., Becquevort, S., Schoemann, V., and Goosse, H., Lancelot, C., 2005. Linking ocean biogeochemical cycles and ecosystem structure and function: results of the complex SWAMCO-4 model. *Journal of Sea Research*, 53: 93-108.

Pasquer, B., Goosse, H., Metzl, N., Lancelot, C. Testing a 1D coupled physical-biogeochemical model in the Open Ocean Zone of the Southern Ocean for understanding the seasonal variability of air-sea CO_2 fluxes. *Deep-Sea Research,* submitted.

Pike, S.M., Buesseler, K.O., Andrews, J. and Savoye, N., 2005. Quantification of Th-234 recovery in small volume seawater samples by inductively coupled plasma-mass spectrometry. *Journal of Radioanalytical and Nuclear Chemistry* 263: 355-360.

Poisson, A. and Chen, C.T.A., 1987. Why is there little anthropogenic CO2 in the Antarctic bottom water?, *Deep-Sea Research Part A*, 34(7), 1255-1275.

Pollard, R.T., Lucas, M.I. and Read J.F. (2002), Physical controls on biogeochemical zonation in the Southern Ocean. *Deep Sea Research part II*, 49,3289– 3305.

Porter K.G., Feig Y.S. 1980. The use of DAPI for identifying and counting aquatic microflora. Limnol Oceanogr 25: 943-948.

Rangama, Y., Boutin, J., Etcheto, J., Merlivat, L., Takahashi, T., Delille, B., Frankignoulle, M., and Bakker, D.C.E., 2004. Variability of net air-sea CO_2 flux inferred from in situ and satellite measurements in the Southern Ocean south of Tasmania and New Zealand. *Journal of Geophysical Research*, 110(C9), C09005, doi:10.1029/2004JC002619.

Rayner N.A., Parker, D.E., Horton, E.B., Folland, C.K., Alexander, L.V., Rowell, D.P., Kent, E.C., and Kaplan, A., 2003, Global analyses of sea surface temperature, sea ice, and night marine air temperature since the late nineteenth century, *Journal. Geophysical Research*, 108(D14), 4407, doi:10.1029/2002JD002670.

Rintoul, S.R., 1998. On the origin and influence of Adelie Land Bottom Water, in *Ocean, Ice and Atmosphere: Interactions at the Antarctic Continental Margin*, edited by S. Jacobs, and R. Weiss, pp. 151-171, American Geophysical Union, Washington, D. C.

Rintoul, S.R. and Bullister, J.L., 1999. A late winter hydrographic section from Tasmania to Antarctica. *Deep-Sea Research Part I*, 46, 1417-1454.

Rintoul, S.R. and Trull, T.W., 2001. Seasonal evolution of the mixed layer in the Subantarctic Zone south of Australia. *Journal of Geophysical Research,* 106, 31447-31462.

Rodriguez, G.G., Phipps, D., Ishiguro, K., and Ridgeway, H.F., 1992. Use of fluorescent redox probe for direct visualization of actively respiring bacteria. *Applied Environmental Microbiology* 58:1801-1808.

Roy, T., Rayner, P.J., Matear, R., and Francey, R.J., 1-4-2003. Southern hemisphere ocean CO_2 uptake: reconciling atmospheric and oceanic estimates. *Tellus B*, 55(2), 701-710.

Rushdi, A.I., McManus, J., and Collier, R.W., 2000. Marine barite and celestite saturation in seawater. *Marine Chemistry*, 69, 19-31.

Rutgers van der Loeff, M.M., Friedrich, J., and Bathmann, U.V., 1997. Carbon export during the spring bloom at the Antarctic Polar Front, determined with the natural tracer [234]Th. *Deep-Sea Research II* 44 (1–2), 457– 478.

Rutgers van der Loeff, M.M., Buesseler, K., Bathmann, U., Hense, I., and Andrews, J., 2002. Comparison of carbon and opal export rates between summer andspring bloom periodsin the region of the Antarctic Polar Front, SE Atlantic. *Deep-Sea Research II* 49, 3849–3869.

Sambrotto, R. N., and Mace, B.J., 2000. Coupling of biological and physical regimes across the Antarctic Polar Front as reflected by nitrogen production and recycling, *Deep Sea Research part II*, 47(15 – 16), 3339 – 3367.

Sarmiento, J.L., Gruber, N., Brzezinski, M.A., and J.P., Dunne, 2004. High-latitude controls of thermocline nutrients and low latitude biological productivity. *Nature*, 427, 56-60.

Sarthou, G., Timmermans, K., Blain, S., Tréguer, P., and de Baar, H.J.W., 2005. Growth physiology and fate of diatoms in the ocean: a review. *Journal of Sea Research*, 53(1-2): 25-42.

Savoye, N., Buesseler, K.O., Cardinal, D. and Dehairs, F., 2004. [234]Th deficit and excess in the Southern Ocean during spring 2001: Particle export and remineralization. *Geophysical Research Letters*, 31(12,L12301): 10.1029/2004GL019744.

Savoye, N., F. Dehairs, M. Elskens, D. Cardinal, E. E. Kopczyn˜ska, T. W. Trull, S. Wright, W. Baeyens, and F. B. Griffiths (2004), Regional variation of spring N-uptake and new production in the Southern Ocean, *Geophysical Research Letters*, 31, L03301, doi:10.1029/2003GL018946.

Savoye N., Benitez-Nelson, C., Burd, A. B., Cochran, J. K., Charette, M., Buesseler, K.O., Jackson, G.A., Roy-Barman, M., Schmidt, S., and Elskens, M., (2005) ^{234}Th sorption and export models in the water column: a review. *Marine Chemistry.* In press.

Schlitzer, R., 2002. Carbon export fluxes in the Southern Ocean: results from inverse modeling and comparison with satellite-based estimates. *Deep Sea Research part II*, 49(9-10): 1623-1644.

Schoemann, V., Becquevort, S., Stefels, J., Rousseau, V., and Lancelot C., 2005. Phaeocystis blooms in the global ocean and their controlling mechanisms: a review. *Journal of Sea Research*, 53(43-66).

Sedwick, P., Bowie, A., and Ussher, S., (2002), Dissolved iron in the Australian sector of the Southern Ocean during spring: Implications for the seasonal cycle of iron in Antarctic surface waters, *Eos Transactions AGU*, 83(47), Fall Meet. Suppl. Abstract OS11A-0220.

Sedwick, P., DiTullio, G.R., 1997. Regulation of algal blooms in Antarctic shelf waters by the release of iron from melting sea ice. *Geophysical Research Letters*, 24: 2515-2518.

Semiletov, I., A.Makshtas, S.I.Akasofu and E.L.Andreas, 2004. Atmospheric CO2 balance: The role of Arctic sea ice, *Geophysical Research Letters,* 31(5), L05121-doi:10.1029/2003GL017996.

Sigman D.M., M.A. Altabet, D.C. McCorkle, R. François and G. Fischer, 1999. The δ^{15}N of nitrate in the Southern Ocean: consumption of nitrate in surface waters. *Global Biogeochemical Cycles*, 13(4), 1149-1166.

Smith E.M., and del Giorgio P.A. 2003. Low fractions of active bacteria in natural aquatic communities? *Aquatic Microbial Ecology* 31: 203-208.

Sokolov, S., and S. R. Rintoul (2002), Structure of Southern Ocean fronts at 140°E, *Journal of Marine Systems*, 37, 151–184.

Stössel, A. 1992. Sensitivity of the Southern Ocean sea-ice simulations to different atmospheric forcing algorithms, *Tellus*, 44A, 395–413.

Struraro, G., 2003. A closer look at the climatological discontinuities present in the NCEP/NCAR reanalysis temperature due to the introduction of satellite data, *Clymate Dynamics* 21, 309-316, doi:10.1007/s00382-003-0334-4

Sugimura, Y., and Suzuki, Y. 1988. A high temperature catalytic oxidation method for the determination of non-volatile dissolved organic carbon in seawater by direct injection of a liquid sample. *Marine Chemistry* 24: 105-131

Takahashi, T., Sutherland, S.C., Sweeney, C., Poisson, A., Metzl, N., Tilbrook, B., Bates, N.R., Wanninkhof, R., Feely, R.A., Sabine, C., Olafsson, J., and Nojiri, Y. 2002. Global sea-air CO2 flux based on climatological surface ocean pCO2, and seasonal biological and temperature effects. *Deep-Sea Research. II*, 9-10: 1601-1622

Takahashi, H. 2003. Ocean basin summations of sea-air flux computed using the 10 Meter Height Winds, (http://www.ldeo.columbia.edu/res/pi/CO2/carbondioxide/ text/10m_wind.prn).

Takagi, K. et al, 2005. Dynamic carbon dioxide exchange through snowpack by wind-driven mass transfer in a conifer-broadleaf mixed forest in northernmost Japan, Global Biogeochemical Cycles, 19(2).

Timmermann, R., Goosse, H., Madec, G., Fichefet, T., Ethe, C. and Dulière, V. 2004a. On the representation of high latitude processes in the ORCALIM global coupled sea-ice model, *Ocean Modelling,* in press, doi:10.1016/j.ocemod.2003.12.009.

Timmermann, R., Worby, A., Goosse, H. and Fichefet, T. 2004. Utilizing the ASPeCt sea ice thickness data set to validate a global coupled sea ice--ocean model. *Journal of Geophysical Research* 109, C07017,doi.1029/2003JC002242.

Timmermann, R., Goosse, H., Madec, G., Fichefet, T., Ethe, C. and Dulière, V., 2005. On the representation of high latitude processes in the ORCALIM global coupled sea ice-ocean model. *Ocean Modelling* 8, 175-201.

Timmermans, K.R., Gerringa, L.J.A., de Baar, H.J.W., van der Wagt, B., Veldhuis, M.J.W., de Jong, J.T.M., and Croot, P.L., 2001. Growth rates of large and small Southern Ocean diatoms in relation to availability of iron in natural seawater. *Limnology and Oceanography*, 46(2): 260-266.

Timmermans, K.R., van der Wagt, B., de Baar, and H.J.W., 2004. Growth rates, half-saturation constants, and silicate, nitrate and phosphate depletion in relation to iron availability of four large, open-ocean diatoms from the Southern Ocean. *Limnology and Oceanography*, 49(6): 2141-2151.

Tison, J.L., C.Haas, M.M.Gowing, S.Sleewaegen and A.Bernard, 2002. Tank study of physico-chemical controls on gas content and composition during growth of young sea ice, *Journal of Glaciology*, 48(161), 177-191.

Trenberth, K.E., Olson, J.G. and Large, W.G. 1989. A global ocean wind stress climatology based on the ECMWF analyses, National Center for Atmospheric Research, NCAR/TN-338+STR, 93 pp, NCAR, Boulder, USA.

Trull, T.W., Rintoul, S.R., Hadfield, M., and Abraham, R., 2001. Circulation and seasonal evolution of polar waters south of Australia: Implication for iron fertilization of the Southern Ocean, *Deep Sea Research part II*, 48, 2439–2466.

Trull, T.W., Bray, S.G., Manganini, S.J., Honjo, S., and François, R., (2001b), Moored sediment trap measurements of carbon export in the Subantarctic and Polar Frontal Zones of the Southern Ocean, south of Australia, *Journal of Geophysical Research*, 106(C12), 31,489– 31,509.

Thompson, D.W.J., and Solomon, S., 2002. Interpretation of Recent Southern Hemisphere Climate Change, *Science*, 296, 895-899.

Tortell P.D., Maldonado, M.T., Price, N.M., 1996. The role of heterotrophic bacteria in the iron-limited ocean ecosystems. *Nature* 383: 330-332

Tortell P.D., Maldonado M.T., Granger J., Price N.M. 1999. Marine bacteria and biogeochemical cycling of iron in the oceans. FEMS *Microbial Ecology* 29: 1-11

Usbeck, R., Rutgers van der Loeff, M., Hoppema, M., and Schlitzer, R., (2002), Shallow remineralization in the Weddell Gyre, *Geochemistry, Geophysics, Geosystems*, 3(1), 1008, doi:10.1029/2001GC000182.

Van den Broeke, M. 2000. The semi-annual oscillation and Antarctic climate. Part 4: note on sea ice cover in the Amundsen and Bellingshausen Seas, *International Journal of Climatology,* 20, 455-462.

van Leeuwe, M.A., Scharek, R., de Baar, H.J.W., de Jong, J.T.M., and Goeyens L. 1997. Iron enrichment experiments in the Southern Ocean: physiological responses of plankton communities. *Deep-Sea Research part II* 44 (1-2): 189-207

Varela D., Pride, C.J., and Brzezinski, M.A., 2004. Biological fractionation of silicon isotopes in Southern Ocean surface waters. *Global Biogeochemical Cycles*, 18, GB01047, doi:10.1029/2003GB002140.

Wadhams, P., Lange M.A., and Ackley, S.F., 1987. The ice thickness distribution across the atlantic sector of the antarctic ocean in midwinter, Journal of Geophysical Research, 92(C13), 14535-14552.

Wanninkhof, R.H. 1992. Relationship between wind speed and gas exchange over the ocean. *Journal of Geophysical Research*, C5: 7373-7382.

Wanninkhof, R. and McGillis, W.R. 1999. A cubic relationship between air-sea CO_2 exchange and wind speed. *Geophysical Research Letters,*13: 1889-1892.

Weiss, R.F., Ostlund H.G., and Craig H., 1979. Geochemical studies of the Weddell sea, *Deep-Sea Research Part I*, 26, 1093-1120.

Williams P.J.le B. 2000. Heterotrophic bacteria and the dynamics of dissolved organic material. In: Microbial Ecology of the Oceans. D.L. Kirchman (Ed.) Wiley Liss, NY, 153-200.

Wischmeyer A.G., De La Rocha C.L., Maier-Reimer E. and Wolf-Gladrow D.A., 2003a. Control mechanisms for the oceanic distribution of silicon isotopes. *Global Biogeochemical Cycles*, 17(3), 1083, doi: 10.1029/2002GB002022.

Xie, P., and Arkin, P.A., 1996. Analyses of global monthly precipitation using gauge observations, satellite estimates and numerical model predictions. *Journal of Climate*, 9: 840-858.

Yentsch C.S., and Menzel D.W. 1963. A method for the determination of phytoplankton chlorophyll and phaeophytin by fluorescence. *Deep-Sea Research* 10: 221-231.

Yuan, X. and Martinson, D.G. 1997. Antarctic sea ice area and its global connectivity, *Journal of Climatology*, 13, 1697-1717.

Zemmelink, H.J., Watson, A.J., Delille, B., Tison, J.-L., Hintsa, E.J., Houghton, L., and Dacey, J.W.H. 2005. CO_2 deposition over the multiyear ice of the western Weddell Sea. submitted to *Geophysical Research Letters*.

Zwally, H.J., Comiso, J.C., Parkinson, C.L., Cavalieri, D.J. and Gloersen P. 2002, Variability of Antarctic sea ice 1979-1998, *Journal of Geophysical Research*, 107(C5), 9, 1-29, doi:10.1029/2000JC000733.